To appear in: Iranian Journal of Earth Sciences (Iran J. Earth. Sci.)

E-ISSN: 2228-785X Print ISSN: 2008-8779

Received: 29 December 2024 Revised: 16 February 2025

Accepted: 28 February 2025

DOI: https://doi.org/10.57647/j.ijes.2025.16973

Original Research

Tectonomagmatic evolution implications of the Rashid Abad Eocene volcanic-pyroclastic rocks: evidence of an active continental margin in the subduction setting (THMP, Alborz-Azerbaijan Block (NW Iran))

Mahsa Seyyedi[1], Mohammad Lotfi[1], Arash Gourabjeripour[1], Afshin Ashja Ardalan[1]

1.Department of Geology, North Tehran Branch, Islamic Azad University, Tehran, Iran

* Corresponding author: m.lotfigeology@gmail.com

Abstract

In the Western Alborz-Azerbaijan Block, Eocene volcanic activity generated a suite of volcanic-pyroclastic rocks and marine lavas of Middle Eocene age. The study area is located 45 km north of Zanjan, in the central part of the Tarom-Hashtjin subzone within the Western Alborz-Azerbaijan structural zone, northwestern Iran. This research aims to investigate the regional tectonomagmatic evolution of Eocene volcanic-pyroclastic rocks and their significance for mineralization in the study area. Petrographic and geochemical studies of these rocks in the Rashid Abad district

illustrate a compositional range from acidic to intermediate-basic, ranging from rhyolite to basalt. Based on the geochemical data, the rocks exhibit a high-K calc-alkaline to shoshonitic series. According to the geochemical data, these rocks are mainly enriched in LREEs (e.g., Nd, Ce, La, and Sm) and LILEs (e.g., Rb, Cs, Pb, and K) but are depleted in HFSEs (e.g., Ti and Nb). Furthermore, the REE patterns indicate a negative Eu anomaly. These geochemical characteristics show the obvious features of the magmatic arc and magmatic activity related to subduction, which were derived from the involvement of released fluids from a subducted oceanic slab in the enrichment of magma elements. The ratios of Nb/U, Ce/Pb, Nb/U vs. Ce/Pb, and Na/Ta confirm the influence of crustal contamination in the area. The Nb/Y vs. Rb/Y ratios also demonstrated that the rocks were enriched in the subduction zone and experienced crustal contamination. The fractional crystallization (FC) trend was proved by the decrease in the concentrations of MgO, FeO_t, Fe_2O_3, CaO, TiO_2, Al_2O_3, Na_2O, and P_2O_5 with increasing SiO_2. The FC of pyroxene, plagioclase, and Fe-Ti oxides is the primary process in the magmatic evolution of the Rashid Abad volcanic and pyroclastic rocks. Moreover, the Ba/Rb vs. Rb ratio highlights the influence of crustal contamination associated with FC process within the upper crust. According to the tectonic discrimination diagrams, the rocks of the region exhibit characteristics of a magmatic arc setting related to an active continental margin arc in a subduction zone. Furthermore, the Nb/Y ratio, which varies below 1.72, confirms the presence of an active continental margin setting in the Rashid Abad district. The Eocene andesites and andesite basalts of the study area originated from the partial melting of a spinel lherzolite source, whereas dacitic and rhyolitic magmas formed by partial melting of the lower amphibolite crust. Based on these studies and results, it can be concluded that the primary magma of these rocks, of mantle origin, probably originated from partial melting of subducted oceanic crust and was metasomatized by fluids derived from a subducted slab. Finally, as the magma ascended through the crust or interacted with a shallow-level crustal magma chamber, it became contaminated with crustal material before undergoing fractional crystallization and eventually was suffered from FC.

Keywords: *Magmatic evolution, Active continental margin, subduction, Tarom-Hashtjin, Rashid Abad (Rashtabad)*

1. Introduction

According to Alberti et al. (1980), the young magmatic zone is situated between the Black and Caspian Seas, and extends into central Anatolia (Fig. 1a). This area is referred to as the Azerbaijan Magmatic Province. Later studies, such as Azizi et al. (2006), refer to this region as the 'Alborz-Azerbaijan Block,' which includes the western Alborz and northwestern Iran. The Alborz magmatic belt, oriented east-west, is divided into western and eastern parts by the north-south Rasht-Takestan fault (Fig. 1b). The western part, referred to as the "Alborz-Azerbaijan Magmatic Belt" (AAMB), is subdivided into two mineralized provinces: (1) the Ahar-Arasbaran Belt (AAB) in the north and (2) the Tarom-Hashtjin Metallogenic Province (THMP) in the south (Fig. 1b). The Alborz magmatic cycle in the Eocene-Oligocene led to the formation of a large assemblage of volcanic, intrusive, semi-intrusive, and pyroclastic igneous rocks in the Tarom-Hashtjin mineralization zone, creating numerous mineral deposits (Hajalilo, 1999; Ghorbani, 2007; Abdolahadi et al. 2025; Salehpour et al. 2025). The THMP Zone is one of the most important metallogenic provinces in Iran. It hosts porphyry-epithermal mineralization associated with Eocene to Oligocene volcanic and plutonic events (Seyyedi et al., 2022). In the THMP, numerous studies have been conducted (e.g., Ahmadian, 1991; Moayyed, 1991, 2001; Hajalilo, 1999; Asiabanha and Foden, 2012; Nabatian et al., 2012, 2014, 2016; Yazdi et al. 2016; Ghasemi Siani et al., 2015, 2020, 2022; Aghazadeh et al., 2015; Otari and Dabiri 2015;Mokhtari et al., 2016; Feyzi et al., 2016, Mehrabi et al., 2016; Kouhestani et al., 2017, 2018a, 2018b, 2019; Mollai et al. 2021; Nazari et al. 2023; Ousta et al. 2024). This belt hosts several deposits, including iron deposits such as Morvarid and Sorkheh-Dizaj (Nabatian, 2012); copper deposits, including Aliabad-Khanchay (Mokhtari et al., 2016; Kouhestani et al., 2018a) and Aghkand (Feyzi et al., 2016; Kouhestani et al., 2017); copper-gold deposits, such as North Chargar (Naderlou et al., 2020), Goloujeh (Ghasemi Siani et al., 2015; Mehrabi et al., 2016), Khalyfehlou (Esmaeli et al., 2015, 2019; Hosseinzadeh et al., 2016),and Lubin-Zarde (Zamanian et al., 2020); the Nikoueieh polymetallic epithermal deposit (Aghajani et al., 2016, 2020), and the Dehanj manganese deposit (Nabatian et al., 2012). Most studies in this area focus on existing mineralizations, while less attention has been directed to the lithology and geochemistry of volcanic rocks and intrusive masses. The background for the study area includes geological and geophysical maps, reports, and other studies conducted in the region. The most significant base maps for the region include the 1:250,000 Bandar Anzali geological map (Clarc et al., 1975), the 1:100,000 Hashtjin geological map (Faridi and Anvari, 1996), the 1:250,000

Bandar Anzali aeromagnetic map (Clarc et al., 1975), and the systematic geochemical explorations of the 1:100,000 Hashtjin area (TOZ Co., 2003). Additionally, reports have been published by various researchers and organizations, including Sadr Jahan Mines Development Company (2013, 2016, 2017). Tertiary metallogenesis in the Western Alborz-Azerbaijan (Mianeh-Hashtrood) region, particularly in the Hashtjin area, was also studied by Hajalilo (1999). Additionally, studies have been conducted on the alterations, mineralization, and economic geology of copper and gold in the region (e.g., Hajalilo and Khakzad, 1999; Chichaki and Mokhtari, 2002; Afzali, 2010; Afzali et al., 2010; Baranpurian et al. 2014; Ajalli et al., 2017, 2021; Dabiri et al. 2018; Yazdi et al. 2019; Seyyedi et al., 2022; Yazdi et al. 2022; Ashrafi et al. 2024). However, the lithological, geochemical, tectonic-magmatic patterns, and magmatic evolution related to the formation of volcanic-pyroclastic rocks in the Rashid Abad region have received less attention. A detailed investigation and understanding of these features is crucial for identifying the precise pattern of mineralization in the Rashid Abad area and its surroundings within the THMP. The volcanic and pyroclastic rocks of the Rashid Abad region are part the Eocene volcanic belt, which is situated in the central section of the Tarom-Hashtjin subzone within the Western Alborz-Azerbaijan structural zone. Consequently, this research aims to investigate the importance of regional tectonomagmatic evolution in the mineralization of the Rashid Abad volcanic and pyroclastic rocks. To achieve this purpose, petrogenesis, tectonomagmatic setting, and magmatic evolution of the Eocene volcanic and pyroclastic rocks in the study area were analyzed.

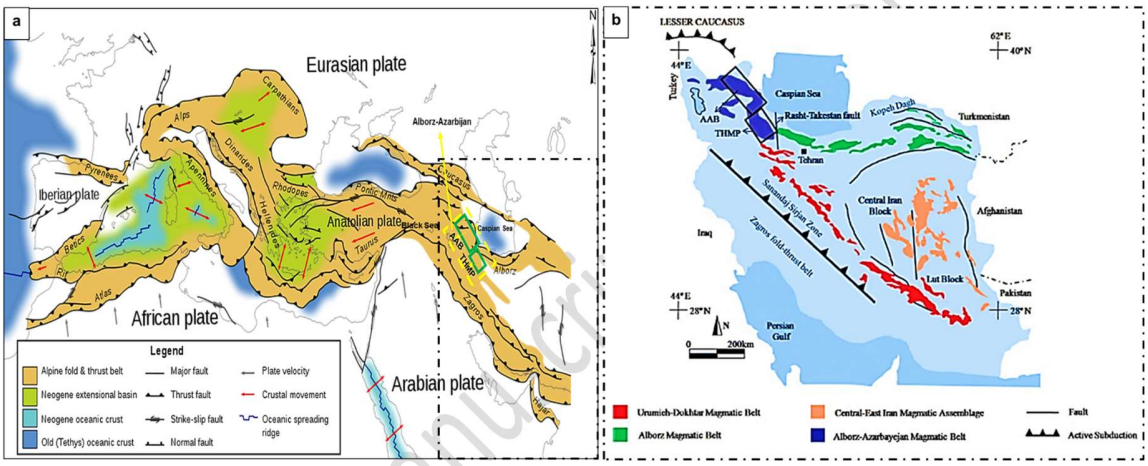

Figure 1. (a) Location of the study area within the Alpine-Himalayan orogenic belt, highlighting the boundaries of the Iranian, Eurasian, Anatolian, and Arabian plates (Woudloper, 2009). (b) Location of the Tarom-Hashtjin Metallogenic Province (THMP) within the Alborz-Azarbayejan Magmatic Belt (AAMB), NW Iran. The AAMB is subdivided into the Ahar-Arasbaran Belt (AAB) in the north and THMP in the south (Ghasemi Siani et al., 2015; Mehrabi et al., 2016).

2. Geological background

2.1. Regional geological setting

The Alborz magmatic belt, oriented east-west (E-W), is located in northern Iran. It is 600 km long and 100 km wide. The Alborz range is part of the Alpine-Himalayan orogeny, formed by the convergence of the Central Iranian and Eurasian plates since the late Triassic (Shokri et al., 2020) (Fig. 1a). Based on structural trends in Iran, tectono-magmatic settings can be divided into eight segments: (1) the Zagros fold belt, (2) the Zagros thrust belt (Neotethyan suture zone), (3) the magmatic-metamorphic Sanandaj-Sirjan zone (SSZ), (4) the Urumieh-Dokhtar Magmatic Arc (UDMA), (5) the Central Iran Block (CIB), (6) the Alborz Magmatic Arc (AMA), (7) the Alborz- Kopeh Dagh belt, and (8) the Eastern Iran/Makran zone (Fig. 2a) (Stöcklin, 1968; Stöcklin and Nabavi, 1973; Alavi, 1994). The opening

and closing of the Tethyan Ocean in several consecutive stages have controlled the evolution of these fragments. The closure of the Paleo-Tethys along the "Paleo-Tethys suture zone" in the north of the Alborz magmatic arc, combined with the collision of the Central Iranian and Eastern Iranian microcontinents with Eurasia, led to the formation of the Alborz-Kopeh Dagh belt (Berberian and King, 1981; Şengör, 1984; Alavi, 1996; Hollingsworth et al., 2010) (Fig. 2a). The Alborz Magmatic Belt formed during two main orogenic cycles (Şengör et al., 1993; Zanchi et al., 2006): (1) the extinction of the Paleo-Tethys in the Late Triassic (Cimmerian) and collision of the Iranian Plate with Eurasia, and (2) the extinction of the Neo-Tethys and deformation of intraplate re-Unauthenticated Download Date related to the convergence of the Arabian and the Eurasian plates. In the Alborz Magmatic Arc (AMA), Eocene volcanic processes include an assemblage of pyroclastic rocks and marine lavas from the Middle Eocene, known in Iranian stratigraphy as the Karaj Formation (Stöcklin and Eftekhar Nezhad, 1969). The Alborz magmatic belt (AMB) is divided into western and eastern sections by the north-south Rasht-Takestan fault (N-S) (Fig. 1b). The eastern part is composed of basic and acidic tuffs and lavas, with an alkaline to shoshonitic affinity (Blourian, 1994; Moayyed, 2001; Nabatian and Ghaderi, 2013; Nabatian et al., 2014). The western part, referred to as the 'Alborz-Azerbaijan Magmatic Belt' (AAMB), is composed of andesitic to dacitic lavas and numerous granitoid bodies with a calc-alkaline to shoshonitic affinity (Moayyed, 2001). Furthermore, these tectono-magmatic zones can be subdivided into smaller magmatic-metallogenic provinces (e.g., Azizi and Moinevaziri, 2009; Azizi and Asahara, 2013; Azizi et al., 2019). Alborz-Azerbaijan Magmatic Arc (Western AMA) is separated from the UDMA by a narrow fragment of the Central Iran microcontinent, which extends northward into the Lesser Caucasus in Armenia and the Eastern Pontides in Turkey to the north. This region is subdivided into the Ahar–Arasbaran Zone (AAZ) in the north and the Tarom-Hashtjin Metallogenic Province (THMP) in the south (Fig. 2a). The THMP is located in the western Alborz magmatic belt (Alborz-Azerbaijan magmatic zone), at the junction with the Urmia-Dokhtar magmatic belt (Eftekhar Nezhad, 1980; Aghanabati, 2004; Stöcklin, 1968). In the AMA, the Late Cretaceous is represented by volcanic and volcano-sedimentary rocks in the western Alborz, and by a thick series of carbonates and marls in north-central Alborz (Brunet et al., 2003). The Eocene was marked by widespread volcanic eruptions in Iran, particularly in the AMA region. The Karaj Formation, along with other equivalent volcanic and volcano-sedimentary layers resulting from these eruptions, developed in the central and western parts of the AMA Mountains within an extensional tectonic regime (Allen et al., 2003; Ballato et al., 2010; Berberian, 1983; Hassanzadeh et al., 2002). Furthermore, the AMA is divided into two magmatic-metallogenic subzones: the Ahar-Arasbaran Metallogenic Belt (AAB) in the north and the Tarom-Hashtjin Metallogenic Province (THMP) in the south (Fig. 2b). The Tarom-Hashtjin metallogenic zone comprises sections: the Hashtjin Mountains in the north and the Tarom Mountains in the south. The Rashid Abad mining district is located in the center of the Tarom-Hashtjin metallogenic province (Fig. 3). Regionally, the Tarom-Hashtjin metallogenic province contains Precambrian metamorphic basement, Cambrian and Permian metamorphic rocks, Jurassic to Cretaceous limestone and sandstone, as well as Eocene to Oligocene volcano-plutonic rocks. The Precambrian metamorphic unit includes schist, phyllite, and felsic rocks. The Cambrian strata consist of dolomitic marble and phyllite. The Permian low-grade metamorphic rocks, consisting of limestone and shale, discordantly overlie the Cambrian strata. Additionally, the Permian strata also discordantly overlie the Mesozoic rocks, which comprise sandstone, limestone, and siltstone. The Cenozoic volcaniclastic rocks are widely distributed throughout the province and include trachybasalt, trachyandesite, trachydacite, andesite, andesitic basalt, basalt, rhyodacite, rhyolitic lava flows, and tuff. The plutonic rocks consist of batholiths and smaller bodies in the form of granodiorite, quartz monzonite, and granite (Fig. 3).

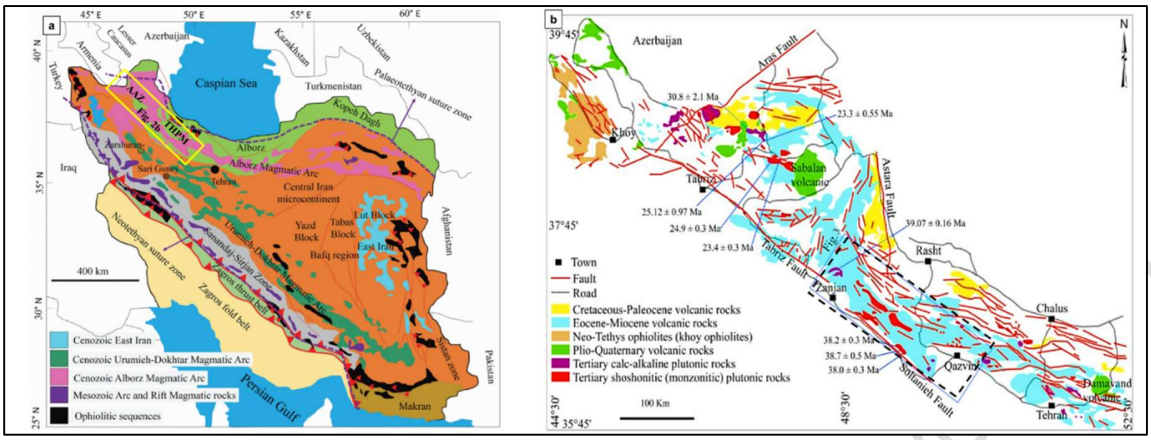

Figure 2. (a) Location of the Tarom-Hashtjin metallogenic province on the geology map of Iran (Modified after Stöcklin, 1968; Stöcklin and Nabavi, 1973). (b) Schematic geological map showing the main Tertiary igneous rocks in the Tarom-Hashtjin metallogenic province and the Ahar-Arasbaran zone, including age determinations from previous studies (Modified after Castro et al., 2013).

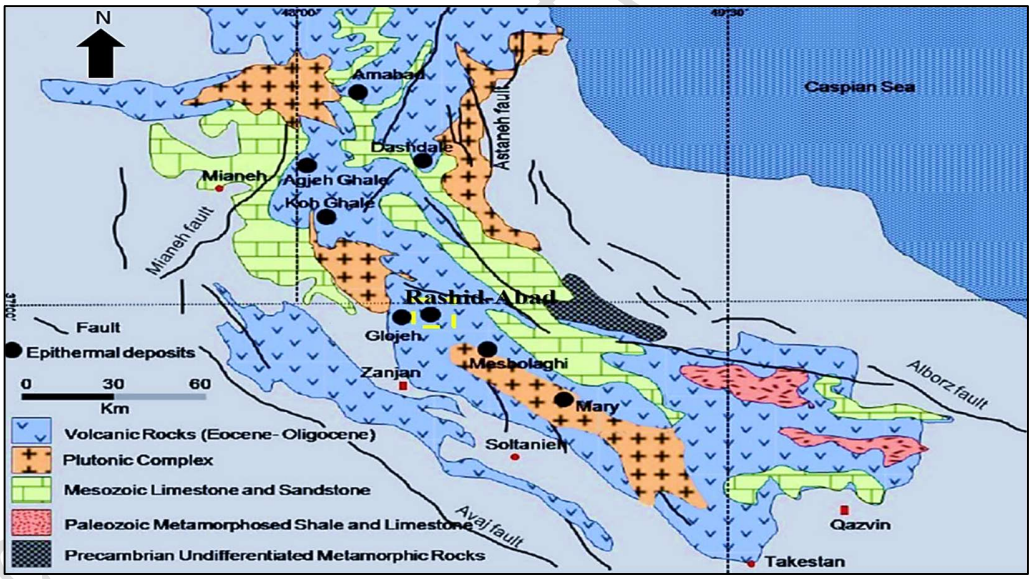

Figure 3. Regional geological map of the Tarom-Hashtjin metallogenic province, showing the location of the Rashid Abad area within the THMP (Modified after Ghorbani, 2007).

2.2. Local geology

According to the geological map of Hashtjin (Faridi and Anvari, 1996; modified by Seyyedi et al., 2022), four major Cenozoic rock units (Eocene to Oligocene) are present in the Rashid Abad area (Rasht Abad). The units include: (1) a lithic-vitric tuff unit, characterized by well-layered, dark-colored deposits and representing the most extensive unit (E^{t}); (2) basic tuff interlayered with trachybasalt (E^{V2}); (3) rhyolite and rhyodacite volcaniclastic flow deposits (Ol^{v1}); and (4) subvolcanic rocks, including porphyrite, dikes, sills, and laccoliths (Ol^{sv}) (Fig. 4a). Based on field observations, the most important outcrops of rock units in the study area were examined. The Eocene volcano-sediments (E^{v}) represent the oldest rock units in the study area, overlain by basaltic-andesite lava units. Towards the upper part of the Eocene units, the volume of lava units decreases while the volume of pyroclastic units increases. An overview of the tuff outcrops in the region is shown in Figure 5b. The studied tuff samples can be mainly classified as vitric tuff, crystal tuff, and crystal-lithic tuff. Tuffs along with andesites, andesitic tuffs and agglomerate-andesite (Fig. 5c), occur alternately with layers of varying thicknesses (Fig. 5d) in the study area. The trend, direction, and slope of the volcano-sedimentary and volcanic units have been altered due to tectonic deformation. This tectonic deformation is evidenced by the crushing of tuffs in the region (Fig. 5e). Dacitic tuffs are exposed in the study area (Fig. 5f). Furthermore, due to an erosion phase between the Eocene and Oligocene formations, volcanics and volcanoclasts deposits from the Oligocene overlie the Eocene units with a sloping discontinuity (Fig. 5g). Finally, the youngest formations in the study area are the Quaternary sediments (Fig. 5h).

2.3. Investigation of Faults

Figure 4b shows the map of faults dispersion in the Rashid Abad region. In this area, the rock units are displaced by the east-west Rasht-Abad fault. There is more than one siliceous-mineralized vein in the Rashid Abad area. According to the studies, several veins of varying dimensions have been observed, most of which are primarily connected to the region's main vein. The general trend of the main veins and sub-veins is east-west (E-W), with a slope direction dipping to the west at an angle of 65–70°. Most intrusive bodies exhibit an east-west trend and appear to be associated with the main fault systems. Recently, Seyyedi et al. (2022) conducted a study in the area, integrating remote sensing and aeromagnetic data. In this study, faults and lineaments were identified and analyzed using a sun-angle filter on OLI band 8 (panchromatic), along with analytic signal (AS) and first-order vertical derivative (FVD) filters. Considering that the main fault trend in this region is NW-SE (Fig. 4b), it can be confidently inferred that the mineralization trend is likely perpendicular to these faults, oriented in the NE-SW direction. Thus, the main Rasht-Abad fault (E-W), along with lineaments exhibiting NW-SE and NE-SW trends, were detected and extracted (Seyyedi et al., 2022). These extracted lineaments and faults were verified using the geological map and field investigations (Seyyedi etal., 2022) (Fig. 6a, b). Eventually, the final map of lineaments and faults for the study area was prepared by Seyyedi et al. (2022) (Fig. 6c).

2.4. Mineralization and Alteration

In this district, mineralization is closely associated with the Rasht-Abad fault, as the mine is situated within the fault zone. Additionally, the other veins are located along the same fault zone. Therefore, the penetration of hydrothermal fluids and the formation of mineralization phases are a result of the activity of faults over different periods. In fact, a connection between the faults and mineralization phases can be proposed (e.g., Shahbazi et al., 2019). In many sections, the main mineralization vein is composed of silica-breccia. The main siliceous-brecciaed vein is formed from tuff, andesitic tuffs, andesite, dacite, rhyolite, trachyandesite, basaltic trachyandesite, and basalt (Fig. 7a). There are hydrothermal alterations in this area. The most important altrations include siliceous (Fig. 7c), argillic, sericite (phyllic), iron oxides, and propylitic (Fig. 6d). Most of the mineralization occurs along silicified hydrothermal veins, which are abundant in the region (Fig. 7b). The silicic alteration exists in the form of silicification, vein-veinlet, and the hydrothermal cement of breccia in the region (Fig. 7a-c). Additionally, the mineralization phases show a strong correlation with silicic veins and silicification (e.g., Shahbazi et al., 2019). Argillic alteration can be observed around the siliceous alteration and along the margins of the mineralized veins. Sericitization, or phyllic alteration, is primarily associated with argillic alteration and is observed in some veins. Iron oxide alteration has also occurred due to leaching in the region. Finally, propylitic alteration is widespread in this district, with chloritization being the most prominent indicator of this alteration in the rocks of the region. In general, the mineralization in the area has formed in two

hypogene and supergene phases (Figs. 7, 8). First, in the hypogene stage, magnetite was formed as the only initial oxide mineral (Fig. 8a). Chalcopyrite as the first sulphide mineral of the hypogene phase, has been formed in the form of a mass with a replacement texture (Fig. 8c, d). Bornite is the second mineral of the hypogene sulphide phase, often forming through the replacement of chalcopyrite at the edges, boundaries of grains, and fractures (Fig. 8c). The second main phase in the region is the supergene. This stage is also divided into oxide and sulfide phases. In the supergene process, mineral enrichment occurs due to leaching of the upper parts of the deposit, driven by atmospheric water circulation and accompanied by chemical weathering and oxidation. The oxide phase of supergene contains hematite, cuprite, goethite-lepidocrocite, and malachite-azurite (copper carbonate). Blade and needle-shaped hematite (specularite) is formed from the region's primary magnetite under oxide conditions, and High oxygen fugacity at the Earth's surface (Fig. 8b). Cuprite mineral is composed from the decomposition of chalcopyrite and is observed alongside hematite blades in the region (Fig. 8e, f). The iron hydroxides in the area include goethite-lepidocrocite (with a rhythmic texture, Fig. 8g), which are often associated with hematite and chalcopyrite. Like cuprite, they also formed from the decomposition of chalcopyrite along the edges and boundaries of grains, as well as in fractures (Fig. 8e-g). In the supergene phase, copper carbonates include azurite and, especially, malachite, which are highly abundant and form through the decomposition and replacement of chalcopyrite (Fig. 8f, h). Digenite-chalcocite and covellite are supergene-phase sulfide minerals that form along the edges of chalcopyrite and bornite as a result of their replacement (Fig. 8d, e). Additionally, during the main mineralization stage, quartz, as the primary gangue mineral, forms simultaneously with chalcopyrite (Fig. 8h).

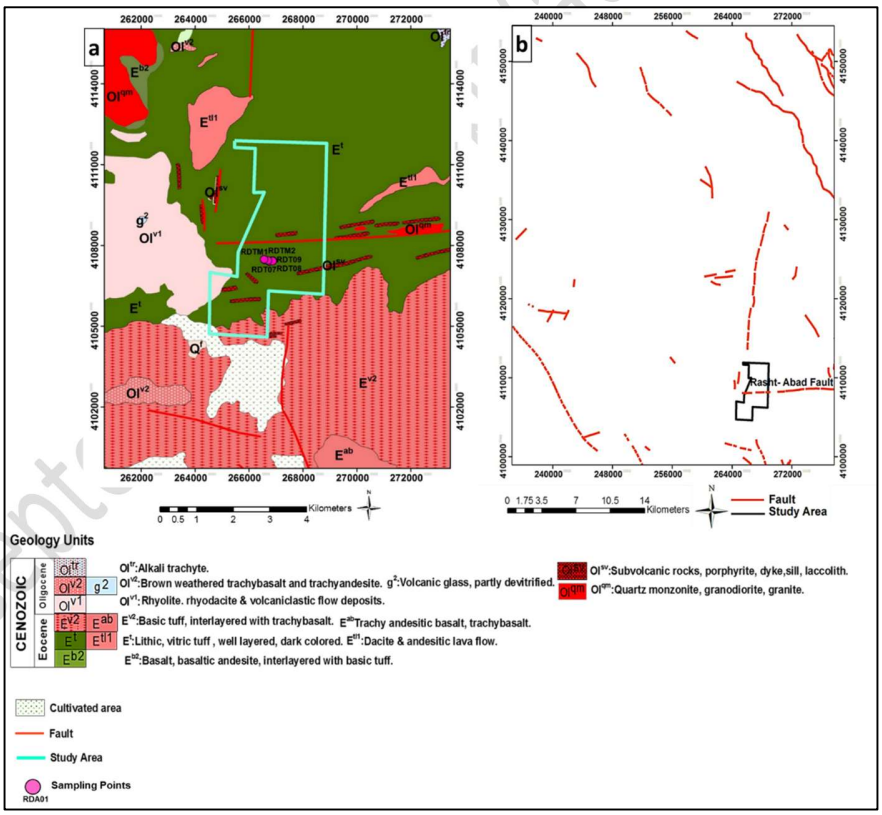

Figure 4. (a) Geological map of Hashtjin at a 1:100,000 scale. (b) Fault locations in Hashtjin at a 1:100,000 scale (Faridi and Anvari, 1996; modified by Seyyedi et al., 2022).

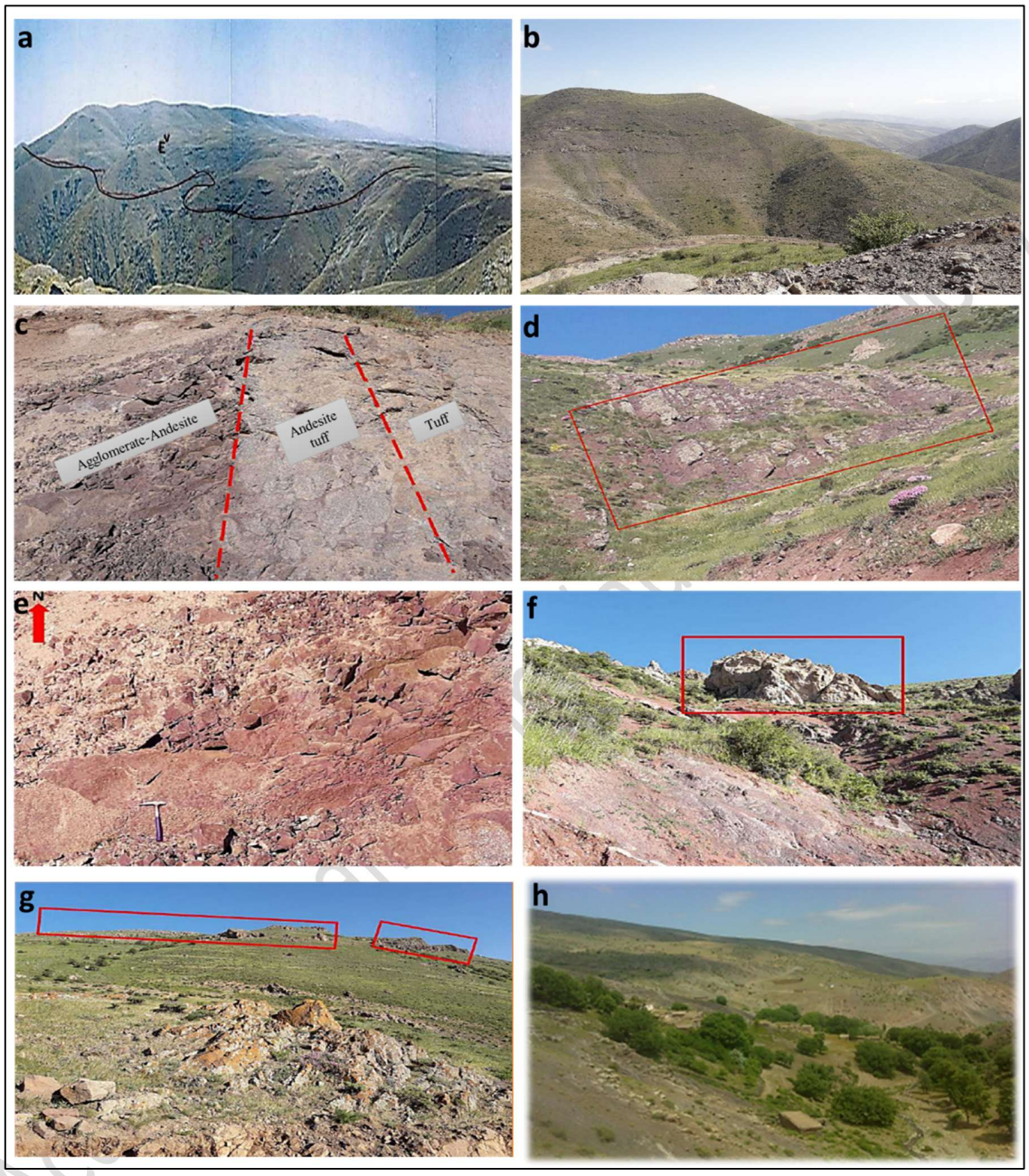

Figure 5. Outcrops of rock units in the study area. (a) Eocene volcano-sediments (E^v) (view to the south and southeast). (b) General view of the tuffs in the study area (view to the north). (c) View of tuff, andesitic tuffs and agglomerate-andesite (view to the north). (d) View of tuffs with layering (slope direction to the northwest). (e) View of crushed tuffs (view to the north). (f) View of Dacitic tuffs (view to the north). (g) View of Oligocene volcanics and volcanoclasts with a sloping discontinuity on the Eocene units (view to the north). (h) View of Quaternary sediments (view to the north).

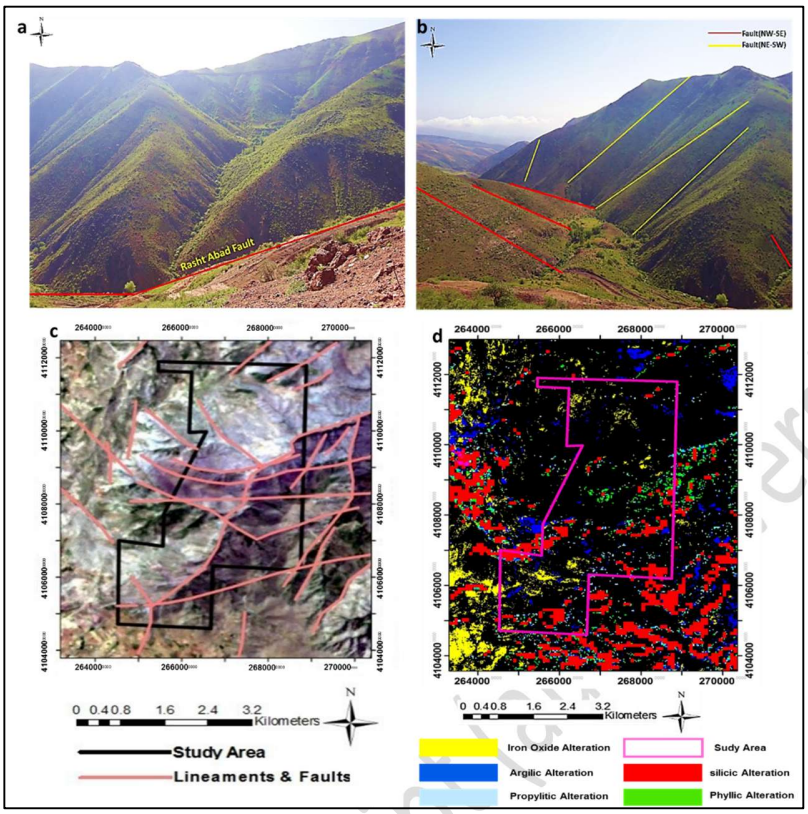

Figure 6. (a) view of the Rasht-Abad fault (view to the north). (b) view of faults with NW-SE and NE-SW trends (View to the north). (d) The alteration map of the Rashid Abad mining area (Seyyedi et al., 2022).

Figure 7. (a) View of the main mineralized vein and the host rock (andesitic tuff) with an east-west trend. (b) Close-up view of mineralization on the main silica-breccia vein, showing malachite and azurite mineralizations (east-west trend) .(c) View of andesite containing siliceous veinlets. (d) Chalcopyrite and malachite associated with the veinlets.

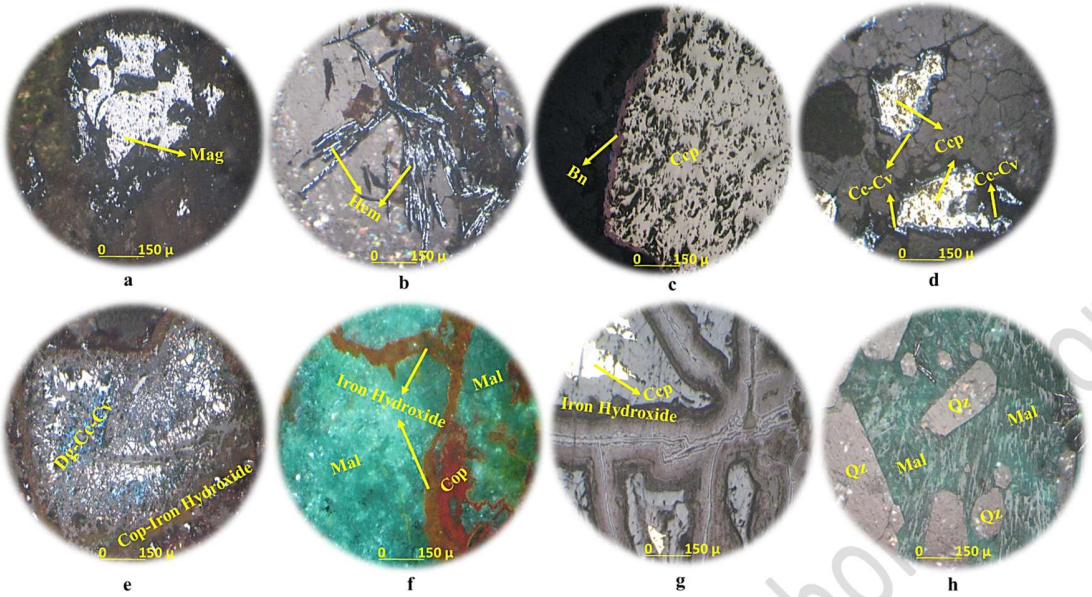

Figure 8. Stages of hypogene and supergene mineralization in the Rashid Abad area. (a) Magnetite mineralization. (b) Blade- and needle-shaped hematite (specularite). (c) Bornite replacing chalcopyrite along the edges and boundaries of grains, and in fractures. (d, e) Mass texture of chalcopyrite. Supergene effects, including the conversion of chalcopyrite at the margins into digenite, chalcocite, and covellite, exhibiting replacement textures. (f) Cuprite and iron hydroxides (goethite-lepidocrocite) associated with copper carbonate (malachite) in the supergene phase. (g) Rhythmic texture in iron hydroxides (goethite-lepidocrocite) with chalcopyrite. (h) Quartz gangues with chalcopyrite formation. Mineral abbreviations are given in: Kretz (1983) Symbols for Rock-forming minerals (Magnetite (Mag), Hematite (Hem), Chalcopyrite (Ccp), Bornite (Bn), Digenite (Dg), Chalcocite (Cc), Covellite (Cv), Malachite (Mal), Cuprite (Cop), Iron hydroxides (goethite-lepidocrocite) and Quartz (Qz)).

3. Research Methods

Given the importance of volcanic-pyroclastic rocks in mineralization, particularly copper, in this region, an investigation into their petrography and petrogenesis is essential. The samples from this region were collected from outcrops of volcanic and pyroclastic rocks. During the field surveys and observations, a total of 42 polished thin sections from mineralized veins and alteration zones were examined using optical microscopy. To conduct geochemical studies, 18 whole-rock samples were collected, and their major element oxides were analyzed using the X-ray fluorescence (XRF) method at the Kansaran Binaloud Company laboratory (Iran). Furthermore, whole-rock trace elements, including rare earth elements (REEs), were determined by the ICP-MS (inductively coupled plasma-mass spectrometry) method (56 elements) at the Zarazma Company lab (Iran). The XRF and ICP-MS results are presented in Tables 1 through 4. Before processing the geochemical analysis of the studied samples, corrections for loss on ignition (LOI) were made by removing volatile substances from the raw data. After this correction, the data were presented in a revised table (Table 2.). Subsequently, further processing was carried out based on the data in the revised table (Table 2.). To remove volatile substances (LOI), the LOI percentage of each rock sample was subtracted from the sum of the total oxides of that sample. The resulting value represented the new amount of rock oxides with volatile substances removed. Subsequently, the ratio (100 divided by the corrected oxide value) was multiplied by the percentage of each oxide to calculate the percentages of oxides without volatile substances.

Table 1. Major raw oxide contents (wt%) in the analyzed volcanic and pyroclastic rock samples, determined using the XRF

Sample Name	Rock Type	X (Meter)	Y (Meter)	Z (Meter)	Major raw element oxides											
					SiO_2	TiO_2	Al_2O_3	Fe_2O_3	MnO	MgO	CaO	Na_2O	K_2O	P_2O_5	LOI	Total
					Detection Limit											
					0.01 %	0.001 %	0.01 %	0.01 %	0.001 %	0.01 %	0.01 %	0.01 %	0.01 %	0.001 %	0.01 %	
RDA01	Volcanic	266576	4107478	1755	53.26	1.012	16.26	8.75	0.356	4.63	4.85	2.12	6.02	0.312	2.13	99.70
RDA03	Pyroclastic	266578	4107466	1756	51.47	0.989	16.63	13.52	0.685	3.58	0.95	1.16	6.42	0.302	3.95	99.66
RDA04	Volcanic	266579	4107463	1755	54.71	1.012	17.32	10.21	0.521	2.85	0.93	1.89	6.45	0.262	3.38	99.54
RDA05	Pyroclastic	266754	4107412	1675	63.42	0.812	15.68	6.49	0.112	2.37	0.59	0.05	4.62	0.202	5.38	99.73
RDA06	Pyroclastic	266748	4107413	1676	60.63	0.865	15.37	9.89	0.156	2.83	0.72	0.03	3.02	0.22	5.92	99.66
RDA08-B	Pyroclastic	266748	4107406	1677	54.89	1.012	16.34	9.05	0.372	4.29	1.69	0.72	5.52	0.196	5.76	99.84
RDA09	Pyroclastic	266750	4107406	1675	55.78	0.989	16.89	8.57	0.245	3.78	1.35	0.85	6.82	0.301	4.02	99.60
RDA10	Pyroclastic	266877	4107432	1588	61.89	0.526	15.85	6.52	0.441	1.89	1.05	0.42	4.21	0.089	6.85	99.74
RDA12	Volcanic	266857	4107426	1601	71.35	0.364	13.89	3.48	0.213	1.39	0.41	0.21	6.76	0.047	1.62	99.73
RDI01	Volcanic	266577	4107469	1756	74.02	0.037	2.33	20.45	0.186	0.45	0.12	0.21	0.03	0.026	1.89	99.75
RDT01	Volcanic	266576	4107478	1755	51.26	1.012	16.63	9.76	0.312	4.53	5.16	2.35	5.72	0.286	2.56	99.58
RDT02	Volcanic	266579	4107463	1755	53.37	0.986	17.65	8.62	0.342	3.41	1.06	1.23	9.52	0.244	3.19	99.62
RDT05	Volcanic	266748	4107413	1676	60.36	0.912	15.69	9.45	0.156	2.42	0.79	0.02	3.52	0.204	6.30	99.83
RDT07	Volcanic	266750	4107406	1675	52.45	0.765	17.56	8.05	0.325	5.4	0.82	0.21	8.91	0.196	4.88	99.57
RDT08	Volcanic	266871	4107429	1594	62.52	0.556	15.41	4.95	0.116	1.21	0.74	1.63	4.68	0.089	7.75	99.65
RDT09	Pyroclastic	266872	4107424	1594	66.35	0.408	14.82	3.15	0.216	1.69	0.76	1.29	5.72	0.041	5.35	99.79
RDTM1	Volcanic	266698	4107440	1702	59.56	0.853	16.68	6.59	0.148	2.63	4.46	2.58	3.85	0.201	2.08	99.63
RDTM2	Volcanic	266560	4107479	1755	59.49	0.848	16.45	6.21	0.346	2.64	3.5	2.51	5.14	0.178	2.43	99.74

Table 2. Major oxide contents (wt%) of the analyzed volcanic and pyroclastic rock samples after correction for volatile substances (LOI), determined using the XRF method.

Sample Name	Group	Rock Type	)Meter)X	)Meter)Y	)Meter)Z	Major element oxides											
						SiO_2	TiO_2	Al_2O_3	Fe_2O_3	MnO	MgO	CaO	Na_2O	K_2O	P_2O_5	Na_2O+K_2O	Total
						Detection Limit											
						0.01%	0.00%	0.01%	0.01%	0.00%	0.01%	0.01%	0.01%	0.01%	0.00%		
RDA01	Volcanic	Terachyandesite	266576	4107478	1755	54.59	1.04	16.66	8.97	0.36	4.75	4.97	2.17	6.17	0.320	8.343	100
RDA03	Pyroclastic	Basaltic terachyandesite	266578	4107466	1756	53.78	1.03	17.38	14.13	0.72	3.74	0.99	1.21	6.71	0.316	7.920	100
RDA04	Volcanic	Terachyandesite	266579	4107463	1755	56.90	1.05	18.01	10.62	0.54	2.96	0.97	1.97	6.71	0.272	8.673	100
RDA05	Pyroclastic	Dacite	266754	4107412	1675	67.22	0.86	16.62	6.88	0.12	2.51	0.63	0.05	4.90	0.214	4.950	100
RDA06	Pyroclastic	Dacite	266748	4107413	1676	64.69	0.92	16.40	10.55	0.17	3.02	0.77	0.03	3.22	0.235	3.254	100
RDA08-B	Pyroclastic	Terachyandesite	266748	4107406	1677	58.34	1.08	17.37	9.62	0.40	4.56	1.80	0.77	5.87	0.208	6.633	100
RDA09	Pyroclastic	Terachyandesite	266750	4107406	1675	58.36	1.03	17.67	8.97	0.26	3.96	1.41	0.89	7.14	0.315	8.025	100
RDA10	Pyroclastic	Dacite	266877	4107432	1588	66.63	0.57	17.06	7.02	0.47	2.03	1.13	0.45	4.53	0.096	4.985	100
RDA12	Volcanic	Rhyolite	266857	4107426	1601	72.72	0.37	14.16	3.55	0.22	1.42	0.42	0.21	6.89	0.048	7.104	100
RDI01	Volcanic	Dacite	266577	4107469	1756	75.64	0.04	2.38	20.90	0.19	0.46	0.12	0.21	0.03	0.027	0.245	100
RDT01	Volcanic	Basaltic terachyandesite	266576	4107478	1755	52.83	1.04	17.14	10.06	0.32	4.67	5.32	2.42	5.90	0.295	8.318	100
RDT02	Volcanic	Tephriphonolite	266579	4107463	1755	55.34	1.02	18.30	8.94	0.35	3.54	1.10	1.28	9.87	0.253	11.148	100
RDT05	Volcanic	Dacite	266748	4107413	1676	64.54	0.98	16.78	10.10	0.17	2.59	0.84	0.02	3.76	0.218	3.785	100
RDT07	Volcanic	Terachyandesite	266750	4107406	1675	55.39	0.81	18.55	8.50	0.34	5.70	0.87	0.22	9.41	0.207	9.632	100
RDT08	Volcanic	Dacite	266871	4107429	1594	68.03	0.60	16.77	5.39	0.13	1.32	0.81	1.77	5.09	0.097	6.866	100
RDT09	Pyroclastic	Rhyolite	266872	4107424	1594	70.25	0.43	15.69	3.34	0.23	1.79	0.80	1.37	6.06	0.043	7.422	100
RDTM1	Volcanic	andesite	266698	4107440	1702	61.05	0.87	17.10	6.76	0.15	2.70	4.57	2.64	3.95	0.206	6.591	100
RDTM2	Volcanic	Terachyandesite	266560	4107479	1755	61.13	0.87	16.90	6.38	0.36	2.71	3.60	2.58	5.28	0.183	7.861	100

Table 3. Concentration of trace and rare earth elements (REEs) in the analyzed volcanic rock samples, determined using the ICP-MS method.

Volcanic Rocks												
Volcanic Rocks	Sample Name	RDA01	RDA04	RDA12	RDI01	RDT01	RDT02	RDT05	RDT07	RDT08	RDTM1	RDTM2
	Rock Type	Terachyandesite	Terachyandesite	Rhyolite	Dacite	Basaltic terachyandesite	Tephriphonolite	Dacite	Terachyandesite	Dacite	andesite	Terachyandesite
Location	X(Meter)	266576	266579	266857	266577	266576	266579	266748	266750	266871	266698	266560
	Y(Meter)	4107478	4107463	4107426	4107469	4107478	4107463	4107413	4107406	4107429	4107440	4107479
	Z(Meter)	1755	1755	1601	1756	1755	1755	1676	1675	1594	1702	1755
Elements	Detection Limit (DL)- ppm											
Li	1	32	46	17	84	30	41	29	47	9	26	26
Na	100	16424	15171	7873	412	16212	1207	8740	1955	17104	20848	17602
K	100	42830	47740	58035	309	41630	23066	54027	44397	25902	22611	39236
Rb	1	170	179	244	6	165	155	196	165	91	73	136
Cs	0.5	5.5	6.8	6.1	9.4	5	21.8	5.4	5.8	3.5	3.2	4.1
Be	0.2	1.5	2.1	2.6	1.3	1.5	4.8	1.6	2	1.3	1.6	1.9
Mg	100	>2%	14983	8312	5299	>2%	12622	17038	>2%	6512	12994	13657
Ca	100	35781	7380	3974	1659	31324	6068	8380	5506	5334	28996	24299
Sr	1	344.1	238.4	155.4	7.3	304.1	97.7	296.4	183.9	105.3	298.2	292.4
Ba	1	823	1417	1295	16	762	220	1750	1508	956	636	852
P	10	1492	1459	310	50	1426	1382	1446	1247	461	1086	1074
As	0.1	10.9	23.1	7.3	14.7	13.4	51.5	17.6	19.1	10.2	6.7	9.5
Sb	0.5	3.6	2.6	3.4	32.8	3.6	6.2	4.4	1.7	1.2	1.6	1.9
Bi	0.1	0.2	0.4	0.5	16.8	0.2	0.8	0.2	0.3	0.2	0.2	0.2
S	50	<50	<50	<50	<50	<50	<50	<50	<50	<50	<50	<50
Se	0.5	1.14	1.66	0.79	0.81	1.39	1.66	1.41	1.35	1.2	1.42	1.49
Te	0.1	0.13	0.16	<0.1	<0.1	0.1	0.66	0.1	0.1	<0.1	0.16	0.16
La	1	20	19	30	<1	18	11	17	37	23	26	25
Ce	0.5	41	37	60	<1	39	36	34	65	46	54	51
Pr	0.05	4.91	4.89	7.1	0.21	5.6	4.05	5.39	9.56	5.7	7.61	7.57
Nd	0.5	21.8	20.5	23.9	1.8	21.3	15.8	20.1	33.2	18.5	25.3	25.3
Sm	0.2	5.03	5.17	5	0.35	4.99	3.96	5.19	7.25	3.93	5.76	5.65
Eu	0.1	1.3	1.34	0.79	<0.1	1.23	0.91	1.34	1.82	0.8	1.36	1.41
Gd	0.05	4.54	4.52	3.95	<0.05	4.68	3.64	4.39	6.01	3	4.94	4.97
Tb	0.1	0.75	0.76	0.67	0.11	0.71	0.63	0.68	0.84	0.55	0.78	0.78
Dy	0.02	4.67	4.63	4.53	0.8	4.66	4.05	4.24	4.73	3.4	4.94	4.93
Er	0.05	2.68	2.46	2.87	0.1	2.44	1.99	2.12	2.32	1.98	2.84	2.74
Tm	0.1	0.37	0.34	0.45	<0.1	0.36	0.27	0.3	0.32	0.34	0.42	0.4
Yb	0.05	3.6	3.3	3.8	1	3.1	2.3	2.4	2.6	2.9	3.4	3.2

Lu	0.1	0.35	0.27	0.49	<0.1	0.33	0.21	0.23	0.27	0.35	0.38	0.38
Sc	0.5	22.7	18.9	5.5	2.9	20.7	10.8	16.6	14.7	6.9	13.2	13.9
Y	0.5	22.2	22.2	23.6	2.3	20.2	16.3	17.6	22.4	17.9	23.5	22.8
Th	0.1	3.82	4.25	14.79	<0.1	3.66	4.7	4.38	6.21	9.37	7.07	6.56
U	0.1	1.2	1.2	4	0.7	1.01	1.8	1.1	1.7	2.2	1.89	1.8
Ti	10	6493	6612	2520	<10	5828	4844	6065	5013	3688	4956	5096
Zr	5	91	63	140	5	70	46	40	54	151	125	83
Hf	0.5	2.23	1.5	4.54	<0.5	2.06	1.08	1.14	1.14	3.73	2.93	2.35
V	1	176	170	43	122	157	111	149	112	72	98	103
Nb	1	8.7	10	20.3	1.3	8.1	13	11	10.9	13.1	13.8	13.9
Ta	0.1	0.55	0.76	1.17	0.12	0.44	0.92	0.69	0.64	0.77	0.81	0.74
Cr	1	76	40	4	11	73	20	34	15	6	14	15
Mo	0.1	<0.1	<0.1	<0.1	2.1	<0.1	1.3	<0.1	<0.1	0.2	<0.1	<0.1
W	1	1.6	1.5	1.7	583.8	12.9	7.5	3.1	3.5	3.7	1.5	1.4
Mn	5	2603	3915	1403	2569	2229	1596	2551	2335	732	965	2535
Fe	100	52328	58129	15186	>10%	48193	63716	48509	44473	26444	36038	36743
Co	1	25.8	23	3.2	14.8	23.1	18.3	21.9	13.3	5.1	13.2	13.6
Ni	1	22	14	<1	1	20	8	9	1	<1	1	2
Cu	1	47	9	19	636	32	24	20	4	205	18	9
Ag	0.1	0.2	0.4	0.5	1	0.1	0.6	0.4	0.5	1.7	0.2	0.2
Zn	1	154	428	276	355	134	111	650	233	75	89	205
Cd	0.1	0.1	0.7	0.2	0.5	0.2	0.3	0.4	0.8	0.2	0.1	0.4
Al	100	81312	84020	70181	15283	73810	68024	76915	83295	75370	79040	75821
In	0.5	<0.5	<0.5	<0.5	<0.5	<0.5	<0.5	<0.5	<0.5	<0.5	<0.5	<0.5
Tl	0.1	0.94	1.51	1.25	<0.1	0.89	1.21	1.46	1.21	0.67	0.34	0.63
Sn	0.1	1.3	0.9	1.2	7.4	1.2	1.7	0.7	1.5	0.8	1.3	1.6
Pb	1	14	58	68	63	14	24	212	16	8	9	37
Sr/Y		15.5	10.74	6.58	3.17	15.05	5.99	16.84	8.21	5.88	12.69	12.82
V/Ti		0.03	0.03	0.02	(Ti<10)/122	0.03	0.02	0.02	0.02	0.02	0.02	0.02
Ti/Zr		71.35	104.95	18.00	(Ti<10)/5	83.26	105.30	151.63	92.83	24.42	39.65	61.40
Nb/U		7.25	8.33	5.08	1.86	8.02	7.22	10.00	6.41	5.95	7.30	7.72
Ce/Pb		2.93	0.64	0.88	(Ce<1)/63	2.79	1.50	0.16	4.06	5.75	6.00	1.38
Nb/Y		0.39	0.45	0.86	0.57	0.40	0.80	0.63	0.49	0.73	0.59	0.61
Rb/Y		7.66	8.06	10.34	2.61	8.17	9.51	11.14	7.37	5.08	3.11	5.96
Ba/Rb		4.84	7.92	5.31	2.67	4.62	1.42	8.93	9.14	10.51	8.71	6.26
Th/Nb		0.44	0.43	0.73	(Th<0.1)/1.3	0.45	0.36	0.40	0.57	0.72	0.51	0.47
La/Yb		5.56	5.76	7.89	(La<1)/1	5.81	4.78	7.08	14.23	7.93	7.65	7.81
Th/Yb		1.06	1.29	3.89	(Th<0.1)/1	1.18	2.04	1.83	2.39	3.23	2.08	2.05
Ta/Yb		0.15	0.23	0.31	0.12	0.14	0.40	0.29	0.25	0.27	0.24	0.23
Th/Hf		1.71	2.83	3.26	(Th<0.1)/(Hf<0.5)	1.78	4.35	3.84	5.45	2.51	2.41	2.79
Ta/Hf		0.25	0.51	0.26	0.12/(Hf<0.5)	0.21	0.85	0.61	0.56	0.21	0.28	0.31
Th/Ta		6.95	5.59	12.64	(Th<0.1)/0.12	8.32	5.11	6.35	9.70	12.17	8.73	8.86
Nb/Ta		15.82	13.16	17.35	10.83	18.41	14.13	15.94	17.03	17.01	17.04	18.78
Rb/Yb		47.22	54.24	64.21	6.00	53.23	67.39	81.67	63.46	31.38	21.47	42.50
Zr/Nb		10.46	6.30	6.90	3.85	8.64	3.54	3.64	4.95	11.53	9.06	5.97
La/Nb		2.30	1.90	1.48	(La<1)/1.3	2.22	0.85	1.55	3.39	1.76	1.88	1.80
Hf/Ta		4.05	1.97	3.88	(La<0. 5)/0.12	4.68	1.17	1.65	1.78	4.84	3.62	3.18

S/Y	(S<50)/22.2	(S<50)/22.2	(S<50)/23.6	(S<50)/2.3	(S<50)/20.2	(S<50)/16.3	(S<50)/17.6	(S<50)/22.4	(S<50)/17.9	(S<50)/23.5	(S<50)/22.8
Nb/La	0.44	0.53	0.68	1.3/(La<1)	0.45	1.18	0.65	0.29	0.57	0.53	0.56
ΣREE	111.00	104.18	143.55	4.37	106.40	84.81	97.38	170.92	110.45	137.73	133.33
$(La/Yb)_N$	3.75	3.88	5.32	NA	3.91	3.22	4.78	9.59	5.35	5.16	5.27
Eu/Eu*	0.83	0.85	0.54	NA	0.78	0.73	0.86	0.84	0.71	0.78	0.81

Table 4. Concentration of trace and rare earth elements (REEs) in the analyzed pyroclastic rock samples, determined using the ICP-MS method.

Pyroclastic Rocks								
Pyroclastic Rocks	**Sample Name**	RDA03	RDA05	RDA06	RDA08-B	RDA09	RDA10	RDT09
	Rock Type	Basaltic terachyandesite	Dacite	Dacite	Terachyandesite	Terachyandesite	Dacite	Rhyolite
Location	**)Meter)X**	266578	266754	266748	266748	266750	266877	266872
	)Meter)Y	4107466	4107412	4107413	4107406	4107406	4107432	4107424
	)Meter)Z	1756	1675	1676	1677	1675	1588	1594
Elements	**Detection Limit)DL)-ppm**							
Li	1	47	29	39	43	28	18	18
Na	100	4569	921	994	6206	10764	2203	10552
K	100	53678	35271	25337	44329	52343	20614	41497
Rb	1	202	200	158	186	203	79	187
Cs	0.5	5.9	18.8	18	7.1	5	1.7	4.4
Be	0.2	1.5	3.4	3.8	1.9	1.3	1.6	2.3
Mg	100	18218	13578	14547	>2%	14651	13280	9294
Ca	100	6915	5100	6027	5922	9035	9504	5504
Sr	1	138	124.3	109.5	116.7	137.2	93.8	140
Ba	1	1272	492	199	1176	1309	424	888
P	10	1189	1214	1270	920	1278	393	285
As	0.1	45.9	26	22.7	34.3	26.8	11.3	8.7
Sb	0.5	2.2	3.6	5.3	2.1	2.4	2.7	2.6
Bi	0.1	3.1	0.5	0.7	0.2	0.6	0.2	0.4

S	50	<50	<50	129	<50	<50	149	<50
Se	0.5	<0.5	1.41	0.92	0.77	0.89	1.34	1.57
Te	0.1	0.11	0.22	0.41	<0.1	0.22	<0.1	0.27
La	1	13	19	12	14	27	39	31
Ce	0.5	26	41	25	29	49	78	54
Pr	0.05	3.13	5.24	3.84	3.75	6.84	8.45	6.83
Nd	0.5	14	21.6	16.4	14.6	25.3	29.2	20.7
Sm	0.2	3.51	5.25	3.9	3.3	5.29	5.86	4.06
Eu	0.1	0.91	1.23	0.9	0.89	1.35	1.12	0.61
Gd	0.05	3.01	5.35	3.59	2.6	4.18	5.16	3.58
Tb	0.1	0.52	0.88	0.62	0.49	0.62	0.82	0.63
Dy	0.02	3.27	5.7	4.01	3.16	3.79	5.22	4.3
Er	0.05	1.75	3.23	2.07	1.66	1.87	3	2.95
Tm	0.1	0.25	0.43	0.28	0.23	0.27	0.45	0.46
Yb	0.05	2.7	4	2.5	1.9	2.3	3.8	4.1
Lu	0.1	0.23	0.39	0.24	0.22	0.24	0.45	0.49
Sc	0.5	16.9	10.4	12.1	14.6	13.7	6.4	5.3
Y	0.5	15.3	27.4	18.4	12.9	16.6	24.9	24.7
Th	0.1	3.82	6.94	4.61	4.73	5.19	11.32	15.27
U	0.1	2.1	4.7	1.9	1.9	1.1	3	3.8
Ti	10	6212	5144	5401	5729	5889	2668	2413
Zr	5	61	127	72	40	63	157	156
Hf	0.5	1.45	3.13	1.38	0.98	1.5	4.48	5.02
V	1	181	95	115	132	124	45	34
Nb	1	9.3	13.8	11.4	12.1	10.9	13.4	22.4
Ta	0.1	0.64	0.94	0.92	0.87	0.67	0.86	1.4
Cr	1	47	18	21	27	21	5	4
Mo	0.1	<0.1	1.5	0.4	<0.1	<0.1	<0.1	<0.1
W	1	4.3	3.9	2.9	2	2.6	3	2.7
Mn	5	3702	1066	1120	2034	1454	1755	1457
Fe	100	59097	43592	51781	49659	46266	30901	19758
Co	1	25.7	8.2	13.3	18.2	24.1	7	5.5
Ni	1	16	2	5	6	6	<1	<1
Cu	1	600	16	15	440	181	14	222
Ag	0.1	1.1	0.6	0.8	0.3	0.6	0.5	0.5
Zn	1	404	111	146	234	121	112	99
Cd	0.1	0.6	0.2	0.2	0.6	0.5	0.1	0.1
Al	100	78317	75258	74663	72974	79127	66859	71221
In	0.5	<0.5	<0.5	<0.5	<0.5	<0.5	<0.5	<0.5
Tl	0.1	1.53	1.36	1	1.1	1.22	0.39	0.91
Sn	0.1	0.9	0.8	2.2	1.2	3.8	1.2	1.5
Pb	1	36	10	16	9	12	8	20
Sr/Y		9.02	4.54	5.95	9.05	8.27	3.77	5.67
V/Ti		0.03	0.02	0.02	0.02	0.02	0.02	0.01
Ti/Zr		101.84	40.50	75.01	143.23	93.48	16.99	15.47
Nb/U		4.43	2.94	6.00	6.37	9.91	4.47	5.89
Ce/Pb		0.72	4.10	1.56	3.22	4.08	9.75	2.70
Nb/Y		0.61	0.50	0.62	0.94	0.66	0.54	0.91
Rb/Y		13.20	7.30	8.59	14.42	12.23	3.17	7.57
Ba/Rb		6.30	2.46	1.26	6.32	6.45	5.37	4.75
Th/Nb		0.41	0.50	0.40	0.39	0.48	0.84	0.68

La/Yb	4.81	4.75	4.80	7.37	11.74	10.26	7.56
Th/Yb	1.41	1.74	1.84	2.49	2.26	2.98	3.72
Ta/Yb	0.24	0.24	0.37	0.46	0.29	0.23	0.34
Th/Hf	2.63	2.22	3.34	4.83	3.46	2.53	3.04
Ta/Hf	0.44	0.30	0.67	0.89	0.45	0.19	0.28
Th/Ta	5.97	7.38	5.01	5.44	7.75	13.16	10.91
Nb/Ta	14.53	14.68	12.39	13.91	16.27	15.58	16.00
Rb/Yb	74.81	50.00	63.20	97.89	88.26	20.79	45.61
Zr/Nb	6.56	9.20	6.32	3.31	5.78	11.72	6.96
La/Nb	1.40	1.38	1.05	1.16	2.48	2.91	1.38
Hf/Ta	2.27	3.33	1.50	1.13	2.24	5.21	3.59
S/Y	(S<50)/15.3	(S<50)/27.4	7.01	(S<50)/12.9	(S<50)/16.6	5.98	(S<50)/24.7
Nb/La	0.72	0.73	0.95	0.86	0.40	0.34	0.72
ΣREE	72.28	113.30	75.35	75.80	128.05	180.53	133.71
$(La/Yb)_N$	3.25	3.20	3.24	4.97	7.91	6.92	5.10
$(La/Sm)_N$	2.33	2.28	1.94	2.67	3.21	4.19	4.80
Eu/Eu*	0.86	0.71	0.74	0.93	0.88	0.62	0.49

4. Petrography

The studied samples are classified into two groups: Eocene volcanic rocks and pyroclastic rocks.

4.1. Volcanic Rocks

Petrographic studies of volcanic rocks in the study area indicate a range of acidic to intermediate-basic compositions, including basaltic trachyandesite, basalt, basaltic andesite, rhyolite-dacite, and dacite-andesite for these rocks. The basaltic trachyandesite samples exhibit a porphyritic texture, characterized by phenocrysts of olivine, pyroxene, and plagioclase (Fig. 9a). Olivines are observed in olive green and gray colors. They occasionally appear in the form of strings or scales, indicating the transformation of olivine into serpentine. Chlorite is also sometimes present (Fig. 9e). Additionally, opacity is commonly observed in the olivine grains. Pyroxenes are observed as green to cream-colored, shaped to semi-shaped crystals. In some crystals, opacification has occurred, causing the entire volume of the pyroxene crystals to become opaque, with only small remnants remaining. Plagioclases are observed as automorphic and prismatic crystals, exhibiting a distinct banding effect known as polysynthetic twinning (Fig. 9b). The plagioclases are slightly altered to sericite. The groundmass consists of narrow and short plagioclase blades that intersect, along with pyroxene and opaque amorphous granules, possibly including olivine microparticles. Additionally, it contains chlorite and serpentinized products, which make up approximately 40 to 50% of the total rock volume. An equilibrium reaction between plagioclase phenocrysts and the groundmass results in the development of a sieve texture around the plagioclase (Fig. 9c). Additionally, in the groundmass, some plagioclases are intensely deformed into mylonites, and along the mylonite pathways, iron hydroxides have stained the cross-section brown due to dissolution (Fig. 9d). Due to tectonic stress, coarse crystals were altered, and phyllic (sericite), propylitic (chloritic), silicic, and carbonate alterations partially observed in the rocks (Fig. 9e). In the basalt units of the region, the general texture of these rocks is porphyritic, while some exhibit a hyalopilitic, and others show a lattice texture (Fig. 9h). These rocks are composed of plagioclase, olivine, and pyroxene crystals (Fig. 9f). In some cases, plagioclases has alterated to sericite (Fig. 9g). In the basaltic rocks of the region with a hyalopilitic texture, the phenocrysts are set in a groundmass composed of small microlites of plagioclase embedded in the glass. Lattice texture is also observed in other basaltic units, where olivine has been altered to serpentine. Alterations in these units are predominantly characterized by the sericitization of plagioclase, serpentinization of olivine, and chloritization of pyroxene. In the basaltic andesite rocks, plagioclase phenocrysts are extensively altered to sericite and are embedded in a groundmass composed of argillic, fine-grained materials and devitrified glass. Furthermore, mafic minerals undergo opacification and decomposition into iron hydroxides and opaque materials within the rock groundmass. The rock groundmass constitutes approximately 65 to 70% of the total rock volume. The most important alterations in these rocks include sericitization and argillicization. The general texture of these units is hyalopilitic, accompanied by a devitrified glass matrix (Fig. 9i). The rhyolite-dacite units of the region contain crystals of potassium feldspar and plagioclase (Fig. 9j). The groundmass comprises the simultaneous growth of quartz and fine-grained feldspar, displaying a false pyroclastic texture in these rocks. These rocks have also been affected by silica fluids, with delayed quartz veins cutting through them (Fig. 9j). Silicification is the primary alteration observed in these rocks. The dacite-andesite rocks of the region exhibit a porphyritic texture, with plagioclase crystals and opacified mafic minerals embedded in a vitreous groundmass containing sanidine microlites (Fig. 9k, l). These rocks have been significantly affected by siliceous fluids, resulting in quartz veins cutting across their cross-sections. Additionally, silicification is a prominent alteration observed in these rocks (Fig. 9l).

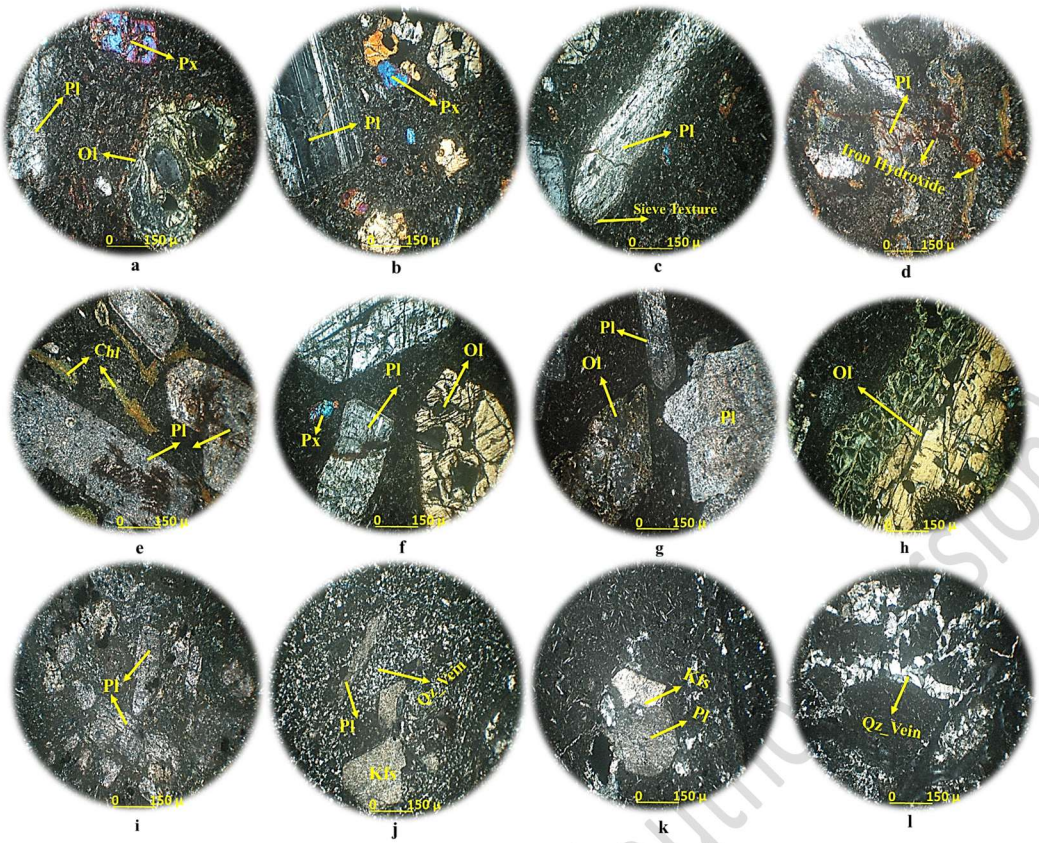

Figure 9. Photomicrographs of volcanic rock samples from the study area. (a-e) Basaltic trachyandesite samples: (a) Phenocrysts of olivine, pyroxene and plagioclase; (b) Polysynthetic banding in plagioclase; (c) Sieve texture in plagioclase; (d) Mylonitization of coarse plagioclase crystals and dissolution as brown staining in the cross-section by iron hydroxides; (e) Chloritization processe. (f-h) Basalt samples: (f) Phenocrysts of olivine, pyroxene, and plagioclase; (g) Sericitization of plagioclase; (h) Lattice texture in olivine. (i) Basaltic andesite sample: Strongly sericitized plagioclases with argillicization in a matrix of devitrified glass. (j) Rhyolite-dacite sample with a false pyroclastic texture: Crystals of K-feldspar, plagioclase and delayed quartz veins. (k,l) Dacite-andesite samples with sanidine microlites in a vitreous groundmass: (k) Crystals of K-feldspar and plagioclase; (l) Delayed quartz veins. Mineral abbreviations are given in: Kretz (1983). Symbols for rock-forming minerals: Pyroxene (Px), Plagioclase (Pl), Olivine (Ol), Chlorite (Chl), K-feldspar (Kfs), and Quartz (Qz).

4.2. Pyroclastic Rocks

Petrographic studies of pyroclastic rocks reveal different types of tuffs, including of vitric tuff, crystal tuff, and crystal-lithic tuff. In the vitric tuffs, highly argillized phenoclasts and iron hydroxides impregnated are observed. The matrix consists of clay material. These rocks exhibit a vitroclastic texture and are crosscut by quartz veins, with traces of brown iron hydroxides visible along the fracture paths. Therefore, these tuffs can be classified as argillic vitroclastic tuff (Fig. 10a). Within the vitreous tuff group, there are other types in which the matrix is composed of devitrified glass, with fragments of porphyroclastic vitric tuffs considered as lithic fragments (Fig. 10b). These samples are essentially composed of two sections: a stony part and a veiny part. The veiny part is younger and has penetrated the stony section. The stony part exhibits a devitrified vitroclastic porphyroclastic texture, with a matrix composed of glass. The process of converting the glass material into crystallized material is known as devitrification. The term is derived from the Latin vitreus, meaning glassy and transparent. These rocks display signs of this characteristic and have been cut by quartz veins. Within veins, elongated and automorphic to semi-automorphic quartz crystals are observed, oriented perpendicular to the direction of the veins. The longitudinal axis of the quartz crystals grows together, forming an interlocking texture (Fig. 10c). Generally, argillization and siliceous alteration have occurred in vitric tuffs. Prismatic plagioclase crystals are present in the crystal tuffs of the region. The matrix of these rocks consists of perlitic material, characterized by concentric circular patterns (Fig. 10d). In these samples, quartz veins intersected by cristobalite-type silica are observed, cutting through the entire cross-section (Fig. 10e). This phenomenon suggests that the primary rock is a volcanic lava with a porphyritic texture, which has been altered by siliceous fluids and undergone devitrification. As a result, these rocks are classified as crystal tuffs with a perlitic texture. The crystal-lithic tufts of the region are divided into three types. In the first type, the lithic fragments, along with feldspar and quartz crystalline phenoclasts, are embedded in a fine-grained vitroclastic matrix, with the matrix being more abundant. These fine-grain materials include shale and clay. Consequently, the primary alteration in these rocks is argillic (Fig. 10f). The second type, characterized by a porphyroclastic texture,

contains plagioclase crystals, K- feldspar, and volcanic lithic fragments (Fig. 10g). The matrix of these rocks is primarily composed of glass; however, in some samples, it is argillaceous and contains devitrified glass. Since the crystals and lithic fragments are embedded in the devitrified glass matrix, this type is referred to as strongly argillic devitrified vitroclastic crystal-lithic tuff (Fig. 10g). Additionally, argillic and siliceous alterations are observed in these rocks. The third type closely resembles the second type, except that the matrix is highly siliceous. These tuffs consist of plagioclase crystalline phenoclasts with hydroxides impregnation within in a matrix that has been extensively affected by siliceous fluids, resulting in significant silicification. Consequently, this type is classified as strongly silicified vitroclastic crystal-lithic tuff (Fig. 10h).

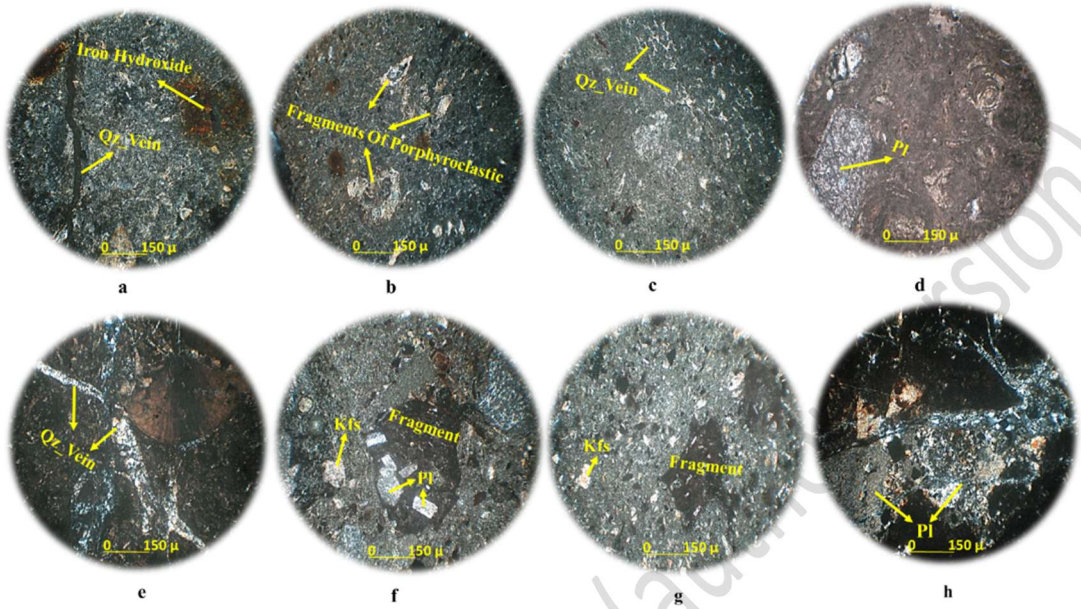

Figure 10. Photomicrographs of pyroclastic rock samples from the study area. (a) Argillic vitroclastic tuff with highly argillic phenoclasts and vitroclastic texture, crosscut by quartz veins (Qz_Vein) and traces of brown iron hydroxides along fracture paths. (b) Fragments of porphyroclastic vitric tuffs. (c) Formation of an interlocking texture in quartz crystals. (d) Matrix of perlite showing concentric circular structures. (e) Cristobalite-type silica intersecting the cross-section. (f) Crystal-lithic tuft type I. (g) Crystal-lithic tuft typs II: strongly argillic, devitrified vitroclastic crystal-lithic tuff. (h) Crystal-lithic tuft typs III: strongly silicified vitroclastic crystal-lithic tuff. Mineral abbreviations are given in: Kretz (1983). Symbols for rock-forming minerals: Plagioclase (Pl), K-feldspar (Kfs), and Quartz (Qz).

5. Geochemical characteristics

5.1. The lithochemical classification of rocks

Lithological studies, based on chemical analysis results of volcanic and pyroclastic samples and using total alkali vs. silica plots, indicate that the samples from the region span a compositional range from acidic-intermediate to basic. Volcanic samples contain 52.83 to 75.64 wt.% SiO_2 and 0.25 to 11.15 wt.% $K_2O + Na_2O$, while the pyroclastic samples range from of 53.78 to 70.25 wt.% SiO_2 and 3.25 to 8.03 wt.% $K_2O + Na_2O$. In all total alkali ($K_2O + N_{a2}O$) vs. silica (SiO_2) plots, the volcanic samples display a compositional range from rhyolite to basalt, including rhyolite, dacite, andesite, trachyandesite, basaltic trachyandesite and tephri-phonolite. Similarly, the pyroclastic samples exhibit a compositional range from rhyolite to basalt, comprising rhyolite, dacite, andesite, trachyandesite, basaltic trachyandesite, and mugearite (Fig. 11).

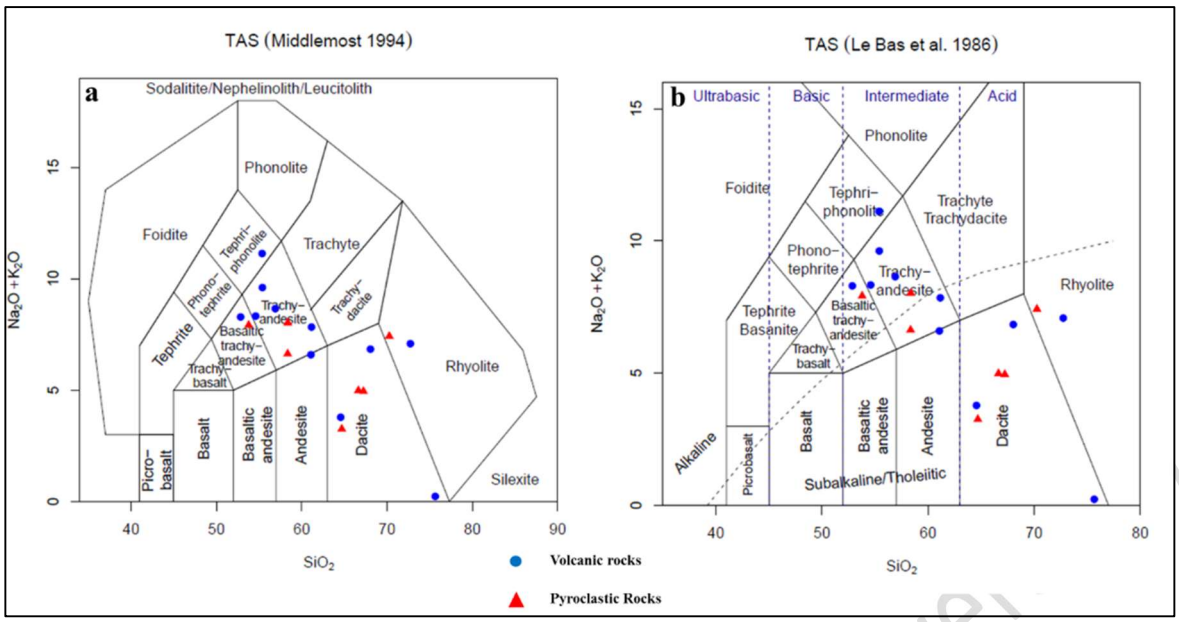

Figure 11. Total alkali-silica (TAS) variation diagrams for the classification of volcanic and pyroclastic rocks from the Rashid Abad area. (a) TAS diagram based on Middlemost (1994). (b) TAS diagram based on Le Bas et al. (1986).

5.2. Determining magmatic series

Volcanic and pyroclastic rocks of the Rashid Abad district follow a calc-alkaline series trend on the AFM (A: Alkalis [$Na_2O + K_2O$], F: FeO^t [$FeO + Fe_2O_3$], and M: MgO) diagram (Fig. 12a), with some samples trending toward the shoshonitic field. To further investigate, the SiO_2-K_2O diagram was utilized (Fig. 12b). On the K_2O vs. SiO_2 plot, the samples are classified within the high- K calc-alkaline to shoshonitic series. These plots (Fig. 12) indicate that the rocks in this region can be broadly categorized into two groups: acidic and intermediate-basic rocks, characterized as high- K calc-alkaline to shoshonitic and shoshonitic in nature, respectively.

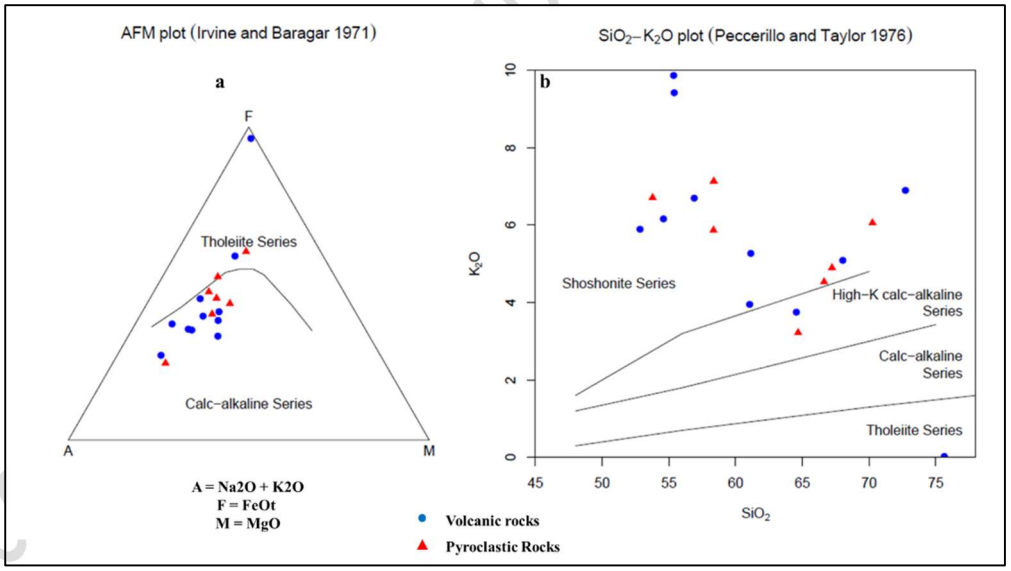

Figure 12. (a) AFM diagram (A: Alkalis [$Na_2O + K_2O$], F: FeO^t [$FeO + Fe_2O_3$], and M: MgO) (Irvine and Baragar, 1971). (b) K_2O vs. SiO_2 plot (Peccerillo and Taylor, 1976).

5.3. Harkers' Variation diagram of SiO_2 vs. major and minor elements

One of the most significant factors in Harker diagrams is the silica (SiO_2) percentage in the rocks, as it serves as a key parameter to assess and analyze magmatic differentiation trends and compositional variations. According to the analysis table and the position of the samples in the diagrams, SiO_2 content in the study area fluctuates between 52.83 and 75.64%. However, the majority of the samples, except for approximately three, exhibit SiO_2 values ranging from 52.83 to 68%. This range of silica percentages indicates that the parent magma of the rocks in the study area is predominantly sub-alkaline. According to the Harker diagrams, the values of all major oxides, except for K_2O, decrease as the SiO_2 content increases (Fig. 13). The amount of K_2O increases with higher SiO_2 content. The initial crystallization of olivine and pyroxene minerals and their separation from magma reduced the concentrations of MgO, FeO_t, and Fe_2O_3 in the remaining liquid magma. The decreasing

trend of CaO indicates the crystallization of calcic plagioclase during magmatic differentiation. In this area, the dispersion of some samples on the CaO diagram is due to processes such as clay materials and carbonation of plagioclase. Oxides such as Na_2O and K_2O (alkaline elements) are among the incompatible elements that typically show an increasing trend with rising SiO_2 content magma, and the K_2O value follows this trend. The absence of K_2O in the structure of minerals formed during the early stages of magmatic differentiation is due to the high ionic radius of potassium. In this region, as the SiO_2 content increases, Na_2O decreases. This can be attributed to partial alteration or contamination by felsic crustal material, as well as the consumption of alkali feldspar, sodic plagioclase, and their involvement in the formation of sieve texture. As a result, variations in Na_2O concentration may be due to alterations in the parent rocks. In the studied rocks, the Al_2O_3 content decreases with increasing SiO_2, which results from the concentration of plagioclase and the partial crystallization of pyroxene minerals. In the TiO_2 and P_2O_5 vs. SiO_2 diagrams, the amounts of TiO_2 and P_2O_5 decrease with increasing SiO_2 content. This is attributed to the partial fractionation of iron oxide, titanium oxide, and apatite. Figure 14 illustrates the variation of minor elements with respect to SiO_2 content. As the SiO_2 content increases, the concentrations of Ni, Cr, V, Co, Zn, Pb, and Cu decrease (Fig. 14), while the concentrations of La, Ce, Sr, Rb, Zr, Nb, Y, and A/CNK increase (Fig. 14). The contents of compatible trace elements such as Co, V, Cr, and Ni, which have smaller ionic radii, fit more easily into crystallographic sites. These elements typically accommodate Mg and Fe, separate from the magma during magmatic differentiation, and enter minerals such as olivine, pyroxene, and magnetite. As a result, the remaining magma becomes enriched in large ion lithophile elements (LILE), such as K, Sr, Ba, and others. However, elements like Ba in this region do not follow a specific trend. Because contamination and mixing of magma with the crust increase the concentration of this element in the magma, its differentiation trend cannot be observed (Fig. 14p). Ba is comparable to K in terms of ionic size and, therefore, replaces K in K-feldspars in the region. The behavior of strontium in substituting within the plagioclase structure is similar to that of barium. Due to its large ionic radius, strontium has a high concentration in plagioclase minerals. When Sr melts or crystallizes, it acts as a compatible element, replacing Ca in the plagioclase structure in this region. Rubidium is also an acceptable substitute for potassium due to its slightly larger ionic radius. As a result, the K/Rb ratio is expected to increase during the late stages of magmatic differentiation. Therefore, in the study area, the concentrations of Rb and Sr show an upward trend with increasing SiO_2, corresponding to the crystal separation process (Fig. 14j, k). Zirconium has a high ionic potential and a high electric charge, making it a member of the high-field strength elements (HFSE) group. As an incompatible element, it does not readily incorporate into common rock-forming minerals. A decrease in zircon content with increasing SiO_2 occurs when the magma becomes saturated with zircon (Li et al., 2007; Zhong et al., 2009; Liu et al., 2009). However, as shown in Figure 14l, the amount of Zr increases with SiO_2 content, indicating that the primary magma is unsaturated with zircon. Additionally, the trend of increasing Ce values on the graph partially reflects magmatic differentiation during magmatic evolution (Fig. 14i).

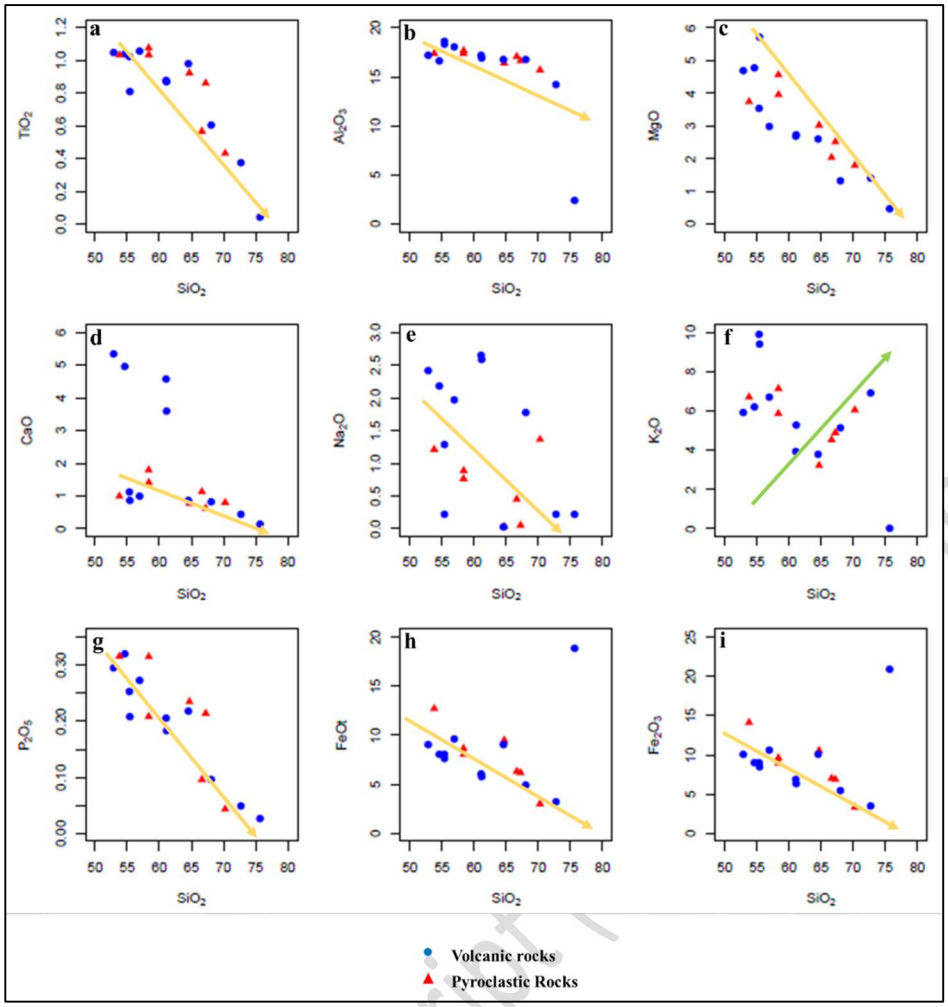

Figure 13. Harkers variation diagrams showing SiO_2 (wt.%) versus major oxides (wt.%) for the analyzed rock samples: (a) TiO_2. (b) Al_2O_3. (c) MgO. (d) CaO. (e) Na_2O. (f) K_2O. (g) P_2O_5. (h) FeO_t. (i) Fe_2O_3.

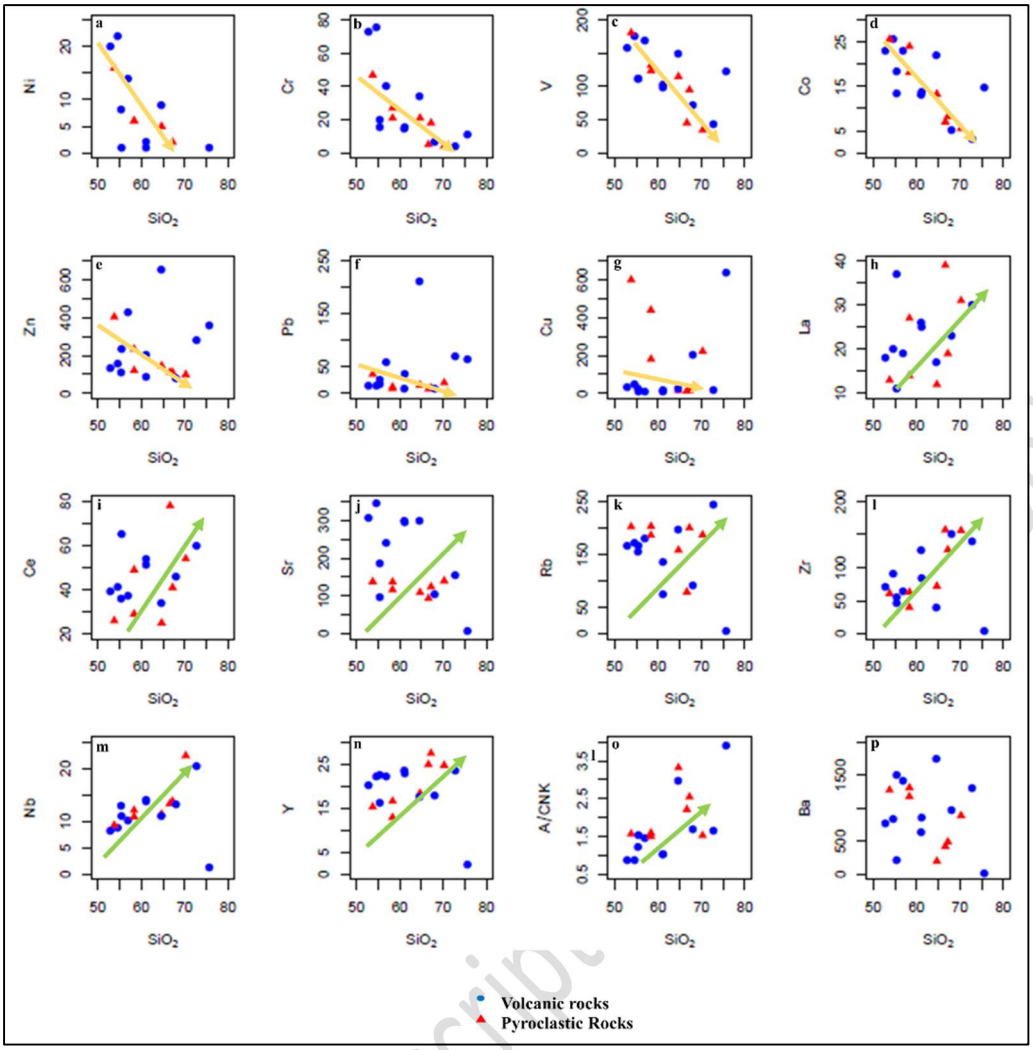

Figure 14. Harkers variation diagrams showing SiO_2 (wt.%) versus minor elements (ppm) for the analyzed rock samples. (a) Ni. (b) Cr. (c) V. (d) Co. (e) Zn. (f) Pb. (g) Cu. (h) La. (i) Ce. (j) Sr. (k) Rb. (l) Zr. (m) Nb. (n) Y. (o) A/CNK. (p) Ba.

5.4. Investigation of changes in trace elements using spider diagrams

Group analyses of trace elements can be used to identify and investigate petrological processes and lithological developments. According to the chondrite-normalized REE patterns in the spider diagram, the volcanic and pyroclastic rocks of the study area exhibit a relatively smooth parallel trend for REE plots. In terms of petrogenesis, this trend corresponds to similar petrogenetic processes (Fig. 15). It also suggests that the various rocks in the study area are related through the segregation of the same primary magma (e.g., Kelemen et al., 1997; Marchesi et al., 2006; Rahmani et al., 2020; Li et al., 2023). In general, both groups of volcanic and pyroclastics rocks from the Rashid Abad area can be investigated based on their TiO_2 and REE characteristics (e.g., Dagva-Ochir et al., 2019; Dagva-Ochir et al., 2020). The TiO_2 content ranges from 0.37 to 1.05 wt.% (average 0.79 wt.%) in volcanic rocks and from 0.43 to 1.08 wt.% (average 0.85 wt.%) in pyroclastic rocks of the region. The total average TiO2 content for both groups is 0.81 wt.%. The chondrite-normalized REE patterns of volcanic rocks show significant enrichment in light REEs (LREEs), and depletion of heavy REEs (HREEs) ($(La/Yb)_N$ = 3.22 to 9.59, with an average 5.02) (e.g., Dagva-Ochir et al., 2020). Similarly, In the chondrite-normalized REE patterns of pyroclastics rocks also display significant LREE enrichment, and HREE depletion ($(La/Yb)_N$ = 3.2 to 7.91 with an average 4.94) (e.g., Dagva-Ochir et al., 2020). In addition, the total average of $(La/Yb)_N$ ratio for both groups is 4.99. The degree of LREE and HREE differentiation is moderate to high, with $(La/Sm)_N$ ratios ranging from 1.75 to 3.77 (average 2.71) in volcanic rocks, and from 1.94 to 4.8 (average 3.06) in pyroclastics rocks of the area. The total average $(La/Sm)_N$ ratio for both groups is 2.86. The $(Eu/Eu^*)_N$ ratio ranges from 0.54 to 0.86 (average 0.77) in volcanic rocks and from 0.49 to 0.93 (average 0.75) in pyroclastic rocks, with a total average of 0.76 for both groups. These rocks exhibit a negative Eu anomaly (Fig. 15). Therefore, this depletion of Eu in the Rashid Abad volcano-pyroclasts suggests a high fugacity of oxygen in the hydrothermal fluid (Khajehmohammadlou et al., 2020) (Fig. 15). The ΣREE content ranges from 84.81 to 170.92 (average 119.98) in volcanic rocks and from 72.28 to 180.53 (average 111.29) in pyroclastic rocks. Also, the total average ΣREE for both groups is 116.40. Therefore, in this area, the chondrite-normalized

REE patterns reflect a moderate total REE (ΣREE) content, enriched LREE, and depletion with a nearly flat trend in HREE (e.g., Alizadeh et al., 2023). In fact, they are characterized by distinct fractionation of LREE and HREE (e.g., Li et al., 2016) (Fig. 15). According to the N-MORB, E-MORB, and primitive mantle-normalized multi-element patterns (Fig. 16), the volcanic and pyroclastic rocks of the region are enriched in large ion lithophile elements (LILE) such as Cs, K, Pb, and Rb, and light rare earth elements (LREE) such as Nd, Ce, La, and Sm. These rocks are also depleted in high field strength elements (HFSE) such as Ti and Nb (e.g., Shafaii Moghadam et al., 2015b; Shafaii Moghadam et al., 2016 ; Li et al., 2016; Mazhari et al., 2017; Sepidbar et al., 2018; Dagva-Ochir et al., 2019; Dagva-Ochir et al., 2020; Mohammadi and Nakhaei 2022; Alizadeh et al., 2023; Li et al., 2023). In fact, these rocks display distinct fractionation between LILEs and HFSEs (Li et al., 2016). The ratios of Rb/Yb, Zr/ Nb and Hf/Ta range from 6 to 97.9, 3.30 to 11.71, and 1.12 to 5.20, respectively (Li et al., 2016). These are characteristic features of magmatic arcs and are indicative of subduction-related magmatic activity, which is derived from fluids released by a subducted oceanic slab in the enrichment of these elements (Küster and Harms, 1998; Ulmer, 2001; Goss and Kay, 2009; Kovalenko et al., 2010; Yazdani et al., 2018, Nazari et al., 2023). Therefore, the three normalized diagrams of N-MORB, E-MORB, and Primitive Mantle are similar (Fig. 16). The characteristics of the magmatic arc and the enrichment of LILEs in the volcanic and pyroclastic rocks of the region suggest that the magma source may be a mixture of mantle and crustal material (Miyashiro, 1978; Harris et al., 1986). This can result in a wide variety of hybrid compositions formed by the mixing of different types of mantle and crustal melts (Poli and Peccerillo, 2016; Santo, 2021). For example, the intermediate dikes (Group 3) and arc tholeiite basalt (Group 4) rocks of the Tsoroidog Uul' accretionary complex in Central Mongolia originated from a supra-subduction origin with calc-alkaline features, and the mantle source formed in the fore-arc tectonic setting around an active continental margin, respectively (Dagva-Ochir et al., 2020). According to Dagva-Ochir et al. (2019), the calc-alkaline rocks are characterized by enrichment in LREEs and LILEs (e.g., K, Rb, Ba, Sr), which are prevailed in the continental crust, as well as depletion of Nb and Ti elements (Dagva-Ochir et al., 2019). The presence of positive anomalies of K and Th reflects the role of the continental crust in the evolution of the magma of the acidic volcanic rocks in the region, indicating crustal dominance (Harris et al, 1986). Many studies lean on distinctive, approximately immobile trace elements and ratios, such as Th/Nb. This ratio is important in modern subduction-related magmas. Additionally, their distinctive negative anomalies in Nb and Ta reflect fluid-fluxed melting in the mantle wedge between the down-going oceanic lithosphere and the overriding magmatic arc (e.g., Zheng 2019). According to Barnes et al. (2001), fractionation of plagioclase decreases Sr and increases the negative Eu anomaly during magma crystallization. Therefore, a negative Sr anomaly could result from the differential crystallization in plagioclases mineralization in the study area. Furthermore, an obvious negative Eu anomaly indicates plagioclase fractionation and partial melting in the plagioclase stability field (Halder et al., 2021) (Fig. 15). Another characteristic of the acidic rocks in the region is the presence of a negative P anomaly, which may indicate the separation of apatite during the early stages of magmatic differentiation (Fan et al., 2003) (Fig. 16). Ti depletion may show the crystallization of Fe-Ti oxides or pyroxene in the early stages of magmatic differentiation, as well as high oxygen fugacity in the source environment (Edwards et al., 1994) (Fig. 16). Pb exhibits a positive anomaly in the acidic rocks of the region, which could be related to mantle wedge metasomatism by fluids from the submerged oceanic crust or magma contamination with continental crustal rocks (Kamber et al., 2002) (Fig. 16). Obvious negative Nb anomalies are observed in all samples, indicating that the magma is related to continental active margin environments. These anomalies can be caused by contamination from the crusts and fluids released from the submerged sediments (Aldanmaz et al., 2000) (Fig. 16). Therefore, depletion in HFSEs (Nb, Ti,and P), enrichment in LREEs relative to HREEs, and enrichment in LILEs suggeste active continental margin volcanic arc magmatism (e.g., Mohammadi and Nakhaei 2022). The association of strong positive Pb anomalies (e.g., G. Soder et al., 2024) and negative Nb anomalies (e.g., G. Soder et al., 2024) indicates volcanic island magmas and magmas influenced by continental crust (Hofmann, 1986). For example, in the EVF ultrapotassic rocks (Efogi Volcanic Field, Papuan Peninsula of eastern New Guinea), recycling of calc-alkaline crust has been assosiated with positive Pb anomalies and negative Nb-Ta anomalies (G.Soder et al., 2024). Generally, it can be inferred that the primary magma of acidic rocks in the study area was formed in a subduction zone and subsequently contaminated with crustal material.

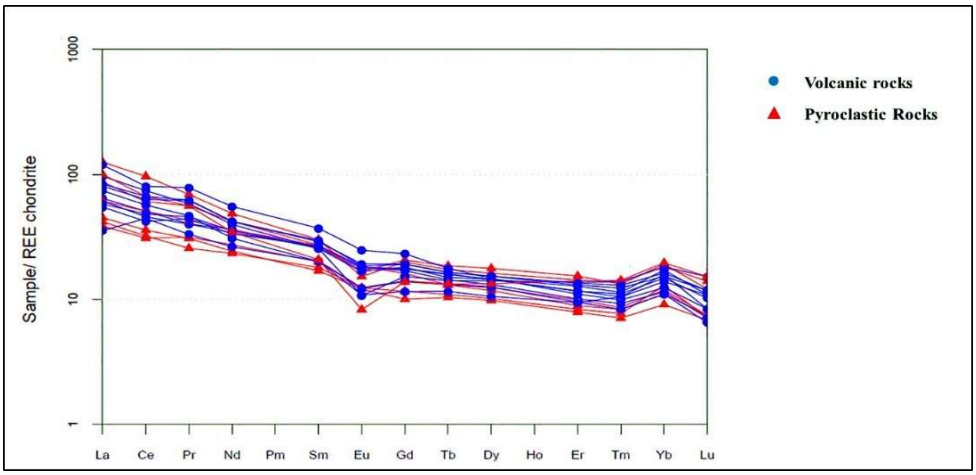

Figure 15. Chondrite-normalized Rare Earth Element (REE) diagram (Boynton, 1984) for the Rashid Abad Volcanic and Pyroclastic rocks.

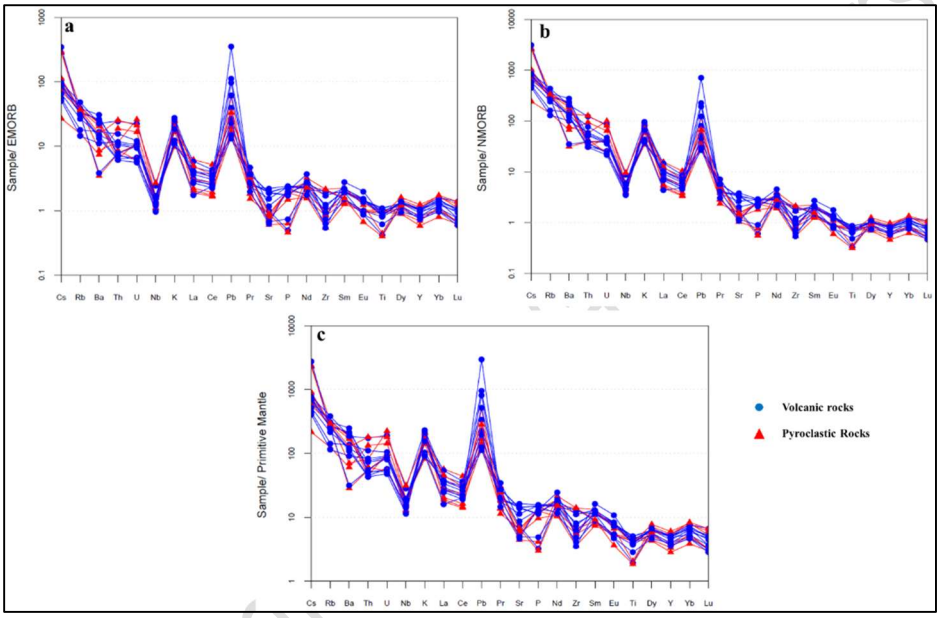

Figure 16. (a) EMORM- normalized spider diagram (Sun and McDonough, 1989), (b) NMORM- normalized spider diagram (Sun and McDonough, 1989), and (c) Primitive mantle-normalized spider diagram (Sun and McDonough, 1989) for volcanic and pyroclastic rocks from the Rashid Abad area.

6. Result and Discussion

6.1. Fractional crystallization and crustal contamination

Since the continental crust is typically enriched in highly incompatible elements, assimilation of even small amounts of crustal material by primary/parental mafic magmas can result in large-scale compositional heterogeneity in the final eruptive products (Halder et al., 2021). The mineralogy of a volcanic series reflects the processes occurring during their petrogenesis. Various events, such as magma mixing and contamination, and fractional crystallization and partial melting processes, with or without crustal contamination (FC-AFC (Assimilation Fractional Crystallization)), play traditional roles in the petrogenesis of calc-alkaline rocks in subduction zones (e.g., Çoban et al., 2012; Pang et al., 2013; Liu et al., 2014; Long et al., 2015; Yang et al., 2015; Litvak et al., 2015; Qian et al., 2016, 2017; Chazot et al., 2017; Ersoy et al., 2017, Lopes de Macêdo et al., 2022; Shamloo and Grunder, 2023). Petrographic studies (Figs. 9, 10) and binary diagrams of major element oxides versus SiO2 (Fig. 13) confirm the trend of fractional crystallization (FC), as evidenced by the decrease in the contents of MgO, FeOt, Fe2O3, CaO, TiO2, Al2O3, Na2O, and P2O5 with increasing SiO2. The ratio of trace elements and REE elements reflect the separation of minerals from the parent magma during melting, followed by fractionation, assimilation, and contamination processes (Litvak et al., 2015). This evidence reflects the FC process in the crystallization of plagioclase, pyroxene, feldspar, iron oxide, and titanium. The variation in Ti, Zr, Y, and V in the arc rock series is associated with the nature and proportion of crystallizing phases (Pearce and Norry, 1979). In the volcanic rocks, crystallization of V and Fe-Ti oxides is reflected in the

trends of decreasing Ti/Zr and V/Ti in residual melts (e.g., Nielsen et al., 1994; Pearce and Norry, 1979). The fractional crystallization of plagioclase and Fe-Ti oxide is illustrated by a decreasing trend in SiO_2 versus Sr/Y, V/Ti, and Ti/Zr diagrams (Fig. 17), as also investigated by Aydınçakır (2014) in NE Turkey. Additionally, the decreases in TiO_2 and P_2O_5 with increasing SiO_2 content (Fig. 13), and the negative Ti anomaly (Fig. 16) are attributed to the partial fractionation of iron oxide, titanium oxide, and apatite. Similar observations have been made for rock series in Chiang Khong (NW of Thailand) (Qian et al., 2016) and Eocene-Oligocene volcanic units in Momen Abad (E Iran) (Tarabi et al., 2019). Additionally, the negative Eu anomaly (Fig. 15) reflects the partial fractionation of plagioclases (Qian et al., 2016; Qian et al., 2017). All of this evidence suggests that the volcanic and pyroclastic rocks in the study area were formed by fractional crystallization (e.g., Nazari et al., 2023). The presence of crustal components in the subduction zone rock sequence with a calc-alkaline affinity has been attributed to multiple factors, including: (1) partial melting of the continental crust (e.g., Sawyer et al., 2011; Long et al., 2015; He et al., 2022; Wang et al., 2021; Cambeses et al., 2021); (2) partial melting and recycling of sediments on the descending subducting slab (e.g., Nebel et al., 2011; Qian et al., 2016; Qian et al., 2017; Su et al., 2017; Zhang et al., 2020; Novais-Rodrigues et al., 2021); (3) delamination of the crust and asthenosphere upwelling (e.g., Yang et al., 2014; Yang et al., 2015; Ersoy et al., 2017; Menke et al., 2018; He et al., 2019; Chen, 2021; Ji et al., 2021); (4) descending slab break-off and its impact on the inherited mantle source (e.g., Tatsumi, 2000; Pang et al., 2012; Pang et al., 2013; Schildgen et al., 2014; Huang, 2017; Nakamura, 2019; Kufner et al., 2021; Gerya et al., 2021). The primary volcanic rocks in the magmatic belts above subduction zones are calc-alkaline in composition (Tatsumi and Takahashi, 2006; Winter, 2010). The negative anomalies in Nb and Ti (Fig. 16) observed in the volcanic rocks may suggest potential crustal contamination (Eriksson et al., 2004). The Nb/U and Ce/Pb ratios are uniform at 47 ± 10 and 25 ± 5, respectively, in mafic lavas, such as mid-ocean ridge basalt (MORB) and ocean island basalt (OIB). These ratios are even lower in the continental crust, e.g., Nb/U = 10 and Ce/Pb = 4 (Hofmann et al., 1986; cited in Furman, 2007; Tarabi et al., 2019; Chen et al., 2021). Therefore, the analyzed rocks from the Rashid Abad region show Nb/U ratios ranging from 1.85 to 10 and Ce/Pb ratios from 0.01 to 9.75 (Fig. 18a, b). For a more detailed analysis, the Nb/U vs. Ce/Pb ratio diagram was also used. According to this plot, the samples from the region are located in the upper crust area (Fig. 18c). In another study, the elements Nb and Ta were also analyzed. The geochemistry of Nb and Ta is crucial for understanding the core-mantle differentiation of the Earth and the formation of the continental crust (Li et al., 2017). The average Nb/Ta ratios in magmas derived from mantle and crust is 17.5 and 11-12, respectively (Green, 1995). In fact, the Nb/Ta ratios in the accessible silicate reservoirs (Fig. 18d) are lower than the chondritic values of 17·5 (Jochum et al., 2000) or 19·9 (Munker et al., 2003). According to the Nb/Ta versus Nb diagram, the samples from the Rashid Abad area plot within the bulk continental crust (CC) and island arc basalt (IAB) fields (Fig. 18d). Following the injection of mafic magma with a mantle composition into the sub-crust, the transfer of heat and fluid materials leads to the melting of the lower crust. These rocks are derived from the partial melting of the lower crust, with partial mixing of mantle-derived mafic magma, confirming the influence of crustal contamination in this area. Consequently, diagrams a to d of Figure 18 clearly demonstrate the influence of crustal contamination clearly. The ratio of Nb/Y is below 1.72 in the active continental margins (Temel et al., 1998). The analyzed rocks display a variation below 1 for this parameter in the study area (Fig. 19a). According to the Nb/Y versus Rb/Y diagram (Temel et al., 1998), the samples from the Rashid Abad area were enriched in the subduction zone and experienced crustal contamination (Fig. 17b). Additionally, the Rb versus Ba/Rb plot (Askren et al., 1997) highlights the role of crustal contamination coupled with fractional crystallization in the upper crust (Fig. 19c).

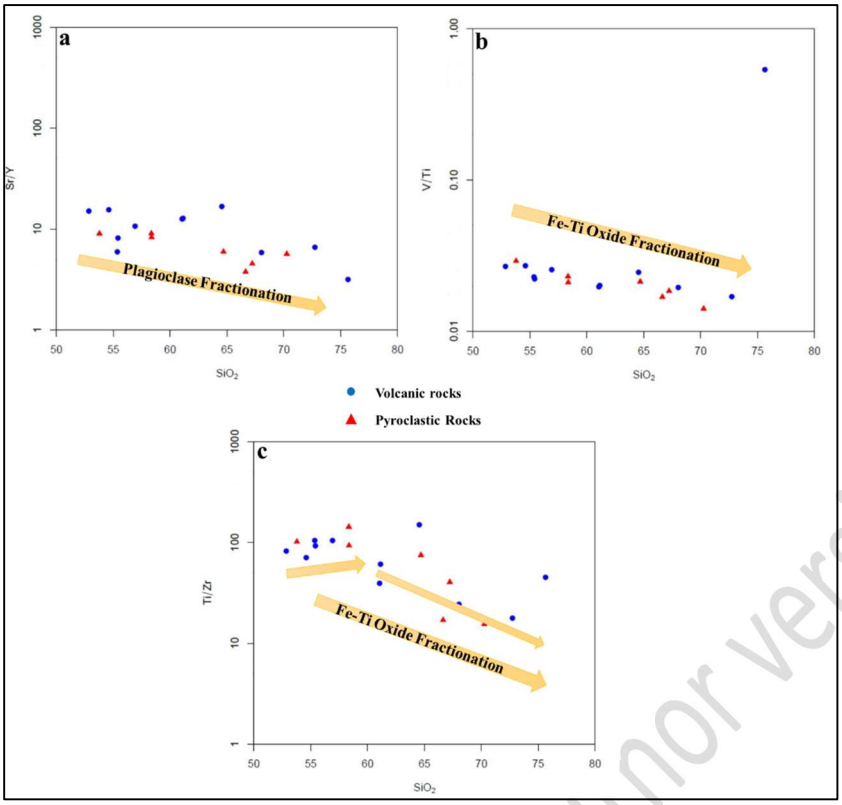

Figure 17. Rashid Abad rock samples plotted on the SiO_2 (wt.%) vs. Sr/Y, SiO_2 vs. V/Ti, and SiO_2 (wt.%) vs. Ti/Zr (Aydınçakır, 2014). (a) Fractionation of plagioclase minerals. (b,c) Fractionation of Fi-Ti oxide minerals.

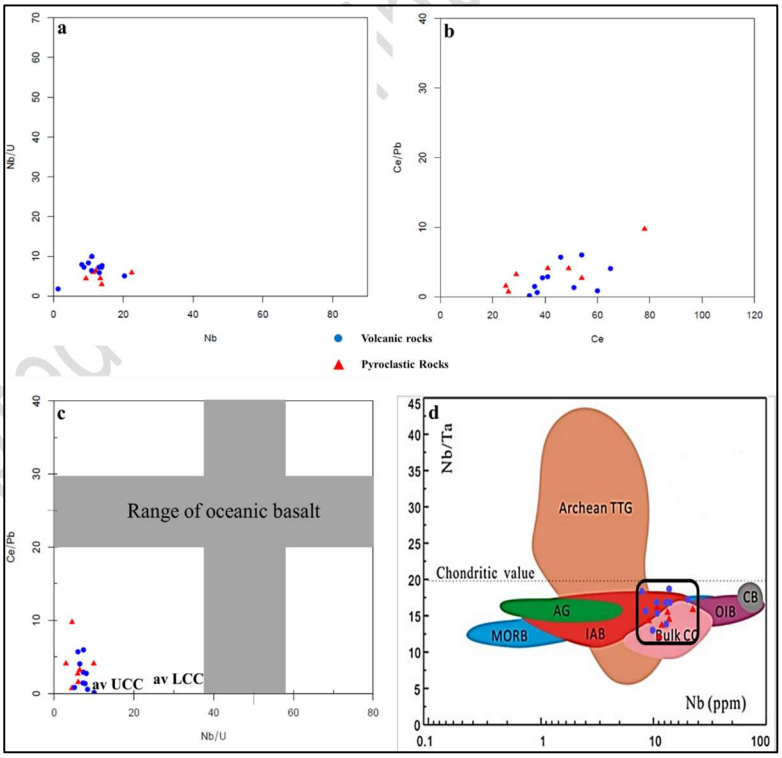

Figure 18. Rashid Abad rock samples plotted on: (a) Nb vs. Nb/U diagram (Hofmann et al., 1986 and used after Hoffman); (b) Ce vs. Ce/Pb diagram (Hofmann et al., 1986 and used after Hoffman); (c) Nb/U vs. Ce/Pb. Grey fields represent studies of oceanic basalts (Hofmann et al., 1986) unaffected by continental crustal contamination.; (d) Nb/Ta ratios across terrestrial basalts (MORB, OIB, CB and IAB) and continental crustal rocks (bulk CC and Archean TTG). The Nb/Ta in Archean TTG is highly variable but generally lower in bulk CC compared to terrestrial basalts from various geological settings (Li et al, 2017). Abbreviations: (MORB: Mid-ocean ridge basalts; OIB: ocean island basalts; CB: continental basalts; IAB: island arc basalts; AG: Archean greenstones; TTG: tonalite–trondhjemite–granite; CC: continental crust; amp: Amphibole; bio: biotite). Data sources: MORB, OIB, CB, IAB and AG from Munker et al. (2003 and 2004); Archean TTG from Hoffmann et al. (2011); bulk CC from Barth et al. (2000).

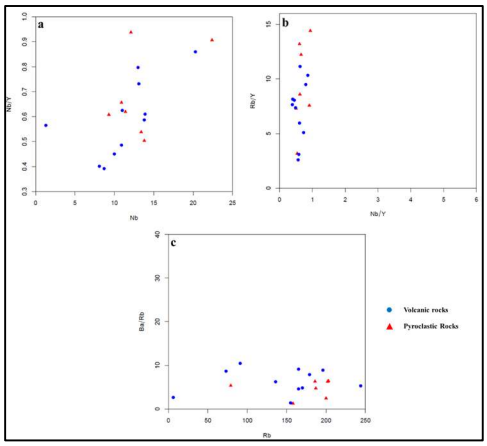

Figure 19. (a) Nb vs. Nb/Y diagram (Temel et al., 1998); (b) Nb/Y vs. Rb/Y diagram (Temel et al., 1998); (c) Rb vs. Ba/Rb diagram (Askren et al., 1997).

6.2. Petrogenesis, source of magmas, Magmatism and tectono-magmatic characteristics

The Alborz Range is part of the Alpine-Himalayan orogenic belt, which resulted from the convergence of the Central Iranian and Eurasian plates beginning in the late Triassic (Shokri et al., 2020) (Fig. 1a). The Alborz-Kopeh Dagh belt was formed due to the closure of the Paleo-Tethys along the 'Paleo-Tethys suture zone' to the north of the Alborz magmatic arc, and the collision of the Central Iranian and Eastern Iranian microcontinents with Eurasia (Berberian and King, 1981; Şengör, 1984; Alavi, 1996; Hollingsworth et al., 2010) (Fig. 2a). The Alborz magmatic belt formed during two main orogenic cycles (Şengör et al., 1993; Zanchi et al., 2006): (1) the extinction of the Paleo-Tethys in the Late Triassic (Cimmerian) and collision of the Iranian plate with Eurasia; (2) the extinction of the Neo-Tethys and deformation of intraplate re-Unauthenticated Download Date related to the convergence of the Arabian and the Eurasian plates. In this zone, Eocene volcanic processes include an assemblage of pyroclastic rocks and marine lavas of Middle Eocene age, which, in Iranian stratigraphy, are referred to as the Karaj Formation (Stöcklin and Eftekhar Nezhad, 1969). The Alborz magmatic belt, which trends east-west, is divided into western and eastern parts by the north-south Rasht-Takestan fault (Fig. 1b). The eastern part of the Alborz magmatic belt is composed of basic and acidic tuffs and lavas with an alkaline to shoshonitic affinity (Blourian, 1994; Moayyed, 2001; Nabatian and Ghaderi, 2013; Nabatian et al., 2014). The western part, which is referred to as the 'Alborz-Azerbaijan Magmatic Belt' (AAMB), consists of andesitic to dacitic lavas and numerous granitoid bodies with a calc-alkaline to shoshonitic affinity (Moayyed, 2001). The AAMB is divided into two mineralized provinces: (1) the Ahar-Arasbaran Belt (AAB) in the north and (2) the Tarom-Hashtjin metallogenic province (THMP) in the south (Fig. 1b). The Alborz magmatic cycle during the Eocene-Oligocene has resulted in a large assemblage of volcanic, intrusive, semi-intrusive, and pyroclastic igneous rocks in the Tarom-Hashtjin mineralization zone, leading to the formation of various minerals in this zone (Hajalilo, 1999; Ghorbani, 2007). Consequently, the volcanic and pyroclastic rocks of the Rashid Abad region are part of the Eocene volcanic belt in the central part of the Tarom-Hashtjin subzone within the Western Alborz-Azerbaijan structural zone. Based on geological, field and laboratory investigations, the Eocene volcanic-pyroclastic rocks of the Rashid Abad district display a combination range from acidic to intermediate-basic, spanning from rhyolite to basalt. Since these volcanic and pyroclastic rocks span the basalt to rhyolite range, the petrogenesis and magmatic evolution of these three types are discussed.

6.2.1. Petrogenesis and and magmatic evolution of rock types in the region

- **Andesite and basaltic andesite**

Andesite and basaltic andesite rocks are observed as lava flows and pyroclastic deposits in the study area. These rocks exhibit characteristics typical of subduction-related magmas. In the spider diagrams (Fig. 20c), they display depletion of HFSEs and enrichment of LILEs. Additionally, they show Pb enrichment, which is indicative of magmas originating from both the crust and subduction zones. In subduction environments, andesite and andesite basaltic rocks can form from various sources, such as the melting of subducting oceanic crust, partial melting of the underlying continental crust, and the transformation of mafic magmas derived from

metasomatized mantle during AFC (Assimilation Fractional Crystallization) and MASH (Melting-Assimilation-Storage-Homogenization) processes (Gill, 1981). The SiO_2 content in the basaltic andesite and andesite rocks of the region ranges from 52.83% to 61.13%. Magmas with this SiO_2 content cannot be directly derived from either the underlying continental crust or the subducting oceanic crust. Furthermore, magmas originating from the subducting oceanic crust typically display adakitic features, which are not observed in the rocks of this region (Fig. 21a). Therefore, the andesite and basaltic andesite rocks of the Rashid Abad area were likely formed through the evolution of mantle-derived magmas during the AFC and MASH processes. Such origins have been proposed for numerous andesite rocks in subduction environments (Askren et al., 1997; Gill, 1981). Examination of the Harker diagrams for these rocks indicates that the magma associated with the andesite and basaltic andesite underwent a fractional crystallization (FC) process during its ascent (Fig. 20a, b). As a result of this process, olivine, pyroxene and plagioclase minerals crystallized from their parent magma in crustal magma reservoirs. The negative Nb-Ta anomaly is likely caused by the retention of these elements in unmelted mantle minerals (Kelemen et al., 1993) or by reactions between the primary magma and mantle peridotite. Based on the geochemical characteristics of these rocks, their parent magma was generated from a metasomatized mantle influenced by subduction processes. The resulting magma underwent fractional crystallization and contamination in the lower crust and possibly experienced magma mixing during its ascent through the upper crust. To investigate the mineralogy and degree of partial melting of the mantle source (spinel or garnet), the highly incompatible element La and the less incompatible element Sm were analyzed. The elements Sm and La are not significantly influenced by the mineralogy of the mantle source, making them valuable for providing insights into the overall chemical composition of the source. In contrast, Yb is strongly affected by the presence or absence of garnet in the mantle source. Therefore, the La/Sm versus Sm/Yb diagram (Aldanmaz et al., 2000) was utilized to analyze the mineralogy and the degree of partial melting of the mantle source. Based on this diagram, the andesite and basaltic andesite samples from the Rashid Abad area predominantly fall within the range of 1-5% of partial melting of a spinel lherzolite source (Fig. 21b). Consequently, the primary magma of the Eocene andesite and basaltic andesite rocks in the study area is inferred to have originated from the partial melting of a metasomatized spinel lherzolite mantle source influenced by subduction processes. During its ascent, the magma likely underwent AFC and MASH processes.

- **Dacite**

Dacites are observed alongside rhyolitic rocks in the study area. These rocks can originate from a variety of sources, including partial melting of the lower crust, melting of subducting oceanic crust, or through the evolution and transformation of andesitic and basaltic andesite magmas. In other words, dacites can form through various processes, such as the fractional crystallization of mafic magma (Dungan and Davidson, 2004), magma mixing between basalt and rhyolite (Dungan and Davidson, 2004), or the partial melting of a mafic protolith (Smith et al., 2003). Basaltic rocks have not been reported on a significant scale in the region. However, it is possible that intermediate to acidic volcanic rocks, such as dacites, originated from the fractional crystallization of mafic magmas (e.g., Pan et al., 2022). Additionally, as it can be inferred in most of the Harker diagrams (Fig. 20a, b), the dacite samples do not appear to represent a continuation of the transformation process from the andesite and basaltic andesite rocks. According to the primitive mantle-normalized multi-element patterns (Fig. 20c), the region's dacites are enriched in LILEs (e.g., Cs, K, Pb, and Rb) and LREEs (e.g., Nd, Ce, La, and Sm). In contrast, they are depleted in HFSEs (e.g., Ti and Nb). These characteristics are similar to those of the bulk continental crust, indicating that the crust was likely melted (e.g., Pan et al., 2022). According to Königer (2002), some HFSEs and REEs are generally stable under conditions of altered weathering and low-grade metamorphism. Therefore, studying their their content or ratio during the diagenetic process is very useful. The La/Nb ratio (1.76–2.91) in the region's dacites is nearly identical to the crustal value (La/Nb = 2.2 ppm (Taylor and Mclennan, 1985)). The low S/Y ratio (≈ 5.99-7.01) suggests that the dacites were formed by the melting of oceanic crust. Additionally, the dacite samples exhibit a low La/Yb ratio (ranging from less than 4.75 to 10.27), indicating that they were formed under relatively low pressure and derived from the partial melting of their source area without residual garnet (e.g., Pan et al., 2022). The dacite samples have relatively high SiO_2 amounts (64.54–75.63 wt.%), and low to moderately low MgO content (0.46–3.01 wt.%, with an average of 1.99 wt.%). The moderate total alkali content (Na2O + K2O ≈ 5) in the dacites is almost in contrast with the typical characteristics of rocks formed from the melting of subducted fragments. The low concentrations of Cr (5-34), Ni (Less than 1 to 9), Sc (2.9-16.6), and MgO (0.46–3.01 wt.% with an average of 1.99 wt.%) in the dacites suggest a minimal influence of mantle-derived material on the magma that formed these rocks in this area (e.g., Ghadami et al., 2015). Based on the range of MgO (0.46–3.01 wt.% with an average of 1.99 wt.%) and the aforementioned geochemical characteristics, the dacitic magma is unlikely to have been directly derived from mantle melting. Experimental evidence from Roberts and Clemens (1993) demonstrated that type I high potassium calc-alkaline magmas can forme through the partial melting of intermediate to mafic calc-alkaline and high-K calc-alkaline rocks. Partial melting of crustal rocks, such as amphibolite, metagreywacke, and metapelite, produces distinct melts under varying melting conditions (Patino Douce, 1996; Alberto and Patino Douce, 1999). Consequently, to investigate the origin of the dacites in the region, a proposed diagram was used to distinguish the source protolith (Fig. 21c). According

to this diagram, the dacite samples fall within the range of mafic rocks (such as amphibolite, metabasalt, metatonalite) (Fig. 21c). Based on this evidence, it can be concluded that dacites, along with rhyolites, originated from the partial melting of a portion of the lower mafic crust under relatively high-temperature and low-pressure conditions (Pan et al., 2022). All the aforementioned evidence supports this conclusion.

- **Rhyolite**

As noted earlier, rhyolites are commonly observed alongside dacites in the study area. The primary models for the formation of felsic magmas in a volcanic arc environment include the AFC process (Bacon and Druitt, 1988) and partial melting of the lower crust due to the thermal influence of mafic magmas with a deeper or mantle origin (Guffanti et al., 1996). According to the Harker diagrams, some of the rhyolite samples follow the same evolutionary trend as the dacite rocks. This suggests that both FC and AFC processes may contribute to the formation of the rhyolites (Fig. 20a, b). However, the high SiO_2 content and the enrichment of incompatible elements such as Rb and Th are not compatible with the formation of rhyolite rocks through processes such as FC and AFC. Therefore, alternative sources for the origin of these rocks should be considered (e.g., Sarkhoshi et al., 2015). Rhyolites exhibit characteristics of calc-alkaline magmas and belong to the felsic magmas group, specifically Type I granitoids (e.g., Sarkhoshi et al., 2015). In the primitive mantle-normalized multi-element pattern, rhyolites display negative anomalies in P, Nb, and Ti, along with positive anomalies in Pb. The spider diagram curves and REE patterns across all samples reflect their shared source rocks (Li et al., 2023). In general, the rhyolites in the region are enriched in LILEs (e.g., Cs, K, Pb, and Rb) and LREE (e.g., Nd, Ce, La, and Sm), while being depleted in HFSEs (e.g., Ti, and Nb) (e.g., Sarkhoshi et al., 2015; Li et al., 2023) (Fig. 20c). In addition, the rhyolite samples exhibit a low Eu/Eu* ratio (negative anomaly) ranging from 0.49 to 0.54, indicating the presence of plagioclase in their origin or the separation of this mineral during fractionation (e.g., Barnes et al., 2001). Furthermore, the geochemical signatures suggest that the rhyolite melt was generated with a minor fraction from lower crustal depths within the plagioclase stability field (Halder et al., 2021). Geochemical features such as the enrichment of incompatible elements (K, Th, La and Ce) and negative anomalies in Nb, Ti and Ta are more compatible with melts derived from the lower crust (e.g., Sarkhoshi et al., 2015). Additionally, the abundance of LILEs such as Th, U, K, Rb, and La, along with Pb, and the depletion of Ta, Nb, and Ti have been attributed to the continental crust-origin melt (Taylor and Mclennan, 1985). To distinguish between crustal and mantle origins, the ratios of trace elements in the samples can be used. In the mantle, the $(La/Sm)_N$ and Nb/La ratios are approximately 0.01 and 1, respectively (Sun and McDonough, 1989), while in the crust, these ratios are about 4.25 and 0.23, respectively (Weaver and Tarney, 1984). In the rhyolite samples, these ratios range from 3.77 to 4.8 for $(La/Sm)_N$ and from 0.68 to 0.72 for Nb/La. These values indicate that the crust played a major role in their formation. Therefore, for further investigation, the same proposed diagram was used to differentiate the source protolith employed for the dacites. According to this diagram, the rhyolitic samples from the region, like the dacites, fall within the partial melting range of amphibolites (Fig. 21c). Eventually, it can be inferred that the rhyolite samples were most likely formed by the partial melting of a thickened lower crust (Long et al., 2015).

6.2.2. Tectono-magmatic setting

Tectonic environment differentiation diagrams are used to determine the tectonic-magmatic setting of igneous rocks. These diagrams primarily rely on variations in rare elements, using immobile or low-mobility elements. As shown in Figure 12b, most of the volcanic and pyroclastic rocks from the Rashid Abad area fall within the high-K calc-alkaline to shoshonitic series. High-K and shoshonitic magmatism characteristically occur in five different tectonic settings (Müller et al., 1992): (1) continental arcs (CAP); (2) post-collisional arcs (PAP); (3 and 4) oceanic arcs (subdivided into initial (IOP) and late (LOP)); and (5) within-plate (WIP). In this study, Zr vs. Y and Al_2O_3 vs. TiO_2 diagrams (Müller and Groves, 1997) were used to identify the tectonic setting of the magma in the rocks of this region. These diagrams indicate that the volcanic and pyroclastic rocks from the Rashid Abad area are associated with magmatic arc tectonics (Fig. 22a, b). The La/Yb vs. Th/Nb diagram (Hollocher et al., 2012) further confirmed the continental arc position of the samples from the study area (Fig. 22c). Additionally, an examination of the samples on the Schandl and Gorton (2002) diagrams (Fig. 23) shows that the volcanic and pyroclastic samples from the Rashid Abad region are located in the active continental margin areas. Finally, the Ta/Yb versus Th/Yb diagram (Pearce, 1983; Fig. 24) places the study area samples within the subduction setting and active continental margin fields.

6.2.3. Subduction and its role in the magmatism and tectonic evolution of the rocks in the study area

Igneous rocks associated with continental arcs commonly found in subduction zones along continental margins, where such tectonic settings are characterized by plate convergence (Fig. 25). These zones are typically

characterized by relatively flat subduction, as seen in the Benioff zone. The nature and propagation of magmatic activity are influenced by the type of plate convergence, the age of the subducting lithosphere, and the presence of chain-like seamounts or seismic ridges (Wilson, 1989). Furthermore, Investigations of ancient orogens indicate that continental growth can be facilitated by arc magmatism driven by plate tectonics and material accretion along convergent margins (Wu et al., 2022). Additionally, the speed rate of subduction-related magmatic activity over geological time is episodic. The key parameter in the ratio and rate of H_2O entering the sub-arc is the volume of oceanic lithosphere entering the mantle. in the ancient Earth, similar magmatic flare-ups could be associated with variability in slab flux related to supercontinent cycles (Chapman et al., 2023). Therefore, subduction zones are key locations, which causes the net growth of continents, and the long-term cycling of elements through the crust, mantle and exosphere takes place there (Hawkesworth and Kemp, 2006; Till et al., 2021). A continental arc forms at an active continental margin, where two tectonic plates converge, involving both continental and oceanic crust along the line of the plate convergence (Fig. 25). This process leads to the development of a subduction, which can be classified into two types based on the type of crust involved: (1) island-arc and (2) active continental margin (ACM). As previously mentioned, the Rashid Abad region is situated along an ACM. Geochemical and petrogenetic evidence, along with the features studied, confirm that the magmatic arc in the Rashid Abad area is associated with an active continental margin in a subduction zone. Subduction is the main process that recycles surface material into the mantle. Mantle metasomatism and refertilization are primarily driven by fluids and melts generated from the dehydration and partial melting of subducted continental crust, which acts as the main reservoir of volatiles (e.g., H_2O and CO_2) and incompatible elements (Borghini et al., 2023). The petrogenesis and magmatism of continental crust are more complex than those of oceanic arcs, as continental arcs represent a mixture of materials derived from the oceanic crust, mantle wedge, and continental crust. Moreover, primary magmas generated by the partial melting of the subducted oceanic slab are typically contaminated during their ascent through the crust (e.g., Pawley and Holloway, 1993; Eyuboglu et al., 2018). Therefore, continental magmatic arcs are characterized by the accumulation of massive mantle-derived magmatic rocks and the growth of juvenile crust (Jiang et al., 2022). Since the magmas in continental arcs result from the mixing of juvenile magmas and pre-existing crustal wall rock, the juvenile magmas are typically mafic, while the crustal wall rocks are more felsic or silicic (Chin et al., 2013). In addition, it is well established that felsic continental crust is derived from the fractionation of basaltic magmas (Keller et al., 2015). The primary sources of continental arc rocks are the mixing of existing continental crust, the lower lithosphere or lithospheric mantle beneath the continental crust, subducted oceanic crust and sediments, the mantle wedge, and underplated materials (Winter, 2001). For example, the assimilation of continental crust material acts as a vital mechanism that driving sulfide segregation and sulfide-controlled metal storage (Pieterek et al., 2024). The primary magma of the continental arcs is generated by the dehydration of the downgoing slab and partial melting of the asthenosphere together. This magma is typically composed of olivine tholeiitic basalt, resulting from a mixture of peridotites from the mantle wedge and LILE-enriched fluids from the dehydrating subducting plate (Winter, 2001). Crustal rocks in the subducting slabs also undergo metamorphic dehydration and partial melting at lithospheric depths, releasing aqueous solutions and hydrous melts that contribute to the metasomatism of the mantle wedge (e.g., Kelemen et al., 2003; Zheng et al., 2016).

Moreover, the continental crust, due to the larger thickness and lower density, prevents the upwards rising of primary magma. The continental crust inhibits the upward rise of primary magma, causing it to pond at the base of the continental crust and form a magma chamber. Moreover, due to its greater thickness and lower density, the continental crust prevents the upward rise of primary magma. This inhibition causes the magma to accumulate at the base of the continental crust, forming a magma chamber. In this chamber, an underplating process occurs, leading to the assimilation and fractional crystallization of primary magma and lower crustal rocks at the base of the crust (Pitcher et al., 1985; Winter, 2001). As a result, the olivine tholeiitic primary magma evolves into calc-alkaline magmas, as well as more differentiated, enriched alkaline or siliceous magmas (Harmon et al., 1984). Furthermore, tectonic erosion can contribute to the creation of a more enriched source by scraping and dragging the lower continental lithosphere into the melting zone. This process results in the formation of continental arc magmas with high concentrations of Rb, Cs, Ba, K, Th, and LREEs (light rare-earth elements), along with enriched isotopic compositions (Pearce and Parkinson, 1993). According to the geochemical data, rocks from Rashid Abad are mainly enriched in LREEs (e.g., Nd, Ce, La, and Sm) and LILEs (e.g., Rb, Cs, Pb, and K) but are depleted of HFSEs (e.g., Ti and Nb). Additionally, the REE patterns exhibit a negative Eu anomaly. These geochemical characteristics highlight the obvious features of a magmatic arc and magmatic activity related to subduction, resulting from the involvement of fluids released from the subducted oceanic slab in the enrichment of magma elements. Therefore, the primary magma of the Eocene andesites and andesite basalts in the study area originated from the partial melting of a spinel lherzolite source, likely undergoing AFC and MASH processes during ascent. The accumulation of mafic melts at the at the mantle-crust boundary, coupled with an increased geothermal gradient, triggered partial melting of the lower amphibolite crust, which subsequently produced dacitic and rhyolitic magmas. Hence, the primary magma of these rocks, derived from the mantle, probably underwent partial melting of the subducted oceanic crust and was metasomatized by fluids from the subducted slab. It was further contaminated by crustal material during its ascent through the crust or within a shallow-level crustal magma chamber, ultimately underwent fractional

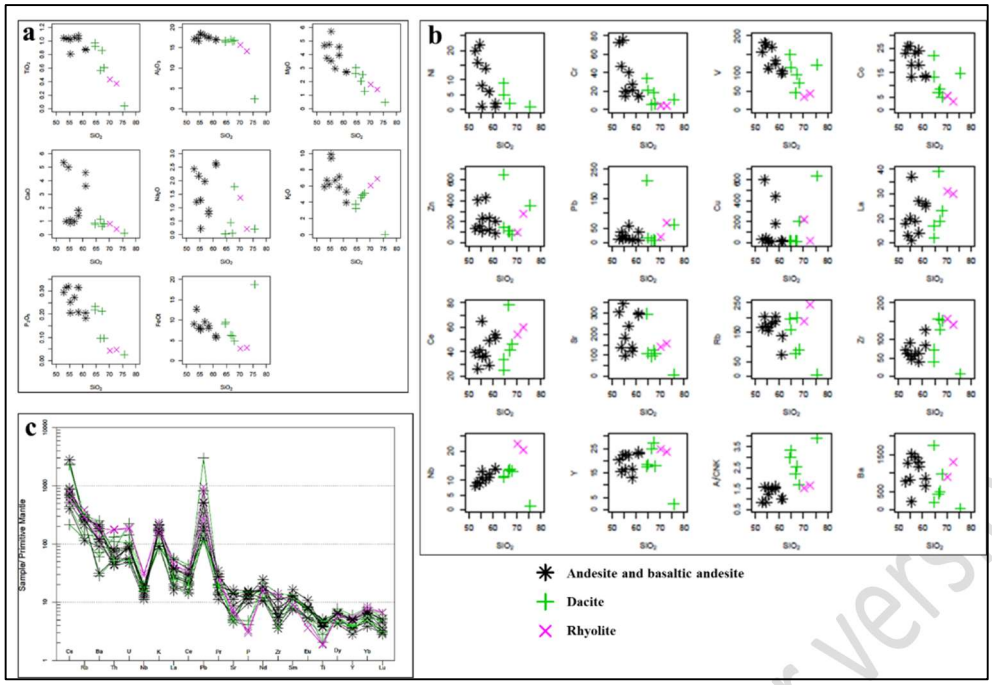

Figure 20. Rock types from the Rashid Abad region (Andesite and Basaltic andesite, Dacite and Rhyolite) plotted on: (a) Harkers' Variation diagram of SiO_2 (wt.%) versus major oxides (wt.%); (b) Harkers' Variation diagram of SiO_2 (wt.%) versus minor elements (ppm); (c) Primitive mantle-normalized spider diagrams (Sun and McDonough, 1989).

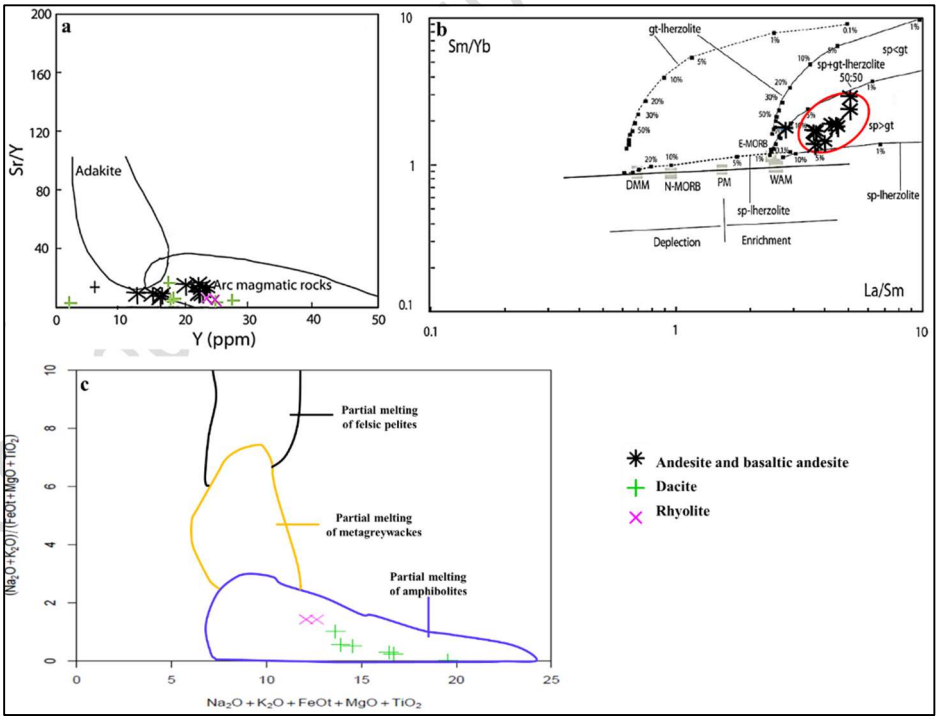

Figure 21. Rock types from the Rashid Abad area (Andesite and Basaltic andesite; Dacite and Rhyolite) plotted on: (a) Y vs. Sr/Y diagram (Defant and Drummond, 1993); (b) La/Sm vs. Sm/Yb diagram (Aldanmaz et al., 2000); (c) $Na_2O+K_2O+FeO+MgO+TiO_2$ vs. $(Na_2O+K_2O)/(FeO+MgO+TiO_2)$ diagram (Patino Douce, 1996).

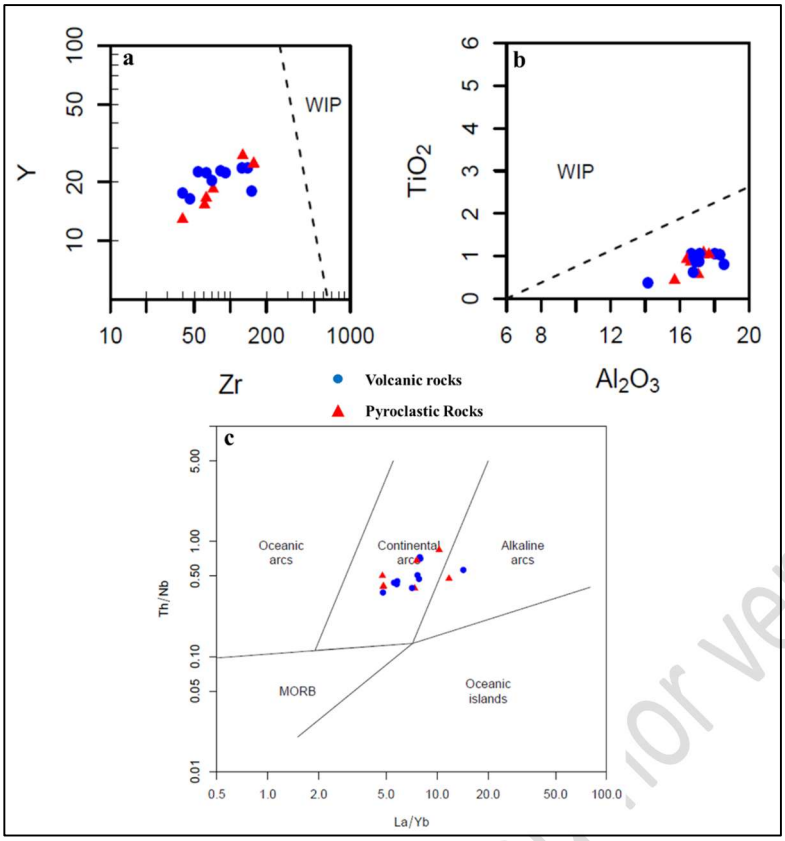

Figure 22. Rock samples from the Rashid Abad region plotted on: (a) Zr vs. Y diagram (Müller and Groves, 1997); (b) Al_2O_3 vs. TiO_2 diagram (Müller and Groves, 1997); (c) La/Yb vs. Th/Nb diagram (Hollocher et al., 2012).

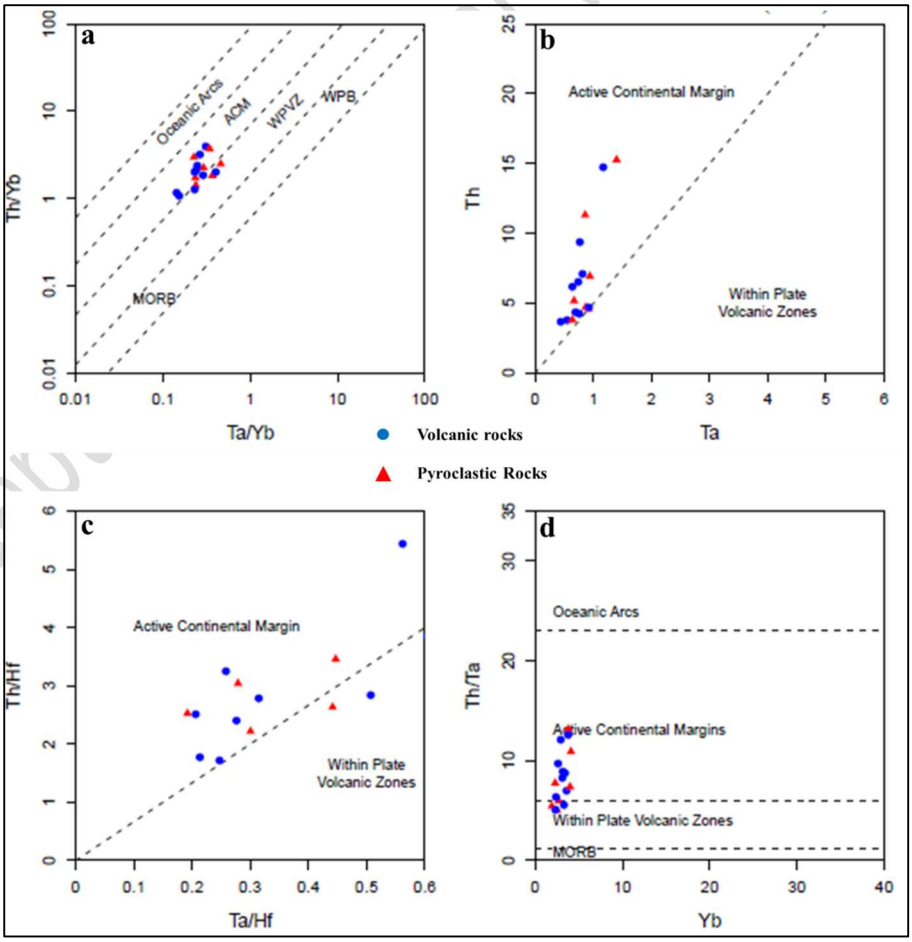

Figure 23. Rock samples from the Rashid Abad area plotted on classification diagrams by Schandl and Gorton (2002).

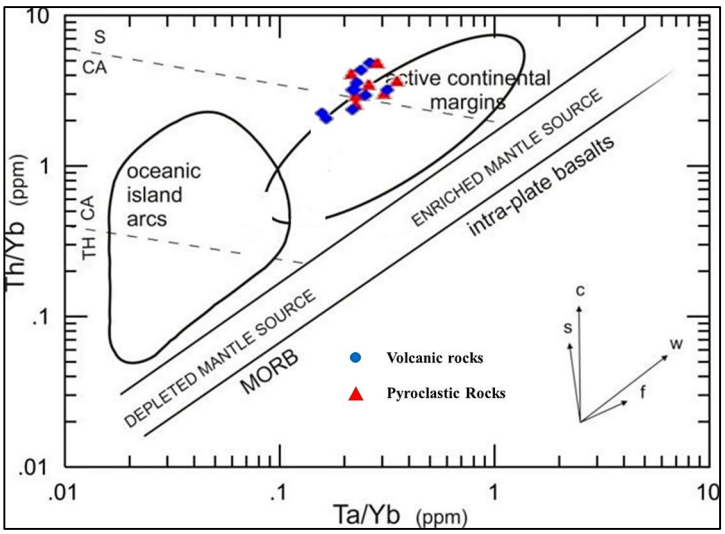

Figure 24. Rock samples from the Rashid Abad region plotted on the Ta/Yb vs. Th/Yb diagram (Pearce, 1983).

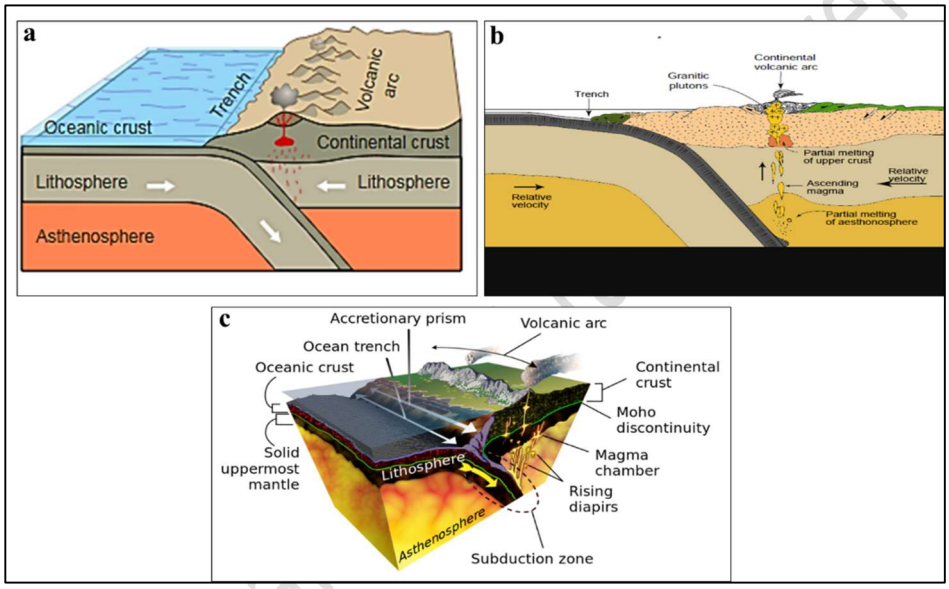

Figure 25. (a) Schematic diagram illustrating the formation of a continental arc, showing the convergence of an oceanic plate and a continental plate (Booyabazoo, 1999); (b) Cross-sectional diagram showcasing magmatic processes within a continental arc (MichaelZuo, 2014); (c) Diagram illustrating the geological process of subduction (Schroeder, 2016).

7. Conclusion

This research presents petrological and geochemical data from the Rashid Abad Eocene volcanic-pyroclastic rocks to examine their petrogenesis, tectonomagmatic setting, and magmatic evolution. The results of chemical analysis and petrographic studies indicate a combination of acidic to intermediate-basic compositions in the rocks, with the data showing a range from rhyolite to basalt. Additionally, the pyroclastic rocks are characterized by tuff types, including vitric tuff, crystal tuff, and crystal-lithic tuff. Both volcanic and pyroclastic rocks have formed in a high-K calc-alkaline to shoshonitic series. Geochemical and petrographic investigations of the area suggest that the rocks originated from fractional crystallization. Fractional crystallization is affirmed by the trends of major oxides and trace elements in relevant diagrams plotted against SiO2, as well as petrographic evidence of minerals such as plagioclase, alkali feldspar, quartz, and pyroxene. This evidence indicates that the source magma of the Rashid Abad volcanic-pyroclastic rocks was influenced by fractional crystallization (FC). According to the tectonic discrimination diagrams, the studied rocks exhibit characteristics typical of continental arc settings. Since igneous rocks associated with continental arcs are commonly found in subduction zones along continental margins, the analysis of the Rashid Abad samples

indicates that these rocks were formed in an active continental margin environment. Furthermore, the Nb/Y ratio, which is lower than 1.72 (a characteristic of active continental margins) supports this conclusion for the Rashid Abad district. In the REE plots, all the samples show enrichment in LREEs (e.g., Nd, Ce, La, and Sm) and LILE (e.g., Rb, Cs, Pb, and K), while exhibiting depletion in HREEs (e.g., Ti and Nb). In addition, the volcanic and pyroclastic rocks displaye a negative Eu anomaly. These are some of the most prominent features of magmatic arcs and a obvious characteristics of magmatic activity related to subduction, resulting from the involvement of fluids released from a subducted oceanic slab in the enrichment of magma elements. The magmatic arc characteristics and LILE enrichment in the rocks of the area indicate that the magma likely originated from a mixture of mantle and crustal material. Additionally, the magma sources may originate from a wide range of hybrid compositions formed by the mixing of various mantle and crustal melts. Negative Nb and Ti anomalies in the region's rocks suggest the possibility of crustal contamination. The Nb/U ratio (1.85 to 10), Ce/Pb ratio (0.01 to 9.75), Nb/U versus Ce/Pb ratios, and Nb/Ta ratios clearly confirm the influence of crustal contamination. Additionally, the Nb/Y versus Rb/Y ratios, which are enriched in the subduction zone, show evidence of crustal contamination. The Rb versus Ba/Rb ratio highlights the role of crustal contamination associated with fractional crystallization (FC) in the upper crust. The primary magma of the Eocene andesites and andesite basalts in the study area originated from the partial melting of a spinel lherzolite source. The accumulation of mafic melts at the boundary between the mantle and crust, along with the increase in the geothermal gradient, caused partial melting of the lower amphibolite crust. The resulting melt produced dacitic and rhyolitic magmas. Generally, it appears that the primary magma of the rocks in the study area formed in a subduction zone that underwent partial melting. This magma was subsequentlycontaminated by continental crust materials as it ascended through the crust or within a shallow-level crustal magma chamber. Ultimately, the magma underwent fractional crystallization.

References

Abdolahadi A., Sheikhzakariaee S.J., Yazdi A., Mousavi S.Z. (2025) Plio-Quaternary Adakite Genesis and Post-collisional Processes: Whole Rock Constraints and Sr, Nd Isotopic Compositions in Alborz Magmatic Belt, Ardabil, Iran. *Journal of Mining and Environmen*t 16(2):737-765. DOI: https://doi.org/10.22044/jme.2024.14781.2801

Afzali F. (2010) The study of economic geology, copper and gold mineralization in Rashtabad (Zanjan) region and its relationship with surrounding mineralizations. *MSC Thesis, Payame Noor University of Tabriz, Tabriz*, Iran.

Afzali F., Hajalilo B., Moghadasi J. (2010) Metal mineralization related to hydrothermal alteration in Rasht Abad mine northwest of Zanjan. *1st Conference of Iranian Society of Economic Geology.*

Aghajani S., Emami M.H., Lotfi M., Gholizadeh K., Ghasemi Siani M. (2016) Source of polymetal epithermal veins at Nikuyeh district (West of Qazvin) based on mineralogy, alteration and fluid inclusion studies. *Scientific Quarterly Journal of Geosciences* 25: 157–168. https://doi.org/10.22071/gsj.2016.40893

Aghajani S., Ghasemi Siani M., Emami M.H., Lotfi M., Gholizadeh K. (2020) Petrography, geochemistry, magmatic evolution and tectenomagmatic setting of igneous rocks associated with Nikuyeh epithermal mineralization (west of Qazvin). *Kharazmi Journal of Earth Sciences* 6: (1) 15–30. https://doi.org/10.52547/gnf.6.1.1

Aghanabati A. (2004) Geology of Iran. *Geological Survey of Iran* .707p. (In Persian)

Aghazadeh M., Badrzadeh Z., Castro A. (2015). Petrogenesis and U-Pb SHRIMP dating of Taroum plutons. *Scientific Quarterly Journal of Geosciences* 24; 3–20. https://doi.org/10.22071/gsj.2015.42373

Ahmadian, J. (1991) Geological and geochemical investigation of hydrothermal alteration zones with a view on the mineralization in Zakir area/southwest of Tarem. *MSC Thesis, Tabriz University*, *Tabriz*, Iran.

Ajalli N., Torkian A., Tale Fazel E. (2017) Investigatinof fluid inclusions in the deposit of copper-gold veins in Rasht Abad (north of Zanjan). *2st Conference of specialized and national on the use of fluids involved in geosciences*.

Ajalli N., Torkian A., Tale Fazel E. (2021) Geochemistry of basaltic rocks of Meshkin- Rasht Abad area (North of Zanjan). *Journal of Petrology* 45: 1-18. https://www.magiran.com/p2320776

Ajalli N., Torkian A., Tale Fazel E. (2021) Intermediate sulfidation epithermal Cu±Au deposit of RashtAbad (North of Zanjan): evidence of mineralization, fluid inclusions and C-O stable isotopeIranian. *Journal of Crystallography and Mineralogy* 29(1): 207-220. https://www.magiran.com/p2281798

Alavi M. (1994) Tectonics of the Zagros orogenic belt of Iran: new data and interpretations. *Journal of Tectonophysics* 229:211-238. https://doi.org/10.1016/0040-1951(94)90030-2

Alavi M. (1996) Tectonostratigraphic synthesis and structural style of the Alborz mountain system in northern Iran. *Journal of Geodynamics* 21:1-33. https://doi.org/10.1016/0264-3707(95)00009-7

Alberti A., Comin-Chiaramonti P., Sinigoi S., Nicoletti M., Petrucciani C. (1980) Neogene and Quaternary volcanism in Eastern Azerbaijan (Iran): some K-Ar age determinations and geodynamic implications. *Journal of Geologische Rundschau* 69:216-225. https://doi.org/10.1007/BF01869034.

Alberto E., Patino Douce A.E. (1999) What do experiments tell us about the relative contributions of crust and mantle to the origin of granitic magmas?. *Journal of the Geological Society (London, Special Publications))* 168: 55-75. https://doi.org/10.1144/GSL.SP.1999.168.01.05

Aldanmaz E., Pearce J.A, Thirlwall M., Mitchell J. (2000) Petrogenetic evolution of late Cenozoic, post-collision volcanism in western Anatolia, Turkey. *Journal of volcanology and geothermal research* 102:67-95. https://doi.org/10.1016/S0377-0273(00)00182-7

Alizadeh E., Li H., Babazadeh S., Ma C., Förster M.W. (2023) Late Eocene slab retreat, extension, and mantle upwelling inferred from mantle signatures in potassium-rich magmatism in NE Iran. *Journal of International Geology Review* 65(9), 1586–1600. https://doi.org/10.1080/00206814.2023.2185823

Allen M.B., Ghassemi M.R., Shahrabi M., Qorashi M. (2003) Accommodation of late Cenozoic oblique shortening in the Alborz range, northern Iran. *Journal of structural geology* 25:659-672. https://doi.org/10.1016/S0191-8141(02)00064-0

and Re–Os geochronology. *Journal of Ore Geology Reviews* 102: 757–775. https://doi.org/10.1016/j.oregeorev.2018.10.007

Ashrafi, N; Dabiri, R and Jahangiri, A. (2024) Some chemical variations in biotite, phlogopite, and muscovite, considering their tectonic setting. *Geopersia* 14(2): 307-32. DOI: https://doi.org/10.22059/geope.2024.373882.648749

Asiabanha A., Foden J. (2012) Post-collisional transition from an extensional volcano-Sedimentary basin to a continental arc in the Alborz Ranges, N-Iran. *Journal of Lithos*, 148: 98-111. https://doi.org/10.1016/j.lithos.2012.05.014

Askren D.R., Roden M.F., Whitney J.A. (1997) Petrogenesis of Tertiary andesite lava flows interlayered with large-volume felsic ash-flow tuffs of the western USA. *Journal of Petrology* 38:1021-1046. https://doi.org/10.1093/petroj/38.8.1021

Aydınçakır E. (2014) The petrogenesis of Early Eocene non-adakitic volcanism in NE Turkey: Constraints on the geodynamic implications. *Journal of Lithos* 208:361-377. https://doi.org/10.1016/j.lithos.2014.08.019

Azizi H., Asahara Y. (2013) Juvenile granite in the Sanandaj–Sirjan Zone, NW Iran: late Jurassic–early Cretaceous arc–continent collision. *Journal of International Geology Review* 55:1523-1540. https://doi.org/10.1080/00206814.2013.782959

Azizi H., Moinevaziri H. (2009) Review of the tectonic setting of Cretaceous to Quaternary volcanism in northwestern Iran. *Journal of Geodynamics* 47:167-179. https://doi.org/10.1016/j.jog.2008.12.002

Azizi H., Moinevaziri H., Mohajjel M., Yagobpoor A. (2006) PTt path in metamorphic rocks of the Khoy region (northwest Iran) and their tectonic significance for Cretaceous–Tertiary continental collision. *Journal of Asian Earth Sciences* 27:1-9. https://doi.org/10.1016/j.jseaes.2004.12.007

Azizi H., Stern R.J, Topuz G., Asahara Y., Moghadam H.S. (2019) Late Paleocene adakitic granitoid from NW Iran and comparison with adakites in the NE Turkey: Adakitic melt generation in normal continental crust. *Journal of Lithos* 346:105151. https://doi.org/10.1016/j.lithos.2019.105151

Bacon C.R., Druitt T.H. (1988) Compositional evolution of the zoned calcalkaline magma chamber of mount Mazama, Crater Lake, Oregon. *Journal of Contribution to Mineralogy and Petrology* 98: 224-256. https://doi.org/10.1007/BF00402114

Ballato P., Uba C.E., Landgraf A., Strecker M.R., Sudo M., Stockli D.F., Friedrich A., Tabatabaei S.H. (2010) Arabia-Eurasia continental collision: Insights from late Tertiary foreland-basin evolution in the Alborz Mountains, northern Iran. *Journal of Geological Society of America Bulletin*123:106-131. https://doi.org/10.1130/B30091.1

Baranpurian N., Emami M.H., Vossoughi Abedini M., Dabiri R. (2014) Mineral Chemistry and Thermobarometry of the Upper Eocene Volcanic Rocks in NE Tafresh, Iran. *Open Journal of Geology* 4(12): 612-621. DOI: http://dx.doi.org/10.4236/ojg.2014.412045

Barnes S.J., Achterbergh E., Makovicky E., Li C. (2001) Proton probe results for partitioning of platinum group elements between monosulphide solid solution and sulphide liquid. *South African Journal of Geology* 104:275-286. https://doi.org/10.2113/gssajg.104.4.275

Barth M. G., McDonough W. F., Rudnick R. L. (2000) Tracking the budget of Nb and Ta in the continental crust. *Journal of Chemical Geology* 165, 197–213. https://doi.org/10.1016/S0009-2541(99)00173-4

Berberian M. (1993) Tectonic Map of Iran Scale 1:1500000, In: Continental Deformation in the Iranian Plateau, Contribution to the Seismotectonics of Iran, Part IV. *Geological Survey Iran* (*Tehran*), 52 p.

Berberian M., King G. (1981) Toward a palegeography and tectonic evolution of Iran, *Canadian Journal of Earth Sciences* 18:210-265. https://doi.org/10.1139/e81-019

Blourian G.H. (1994) Petrology of Tertiary volcanic rocks in the north of Tehran. *MSC Thesis, Tarbiat Moallem University*, Tehran, Iran, 145 pp.

Booyabazoo (1999) Schematic diagram of the formation of a continental arc- showing convergence of an oceanic plate and a continental plate. *Wikimedia.* https://en.wikipedia.org/wiki/Continental_arc#/media/File:Active_Margin.svg

Borghini A., Nicoli G., Ferrero S., O'brien P.J., Laurent O., Remusat L., Borghini G., Milani S. (2023) The role of continental subduction in mantle metasomatism and carbon recycling revealed by melt inclusions in UHP eclogites. *Journal of Science Advances* 9:eabp9482. https://doi.org/10.1126/sciadv.abp9482

Boynton W.V. (1984) Cosmochemistry of the rare earth elements: meteorite studies. *Journal of Developments in geochemistry* 2:63-114 https://doi.org/10.1016/B978-0-444-42148-7.50008-3

Brunet M.F., Korotaev M.V., Ershov A.V., Nikishin A.M. (2003) The South Caspian Basin: a review of its evolution from subsidence modelling. *Journal of Sedimentary geology* 156:119-148. https://doi.org/10.1016/S0037-0738(02)00285-3

Cambeses A., Garcia-Casco A., Molina J., Montero P., Basak S., Morales I., Bea F. (2021) The roles of partial melting of metasomatised mantle, magma mixing at continental crust level and fractionation in calc-alkaline minette genesis, SE Spain. *Journal of International Geology Review*:1-41. https://doi.org/10.1080/00206814.2021.1998798

Castro A., Aghazadeh M., Badrzadeh Z., Chichorro M. (2013) Late Eocene–Oligocene post-collisional monzonitic intrusions from the Alborz magmatic belt, NW Iran. An example of monzonite magma generation from a metasomatized mantle source. *Journal of Lithos* 180:109-127. https://doi.org/10.1016/j.lithos.2013.08.003

Chapman T., Milan L. A., Zahirovic S., Merdith A. S., Clarke G. L., Sun M., Daczko N.R. (2024) Magmatic flare-ups in arcs controlled by fluctuations in subduction water flux. *Journal of Tectonophysics* 888: 230457. https://doi.org/10.1016/j.tecto.2024.230457

Chazot G., Abbassene F., Maury R.C., Déverchère J., Bellon H., Ouabadi A., Bosch D. (2017) An overview on the origin of post-collisional Miocene magmatism in the Kabylies (northern Algeria): evidence for crustal stacking, delamination and slab detachment. *Journal of African Earth Sciences* 125:27-41. https://doi.org/10.1016/j.jafrearsci.2016.10.005

Chen L. (2021) The role of lower crustal rheology in lithospheric delamination during orogeny. *Journal of Frontiers in Earth Science* 9:755519. https://doi.org/10.3389/feart.2021.755519

Chen L., Zheng Y.F., Xu Z., Zhao Z.F. (2021) Generation of andesite through partial melting of basaltic metasomatites in the mantle wedge: Insight from quantitative study of Andean andesites. *Journal of Geoscience Frontiers* 12:101-124. https://doi.org/10.1016/j.gsf.2020.12.005

Chichaki Gh., Mokhtari M.A.A. (2002) Investigation of economic geology of Armaghanekhane - Rashid Abad region (northeast of Zanjan). *5th Conference of the Geological Society of Iran.*

Chin E.J., Lee C.TA., Tollstrup D.L., Xie L., Wimpenny J.B., Yin Q.Z. (2013) On the origin of hot metasedimentary quartzites in the lower crust of continental arcs. *Journal of Earth and Planetary Science Letters* 361:120-133. https://doi.org/10.1016/j.epsl.2012.11.031

Clark G. C., Davis R. G., Hamzehpour B., Jones C. R. (1975) Explanatory text of the Bandar-e-Anzali quadrangle map, scale 1:250,000. Geological Survey of Iran, pp. 198.

Çoban H., Karacık Z., Ece Ö.I. (2012) Source contamination and tectonomagmatic signals of overlapping Early to Middle Miocene orogenic magmas associated with shallow continental subduction and asthenospheric mantle flows in Western Anatolia: a record from Simav (Kütahya) region. *Journal of Lithos* 140:119-141. https://doi.org/10.1016/j.lithos.2011.12.006

Dabiri, R., Akbari-Mogaddam, M., Ghaffari, M. (2018) Geochemical evolution and petrogenesis of the Eocene Kashmar granitoid rocks, NE Iran: Implications for fractional crystallization and crustal contamination processes. *Iranian Journal of Earth Sciences* 10(1):68-77.

Dagva-Ochir L., Oyunchimeg T., Otgonbaatar D., Enkhdalai B., Battushig A. (2019) Middle Paleozoic oceanic basalts from the Tsoroidog Uul area hosted by the Tsetserleg accretionary terrane, Central Mongolia. *Conference: IGCP -662 Project OROGENIC ARCHITECTURE AND CRUSTAL GROWTH FROM ACCRETION TO COLLISION Field Guide*. https://doi.org/10.13140/RG.2.2.18916.32646

Dagva-Ochira, L., Oyunchimeg, T.U., Enkhdalai, B., Safonova, I., Li, H., Otgonbaatar, D., Soh Tamehea, L., Sharav, D. (2020) Middle Paleozoic intermediate-mafic rocks of the Tsoroidog Uul' accretionary complex, Central Mongolia: Petrogenesis and tectonic implications. *Journal of Lithos* 376–377, 105795. https://doi.org/10.1016/j.lithos.2020.105795

Defant M.J., Drummond M.S. (1993) Mount St. Helens: Potential example of the partial melting of the subducted lithosphere in a volcanic arc. *Journal of Geology* 21: 547-550. https://doi.org/10.1130/0091-7613(1993)021<0547:MSHPEO>2.3.CO;2

Dungan M.A., Davidson J. (2004) Partial assimilative recycling of the mafic plutonic roots of arc volcanoes: An example from the Chilean Andes. *Journal of Geology* 32: 773–776. https://doi.org/10.1130/G20735.1

Earth–Moon system from Nb/Ta systematics. *Journal of Science* 301: 84–87. https://doi.org/10.1126/science.1084662

EDWARDS C.M., MENZIES M.A., THIRLWALL M.F., MORRIS J.D., LEEMAN W.P., HARMON R.S. (1994) The transition to potassic alkaline volcanism in Island Arcs: the Ringgit—Beser complex, East Java, Indonesia. *Journal of Petrology* 35:1557-1595. https://doi.org/10.1093/petrology/35.6.1557

Eftekhar Nezhad J. (1980) Separation of different parts of Iran in terms of structural status in relation to sedimentary basins. *Petroleum Society Journal* 82: 19-28.

Eriksson P.G., Altermann W., Nelson D.R., Mueller W.U., Catuneanu O. (2004) The Precambrian Earth. *Developments in Precambrian Geology Series*12: 941 pp.

Ersoy E.Y., Palmer M.R., Genç Ş.C., Prelević D., Akal C., Uysal İ. (2017) Chemo-probe into the mantle origin of the NW Anatolia Eocene to Miocene volcanic rocks: Implications for the role of, crustal accretion, subduction, slab roll-back and slab break-off processes in genesis of post-collisional magmatism. *Journal of Lithos* 288:55-71. https://doi.org/10.1016/j.lithos.2017.07.006

Esmaeli M., Lotfi M., Nezafati N. (2015) Fluid inclusion and stable isotope study of the

Esmaeli M., Lotfi M., Nezafati N. (2019) Mineralogy, and genesis of Khalyfehlou copper deposit based on host rock geochemical data and O-S isotope characteristic. *Scientific Quarterly Journal of Geosciences* 28: 33–46. https://doi.org/10.22071/gsj.2019.84248

Eyuboglu Y., Dudas F.O., Santosh M., Eroğlu-Gümrük T., Akbulut K., Yi K., Chatterjee N. (2018) The final pulse of the Early Cenozoic adakitic activity in the Eastern Pontides Orogenic Belt (NE Turkey): An integrated study on the nature of transition from adakitic to non-adakitic magmatism in a slab window setting. *Journal of Asian Earth Sciences* 157:141-165. https://doi.org/10.1016/j.jseaes.2017.07.004

Fan W.M., Guo F., Wang Y.J., Lin G. (2003) Late Mesozoic calc-alkaline volcanism of post-orogenic extension in the northern Da Hinggan Mountains, northeastern China. *Journal of volcanology and geothermal research* 121:115-135. https://doi.org/10.1016/S0377-0273(02)00415-8

Faridi M., Anvari A. (1996) Geological Map of Hashtjin, scale 1:100,000 (N 5664). *Iran Geological Survey*, Tehran.

Feyzi M., Ebrahimi M., Kouhestani H., Mokhtari M.A.A. (2016). Geology, mineralization and geochemistry of the Aqkand Cu occurrence (north of Zanjan, Tarom-Hashtjin zone). *Journal of Economic geology* 8:507–524. https://10.22067/ECONG.V8I2.49150

Furman T. (2007) Geochemistry of East African Rift basalts: an overview. *Journal of African Earth Sciences* 48:147-160. https://doi.org/10.1016/j.jafrearsci.2006.06.009

G. Soder C., Dunga J., L. Romer R. (2024) Continental subduction controls regional magma heterogeneity and distribution of porphyry deposits in post-collisional settings. *Journal of Geochimica et Cosmochimica* Acta 375: 217-228. https://doi.org/10.1016/j.gca.2024.04.015

Geology 120, 347–359. https://doi.org/10.1016/0009-2541(94)00145-X

Gerya T.V., Bercovici D., Becker T.W. (2021) Dynamic slab segmentation due to brittle–ductile damage in the outer rise. *Journal of Nature* 599:245-250. https://doi.org/10.1038/s41586-021-03937-x

Ghadami Gh.R., Poosti M., Babai F. (2015) Petrogenesis of Mio-Pliocene Dacite-Andesite in SE of Urumieh-Dokhtar Magmatic Belt, (NE Shahr-e-Babak). *Scientific Quarterly Journal of Geosciences* 25(97):37-48. https://doi.org/10.22071/gsj.2015.41350

Ghasemi Siani M., Lentz D.R., Nazarian M. (2020) Geochemistry of igneous rocks associated with mineral deposits in the Tarom-Hashtjin metallogenic province, NW Iran: An analysis of the controls on epithermal and related porphyry-style mineralization. *Journal of Ore Geology Reviews* 126:103753. https://doi.org/10.1016/j.oregeorev.2020.103753

Ghasemi Siani M., Mehrabi B., Azizi H., Wilkinson C.M., Ganerød M. (2015) Geochemistry and geochronology of the volcano-plutonic rocks associated with the Glojehepithermal gold mineralization, NW Iran. *Journal of Open Geosciences* 7:207-222. https://doi.org/10.1515/geo-2015-0024

Ghasemi Siani M., Mehrabi B., Nazarian M., Lotfi M., Corfu F. (2022) Geology and genesis of the Chomalu polymetallic deposit, NW Iran. *Journal of Ore Geology Reviews* 143: 104763. https://doi.org/10.1016/j.oregeorev.2022.104763

Ghorbani M. (2007) Economic geology of mineral and natural resources of Iran. *Arian Zamin,* Tehran, 515pp.

Gill J.B. (1981) Orogenic Andesites and plate Tectonics. *Springer,* New York. https://doi.org/10.1007/978-3-642-68012-0

Goss A.R., Kay S.M. (2009) Extreme high field strength element (HFSE) depletion and near-chondritic Nb/Ta ratios in Central Andean adakite-like lavas (~ 28° S,~ 68° W). *Journal of Earth and Planetary Science Letters* 279:97-109. https://doi.org/10.1016/j.epsl.2008.12.035

Green T.H. (1995) Significance of Nb/Ta as an indicator of geochemical processes in the crust mantle system. *Jornal of Chemical*

Guffanti M., Clynne M.A., Muffler L-J.P. (1996) Thermal and mass implications of magmatic evolution in the Lassen volcanic region, California, and minimum constraints on basalt influx to the lower crust, *Journal of Geophysical Research* 101: 148-227. https://doi.org/10.1029/95JB03463

Hajalilo B, Khakzad A. (1999) Investigation of Bolaghi and Rashtabad copper mines mineralization based on fluid inclusions studies *Journal of Earth Science*, 7: no. 29-30.

Hajalilo B. (1999) Tertiary metallogeny of western Alborz-Azerbaijan (Miyaneh-Siahrood), in particular Hashtjin district, 4*th Conference of the Geological Society of Iran* 323-331.

Halder M., Paul D., Sensarma S. (2021) Rhyolites in continental mafic Large Igneous Provinces: Petrology, geochemistry and petrogenesis. *Journal of Geoscience Frontiers* 12:53-80. https://doi.org/10.1016/j.gsf.2020.06.011

Harmon R.S., Barreiro B.A. (1984) Andean Magmatism: Chemical and Isotopic Constraints. *Shiva Geology Series (Boston, Birkhäuser)* 252 pp. https://doi.org/10.1007/978-1-4684-7335-3

Harris N.B.W., Pearce J. A., Tindle A. G. (1986) Geochemical Characteristics of Collision-Zone Magmatism. In: Coward M. P., Reis A. C., eds., Collision Tectonics. *Journal of the Geological Society (London, Special Publications)* 19: 67–81 https://doi.org/10.1144/GSL.SP.1986.019.01.04

Hassanzadeh J, Ghazi A, Axen G, Guest B (2002) Olig-omiocene mafic-alkaline magmatism north and northwest of Iran: Evidence for the separation of the Alborz from the Urumieh–Dokhtar magmatic arc. *Journal of Geological Society of America Abstracts with Programs* 34: 331 pp.

Hawkesworth C. J., Kemp A. I. S. (2006) Evolution of the continental crust. *Journal of Nature* https://doi.org/10.1038/nature05191.

He C., Dong S., Wang Y. (2019) Lithospheric delamination and upwelling asthenosphere in the Longmenshan area: insight from teleseismic P-wave tomography. *Journal of Scientific Reports* 9:6967. https://doi.org/10.1038/s41598-019-43476-0

He Q., Zhang S.B., Zheng Y.F., Chen R.X. (2022) Peritectic minerals record partial melting of the deeply subducted continental crust in the Sulu orogen. *Journal of Metamorphic Geology* 40:87-120. https://doi.org/10.1111/jmg.12620

Hoffmann J. E., Munker C., Naeraa T., Rosing M. T., Herwartz D., Garbe-Schonberg D., Svahnberg H. (2011). Mechanisms of Archean crust formation inferred from highprecision HFSE systematics in TTGs. *Journal of Geochimica et Cosmochimica Acta* 75:4157–4178. https://doi.org/10.1016/j.gca.2011.04.027

Hofmann A.W. (1986) Nb in Hawaiian magmas: constraints on source composition and evolution. *Journal of Chemical Geology* 57:17-30. https://doi.org/10.1016/0009-2541(86)90091-4

Hofmann A.W., Jochum K.P., Seufert M., White W.M. (1986) Nb and Pb in oceanic basalts: new constraints on mantle evolution. *Journal of Earth and Planetary science letters* 79:33-45. https://doi.org/10.1016/0012-821X(86)90038-5

Hollingsworth J., Fattahi M., Walker R., Talebian M., Bahroudi A., Bolourchi M.J., Jackson J., Copley A. (2010) Oroclinal bending, distributed thrust and strike-slip faulting, and the accommodation of Arabia–Eurasia convergence in NE Iran since the Oligocene. *Geophysical Journal International* 181:1214-1246. https://doi.org/10.1111/j.1365-246X.2010.04591.x

Hollocher K., Robinson P., Walsh E., Roberts D. (2012) Geochemistry of amphibolite-facies volcanics and gabbros of the Støren Nappe in extensions west and southwest of Trondheim, Western Gneiss Region, Norway: a key to correlations and paleotectonic settings. *American Journal of Science* 312:357-416. https://doi.org/10.2475/04.2012.01

Hosseinzadeh M.R., Moghfouri M., Moayyed M., Rahmani A. (2016) Khalifehlu deposit high-sulfidation epithermal Cu-Au mineralization in the Tarom magmatic zone, North Khoramdareh. *Scientific Quarterly Journal of Geosciences* 25: 179–194. https://doi.org/10.22071/gsj.2016.40910

https:// doi.org /10.1127/njma/2017/0036

https://doi.org/10.1016/j.oregeorev.2019.05.014

Huang F, Xu J, Zeng Y, Chen J, Wang B, Yu H, Chen L, Huang W, Tan R (2017) Slab breakoff of the Neo-Tethys Ocean in the Lhasa Terrane inferred from contemporaneous melting of the mantle and crust, *Geochemistry, Geophysics, Geosystems* 18:4074-4095. https://doi.org/https://doi.org/10.1002/2017GC007039

in garnets of the Aghblag iron-copper skarn, West-Azarbaija province. *Scientific Quarterly Journal of Geosciences* 30(3): 265-274. https://doi.org/10.22071/gsj.2019.187341.1660

in the Sangan mining region NE Iran. *Journal of Ore Geology Reviews* 84: 116-133. https://doi.org/10.1016/j.oregeorev.2017.01.003

Irvine T.N., Baragar W. (1971) A guide to the chemical classification of the common volcanic rocks. *Canadian journal of earth sciences* 8:523-548. https://doi.org/10.1139/e71-055

Ji Z., Zhang Y.L., Wan C.B., Ge W.C., Yang H., Dong Y., Jing Y. (2021) Recycling of crustal materials and implications for lithospheric thinning: Evidence from Mesozoic volcanic rocks in the Hailar–Tamtsag Basin, NE China. *Journal of Geoscience Frontiers* 12:101-184. https://doi.org/10.1016/j.gsf.2021.101184

Jiang Y.Y., Zhang Z.M., Palin R.M., Ding H.X., Mo X.X. (2022) Early Cenozoic partial melting of meta-sedimentary rocks of the eastern Gangdese arc, southern Tibet, and its contribution to syn-collisional magmatism. *Journal of Geological Society of America Bulletin* 134:179-200. https://doi.org/10.1130/B35763.1

Jochum K.P., Stolz J., McOrist G. (2000) Niobium and tantalum in carbonaceous chondrites : constraints on the Solar System and primitive mantle niobium/tantalum, zirconium/niobium, and niobium/uranium ratios. *Journal of Meteoritics and Planetary Science* 35, 229-235. https://doi.org/10.1111/j.1945-5100.2000.tb01771.x

Kamber B.S., Ewart A., Collerson K.D., Bruce M.C., McDonald G.D. (2002) Fluid-mobile trace element constraints on the role of slab melting and implications for Archaean crustal growth models. *Journal of Contributions to Mineralogy and Petrology* 144:38-56. https://doi.org/10.1007/s00410-002-0374-5

Kelemen P.B., Koga K., Shimizu N. (1997) Geochemistry of gabbro sills in the crust-mantle transition zone of the Oman ophiolite: Implications for the origin of the oceanic lower crust. *Journal of Earth and Planetary Science Letters* 146:475-488. https://doi.org/10.1016/S0012-821X(96)00235-X

Kelemen P.B., Rilling J.L., Parmentier E., Mehl L., Hacker B.R. (2003) Thermal structure due to solid-state flow in the mantle wedge beneath arcs. *Journal of Geophysical Monograph Series (American Geophysical Union)* 138:293-311. https://doi.org/10.1029/138gm13

Kelemen P.B., Shimizu N., Dunn J.T. (1993) Relative depletion of niobium in some arc magmas and the continental crust: Partitioning of K, Nb, La and Ce during melt/rock reaction in the upper mantle. *Journal of Earth and Planetary Science Letters* 120: 111-133. https://doi.org/10.1016/0012-821X(93)90234-Z

Keller C.B., Schoene B., Barboni M., Samperton K.M., Husson J.M. (2015) Volcanic–plutonic parity and the differentiation of the continental crust. *Journal of Nature* 523:301-307. https://doi.org/10.1038/nature14584

Khajehmohammadlou N., Calagari A.A., Siahcheshm K., Abedini A. (2020) Geochemistry of major and rare earth elements

Khalyfehlou copper deposit, southeast Zanjan, Iran. *Arabian Journal of Geosciences* 8: 9625–9633. https://doi.org/10.1007/s12517-015-1907-3

Kharazmi University 1 (2) :155-178. https://doi.org/10.29252/gnf.1.2.155

Königer S., Lorenz V. (2002) Geochemistry, tectonomagmatic origin and chemical correlation of altered Carboniferous-Permian fallout ash tuffs in southwestern Germany. *Journal of Geological Magazine* 139:541–558. https://doi.org/10.1017/S0016756802006775

Kouhestani H., Azimzadeh A.M., Mokhtari M.A.A., Ebrahimi M. (2017) Mineralization and fluid evolution of epithermal base metal veins from the Aqkand deposit, NW Iran. *Journal of Mineralogy and Geochemistry* 194: 139–155.

Kouhestani H., Mokhtari M.A.A., Chang Z., Johnson C.A. (2018a) Intermediate sulfidation type base metal mineralization at Aliabad-Khanchy, Tarom-Hashtjin metallogenic belt, NW Iran. *Journal of Ore Geology Reviews* 93: 1–18. https:// doi.org /10.1016/j.oregeorev.2017.12.012

Kouhestani H., Mokhtari M.A.A., Chang Z., Stein H.J., Johnson C.A. (2018b). Timing and genesis of ore formation in the Qarachilar Cu-Mo-Au deposit, Ahar-Arasbaran metallogenic zone, NW Iran: Evidence from geology, fluid inclusions, O-S isotopes

Kouhestani H., Mokhtari M.A.A., Qin K., Zhao J. (2019) Fluid inclusion and stable isotope constraints on ore genesis of the Zajkan epithermal base metal deposit, Tarom-Hashtjin metallogenic belt, NW Iran. *Journal of Ore Geology Reviews* 109: 564–584.

Kovalenko V., Naumov V., Girnis A., Dorofeeva V., Yarmolyuk V. (2010) Average composition of basic magmas and mantle sources of island arcs and active continental margins estimated from the data on melt inclusions and quenched glasses of rocks. *Journal of Petrology* 18:1-26. https://doi.org/10.1134/S0869591110010017

Kretz R. (1983) Symbols of rock-forming minerals. *Journal of American Mineralogist* 68, 277–279.

Kufner S.K., Kakar N., Bezada M., Bloch W., Metzger S., Yuan X., Mechie J., Ratschbacher L., Murodkulov S., Deng Z., Schurr B. (2021) The Hindu Kush slab break-off as revealed by deep structure and crustal deformation. *Journal of Nature communications* 12:1685. https://doi.org/10.1038/s41467-021-21760-w

Küster D., Harms U. (1998) Post-collisional potassic granitoids from the southern and northwestern parts of the Late Neoproterozoic East African Orogen: a review. *Journal of Lithos* 45:177-195. https://doi.org/10.1016/S0024-4937(98)00031-0

Le Bas M.J., Le Maitre R.W., Streckeisen A., Zanettin B. (1986) A chemical classification of volcanic rocks based on the total alkali-silica diagram. *Journal of petrology* 27:745-750. https://doi.org/10.1093/petrology/27.3.745

Li H., Xi X.S., Sun H.S., Kong H., Wu Q.H., Wu C.M., Gabo-Ratio J.A.S. (2016) Geochemistry of the Batang Group in the Zhaokalong area, Yushu, Qinghai: Implications for the Late Triassic tectonism in the northern Sanjiang region, China. *Journal of Acta Geologica Sinica (English Edition)* 90: 704–721. https://doi.org/10.1111/1755-6724.12699

Li L., Xiong X.L., Liu X.C. (2017) Nb/Ta Fractionation by Amphibole in Hydrous Basaltic Systems: Implications for Arc Magma Evolution and Continental Crust Formation. *Journal of Petrology* 58, 3–28. https://doi.org/10.1093/petrology/egw070

Li X.H., Li Z.X., Li W.X., Liu Y., Yuan C., Wei G., Qi C. (2007) U–Pb zircon, geochemical and Sr–Nd–Hf isotopic constraints on age and origin of Jurassic I- and A-type granites from central Guangdong, SE China: A major igneous event in response to foundering of a subducted flat-slab?. *Journal of Lithos* 96:186-204. https://doi.org/10.1016/j.lithos.2006.09.018

Li Z., Pei X., Pei L., Liu C., Xu L., Li R., Lin H., Wang M., Ji S., Qin L., Yang Y., Wang M., Zhao S., Chen Y. (2023) Petrogenesis and Geochronology of A1-Type Rhyolites in the Late Late Triassic of the East Kunlun Orogenic Belt: Constraints on the End of the Paleo-Tethys Orogenic Event. *Journal of Minerals* 13(2): 290. https://doi.org/10.3390/min13020290

Litvak V.D., Spagnuolo M.G., Folguera A., Poma S., Jones R.E., Ramos V.A. (2015) Late Cenozoic calc-alkaline volcanism over the Payenia shallow subduction zone, South-Central Andean back-arc (34°30′–

37°S), Argentina. *Journal of South American Earth Sciences* 64:365-380. https://doi.org/10.1016/j.jsames.2015.09.010

Liu H.Q., Xu Y.G., Tian W., Zhong Y.T., Mundil R., Li X.H., Yang Y.H., Luo Z.Y., Shang-Guan S.M. (2014) Origin of two types of rhyolites in the Tarim Large Igneous Province: Consequences of incubation and melting of a mantle plume. *Journal of Lithos* 204:59-72. https://doi.org/10.1016/j.lithos.2014.02.007

Liu S., Hu R., Gao S., Feng C., Huang Z., Lai S., Yuan H., Liu X., Coulson I.M., Feng G., Wang T., Qi Y. (2009) U–Pb zircon, geochemical and Sr–Nd–Hf isotopic constraints on the age and origin of Early Palaeozoic I-type granite from the Tengchong–Baoshan Block, Western Yunnan Province, SW China. *Journal of Asian Earth Sciences* 36:168-182. https://doi.org/10.1016/j.jseaes.2009.05.004

Long X., Wilde S.A., Wang Q., Yuan C., Wang X.C., Li J., Jiang Z., Dan W. (2015) Partial melting of thickened continental crust in central Tibet: Evidence from geochemistry and geochronology of Eocene adakitic rhyolites in the northern Qiangtang Terrane. *Journal of Earth and Planetary Science Letters* 414:30-44. https://doi.org/10.1016/j.epsl.2015.01.007

Lopes de Macêdo I.M., Geraldes M.C., de Abreu Marques R., Gonzaga de Melo M., Tavares A.D., Alves Martins M.V., Oliveira H.C., Rodrigues R.D. (2022) New clues for magma-mixing processes using petrological and geochronological evidence from the Castelo Intrusive Complex, Araçuaí Orogen (SE Brazil). *Journal of South American Earth Sciences* 115:103758. https://doi.org/10.1016/j.jsames.2022.103758

Marchesi C., Garrido C.J., Godard M., Proenza J.A., Gervilla F., Blanco-Moreno J. (2006) Petrogenesis of highly depleted peridotites and gabbroic rocks from the Mayarí-Baracoa Ophiolitic Belt (eastern Cuba). *Journal of Contributions to Mineralogy and Petrology* 151:717-736. https://doi.org/10.1007/s00410-006-0089-0

Mazhari N., Malekzadeh Shafaroudi A., Ghaderi M., Lackey J. S., Farmer G.L., Karimpour M.H. (2017) Geochronological and geochemical characteristics of fractionated I-type granites associated with the skarn mineralization

Mehrabi B., Ghasemi Siani M., Goldfarb R., Azizi H., Ganerod M., Marsh E.E. (2016) Mineral assemblages, fluid evolution, and genesis of polymetallic epithermal veins, Glojeh district, NW Iran. *Journal of Ore Geology Reviews* 78:41-57. https://doi.org/10.1016/j.oregeorev.2016.03.016

Menke W., Lamoureux J., Abbott D., Hopper E., Hutson D., Marrero A. (2018) Crustal heating and lithospheric alteration and erosion associated with asthenospheric upwelling beneath southern New England (USA). *Journal of Geophysical Research: Solid Earth* 123:8995-9008. https://doi.org/10.1029/2018JB15921

MichaelZuo (2014) Cross-sectional diagram of magmatic processes in a continental arc. *Wikimedia.* https://commons.wikimedia.org/wiki/File:Continental_Arc_Sketch.jpg

Middlemost E.A. (1994) Naming materials in the magma/igneous rock system. *Journal of Earth-science reviews* 37:215-224. https://doi.org/10.1016/0012-8252(94)90029-9

Miyashiro A. (1978) Nature of alkalic volcanic rock series. *Journal of Contributions to Mineralogy and Petrology* 66:91-104. https://doi.org/10.1007/BF00376089

Moayyed M. (1991) Petrographic and Petrochemical Study of Volcano-Plutonic Belt Rocks of Tarem Region in relation to Copper Genesis. *MSC thesis, University of Tabriz*, Tabriz, Iran.

Moayyed M. (2001) Geochemistry and petrology of volcano-plutonic bodies in Tarum area. *PhD thesis, University of Beheshti*, Tehran, Iran.

Mohammadi S.S, Nakhaei M. (2022) Geometric properties, petrography, geochemistry and tectonic setting of columnar andesites of Goorid quarry rubble mine, west of Sarbisheh city (South Khorasan). *Petrological Journal* 13(3): 33-62. https://doi.org/10.22108/ijp.2022.133573.1277

Mokhtari M.A.A., Kouhestani H., Saeedi A. (2016) Investigation on type and origin of Copper mineralization at Aliabad Mousavi-Khanchy occurrence, East of Zanjan, using petrological, mineralogical and geochemical data. *Scientific Quarterly Journal of Geosciences* 25: 259–270. https://doi.org/10.22071/gsj.2016.40756

Mollai H., Dabiri R., Torshizian H.A., Pe-Piper G., Wang W.E. (2021) Upper Neoproterozoic garnet-bearing granites in the Zeber-Kuh region from east central Iran micro plate: Implications for the magmatic evolution in the northern margin of Gondwanaland. *Geologica Carpathica* 72 (6): 461-81. DOI: http://dx.doi.org/10.31577/GeolCarp.72.6.2

Müller D., Groves D.I. (1997) Potassic igneous rocks and associated gold-copper mineralization. *Springer-Verlag (Berlin)*, 238pp. https://doi.org/10.1007/978-3-319-23051-1

Müller D., Rock N., Groves D. (1992) Geochemical discrimination between shoshonitic and potassic volcanic rocks in different tectonic settings: a pilot study. *Journal of Mineralogy and Petrology* 46:259-289. https://doi.org/10.1007/BF01173568

Munker C., Pfander J. A., Weyer S., Buchl A., Kleine T., Mezger K. (2003) Evolution of planetary cores and the

Munker C., Worner G., Yogodzinski G., Churikova T. (2004) Behaviour of high field strength elements in subduction

Nabatian G., Ghaderi M. (2013) Oxygen isotope and fluid inclusion study of the Sorkhe-Dizaj iron oxide-apatite deposit, NW Iran. *Journal of International Geology Review* 55:397-410. https://doi.org/10.1080/00206814.2012.713547

Nabatian G., Ghaderi M., Daliran F., Rashidnejhad Omran, N. (2012) Sorkhe- Dizaj iron oxide- apatite ore deposit in the Cenozoic Alborz- Azarbaijan magmatic belt, NW Iran. *Resource Geology* 63: 42-56. https://doi:10.1111/j.1751-3928.2012.00209.x.

Nabatian G., Ghaderi M., Neubauer F., Honarmand M., Liu X., Dong Y., Jiang S.Y., von Quadt A., Bernroider M. (2014) Petrogenesis of Tarom high-potassic granitoids in the Alborz–Azarbaijan belt, Iran: Geochemical, U–Pb zircon and Sr–Nd–Pb isotopic constraints. *Journal of Lithos* 184:324-345. https://doi.org/10.1016/j.lithos.2013.11.002

Nabatian G., Jiang S.Y., Honarmand M., Neubauer F. (2016) Zircon U–Pb ages, geochemical and Sr-Nd-Pb-Hf isotopic constraints on petrogenesis of the Tarom-Olya pluton, Alborz magmatic belt, NW Iran. *Journal of Lithos*, 244: 43-58. https://doi:10.1016/j.lithos.2015.11.020.

Naderlou1 F., Mokhtari M. A A., Kouhestani H., Nabatian Gh. (2020) Type and origin of the north Chargar Cu-Au mineralization, southeast of Zanjan: using petrological, mineralogical and geochemical data. *Scientific Quarterly Journal of Geosciences* 31: 149-162. https://doi.org/10.22071/GSJ.2020.185408.1652

Nakamura H., Iwamori H., Nakagawa M., Shibata T., Kimura J.I., Miyazaki T., Chang Q., Vaglarov B.S., Takahashi T., Hirahara Y. (2019) Geochemical mapping of slab-derived fluid and source mantle along Japan arcs. *Journal of Gondwana Research* 70:36-49. https://doi.org/10.1016/j.gr.2019.01.007

Nazari M., Arian M.A., Solgi A., Zareisahamieh R., Yazdi A. (2023) Geochemistry and technomagmatic environment of Eocene volcanic rocks in the southeastern region of Abhar (NW Iran). *Iranian Journal of Earth Sciences*. https://doi.org/10.30495/ijes.2023.1956689.1746

Nazari M., Arian M.A., Solgi A., Zareisahamieh R., Yazdi A. (2023) Geochemistry and tectonomagmatic environment of Eocene volcanic rocks in the Southeastern region of Abhar, NW Iran. *Iranian Journal of Earth Sciences* 15(4): 228-247. DOI: https://doi.org/10.30495/ijes.2023.1956689.1746

Nebel O., Vroon P.Z., van Westrenen W., Iizuka T., Davies G.R. (2011) The effect of sediment recycling in subduction zones on the Hf isotope character of new arc crust, Banda arc, Indonesia. *Journal of Earth and Planetary Science Letters* 303:240-250. https://doi.org/10.1016/j.epsl.2010.12.053

Nielsen R.L., Forsythe L.M., Gallahan W.E., Fisk M.R. (1994) Major-and trace-element magnetite-melt equilibria. *Journal of Chemical Geology* 117:167-191. https://doi.org/10.1016/0009-2541(94)90127-9

Novais-Rodrigues E., Jalowitzki T., Gervasoni F., Sumino H., Bussweiler Y., Klemme S., Berndt J., Conceição R.V., Schilling M.E., Bertotto G.W. (2021) Partial melting and subduction-related metasomatism recorded by geochemical and isotope (He-Ne-Ar-Sr-Nd) compositions of spinel lherzolite xenoliths from Coyhaique, Chilean Patagonia. *Journal of Gondwana Research* 98:257-276. https://doi.org/10.1016/j.gr.2021.06.003

Otari, M and Dabiri, R. (2015) Geochemical and environmental assessment of heavy metals in soils and sediments of Forumad Chromite mine, NE of Iran. *Journal of Mining and Environment* 6(2): 251-261.

Ousta S.h., Ashja-Ardalan A., Yazdi A., Dabiri R., Arian M.A. (2024) Petrogenesis and tectonic implications of Miocene dikes in the southeast of Bam (SE Iran): Constraints on the development of active continental margin. *Geopersia* 14 (1): 89-111. DOI: https://doi.org/10.22059/geope.2023.364334.648729

Pan Z., Sun F., Cong Z. (2022) Petrogenesis, Sources, and Tectonic Settings of Triassic Volcanic Rocks in the Ela Mountain Area of the East Kunlun Orogen: Insights from Geochronology, Geochemistry and Hf Isotopic Compositions. *Journal of Minerals* 12(9): 1085. https://doi.org/10.3390/min12091085

Pang K.N., Chung S.L., Zarrinkoub M.H., Khatib M.M., Mohammadi S.S., Chiu H.Y., Chu C.H., Lee H.Y., Lo C.H. (2013) Eocene–Oligocene post-collisional magmatism in the Lut–Sistan region, eastern Iran: Magma genesis and tectonic implications. *Journal of Lithos* 180:234-251. https://doi.org/10.1016/j.lithos.2013.05.009

Pang K.N., Chung S.L., Zarrinkoub M.H., Mohammadi S.S., Yang H.M., Chu C.H., Lee H.Y., Lo C.H. (2012) Age, geochemical characteristics and petrogenesis of Late Cenozoic intraplate alkali basalts in the Lut–Sistan region, eastern Iran. *Journal of Chemical Geology* 306:40-53. https://doi.org/10.1016/j.chemgeo.2012.02.020

Patino Douce A.E. (1996) Effects of pressure and H2O content on the compositions of primary crustal melts. *Transactions of the Royal Society of Edinburgh: Earth Sciences* 87: 11-21. https://doi.org/10.1017/S026359330000643X

Pawley A.R., Holloway J.R. (1993) Water sources for subduction zone volcanism: New experimental constraints. *Journal of Science* 260:664-667. https://doi.org/10.1126/science.260.5108.664

Pearce J.A., Norry M.J. (1979) Petrogenetic implications of Ti, Zr, Y, and Nb variations in volcanic rocks. *Journal of Contributions to mineralogy and petrology* 69:33-47. https://doi.org/10.1007/bf00375192

Pearce J.A., Parkinson I.J. (1993) Trace element models for mantle melting: application to volcanic arc petrogenesis. *Journal of the Geological Society(London, Special Publications)* 76:373-403. https://doi.org/10.1144/GSL.SP.1993.076.01.19

Pearce JA (1983) Role of sub continental lithosphere in magma genesis at active continental margin In: C.J. Hawkesworth, and M. J. Norry, Eds, *Continental basalts and mantle xenoliths* (Shiva Publishing, Cheshire), pp.230- 249. https://orca.cardiff.ac.uk/id/eprint/8626

Peccerillo A., Taylor S. (1976) Geochemistry of Eocene calc-alkaline volcanic rocks from the Kastamonu area, northern Turkey. *Journal of Contributions to mineralogy and petrology* 58:63-81. https://doi.org/10.1007/BF00384745

Pieterek B., Tribuzio R., Matusiak-Małek M., Ciążela J., Horn I., Weyer S., Strauss H., Kuhn T., Muszyński A. (2024) Underplated melts control sulfide segregation at the continental crust-mantle transition. *Journal of Communications Earth & Environment* 5: 45. https://doi.org/10.1038/s43247-024-01218-9

Pitcher W.S., Atherton M.P., Cobbing E.J., Beckinsale R.D. (1985) Magmatism at a Plate Edge: The Peruvian Andes, *Glasgow (Blackie) and New York (Halsted Press)*, 328 pp. https://doi.org/10.1007/978-1-4899-5820-4

Poli G., Peccerillo A. (2016) The Upper Miocene magmatism of the Island of Elba (Central Italy): compositional characteristics, petrogenesis and implications for the origin of the Tuscany Magmatic Province. *Journal of Mineralogy and Petrology* 110:421-445. https://doi.org/10.1007/s00710-016-0426-6

Qian X., Wang Y., Feng Q., Zi J.W., Zhang Y., Chonglakmani C. (2016) Petrogenesis and tectonic implication of the Late Triassic post-collisional volcanic rocks in Chiang Khong, NW Thailand. *Journal of Lithos* 248:418-431. https://doi.org/10.1016/j.lithos.2016.01.024

Qian X., Wang Y., Srithai B., Feng Q., Zhang Y., Zi J.W., He H. (2017) Geochronological and geochemical constraints on the intermediate-acid volcanic rocks along the Chiang Khong–Lampang–Tak igneous zone in NW Thailand and their tectonic implications. *Journal of Gondwana Research* 45:87-99. https://doi.org/10.1016/j.gr.2016.12.011

Rahmani F., Mackizadeh M.A., Noghreyan M., Marchesi C., Garrido C.J. (2020) Petrology and geochemistry of mafic and ultramafic cumulate rocks from the eastern part of the Sabzevar ophiolite (NE Iran): Implications for their petrogenesis and tectonic setting. *Journal of Geoscience Frontiers* 11:2347-2364. https://doi.org/10.1016/j.gsf.2020.02.004

Roberts M.P., Clemens J.D. (1993) The origin of high potassium, calc-alkaline, I-type granitoids. *Journal of Geology* 21: 825-828. https://doi.org/10.1130/0091-7613(1993)021<0825:OOHPTA>2.3.CO;2

Sadr Jahan Mines Development Company (2013) The report of the end of the exploration operationin Rashtabad area.

Sadr Jahan Mines Development Company (2016-2017) Report of exploration activities and extraction plan in Rashtabad area.

Salehpour S., Arian M.A., Rad A.J., Zarei Sahamieh R., Yazdi A. (2025) Geochemistry and technomagmatic environment of Eocene volcanic rocks in Yuzbashi Chay region, west of Qazvin (Iran). *Iranian Journal of Earth Sciences* 17(1): 1-13. DOI: https://doi.org/10.57647/j.ijes.2025.1701.04

Santo A.P. (2021) A new magma type in the continental collision zone. The case of Capraia Island (Tuscany, Italy). *Journal of Geosciences* 11:104 pp. https://doi.org/10.3390/geosciences11020104

Sarkhoshi A., Aghazadeh M., Javanshir A. (2015) Petrogenesis of NW of Bam Volcanic Rocks. *Kharazmi Journal of Earth Sciences*

Sawyer E.W., Cesare B., Brown M. (2011) When the continental crust melts. *Journal of Elements* 7:229-234. https://doi.org/10.2113/gselements.7.4.229

Schandl E.S., Gorton M.P. (2002) Application of high field strength elements to discriminate tectonic settings in VMS environments. *Journal of Economic geology* 97:629-642. https://doi.org/10.2113/gsecongeo.97.3.629

Schildgen T.F., Yıldırım C., Cosentino D., Strecker M.R. (2014) Linking slab break-off, Hellenic trench retreat, and uplift of the Central and Eastern Anatolian plateaus. *Journal of Earth-Science Reviews* 128:147-168. https://doi.org/10.1016/j.earscirev.2013.11.006

Schroeder K.D. (2016) Diagram of the geological process of subduction. *subduction-en.svg from Wikimedia Commons*, CC-BY-SA 4.0 https://en.m.wikipedia.org/wiki/File:Subduction-en.svg##

Şengör A. M. C, Cin A., Rowley D.B., Nie S.Y. (1993) Space-time patterns of magmatism along the Tethysides: a preliminary study. *The Journal of Geology* 101:51-84. https://doi.org/10.1086/648196

Şengör A.M.C. (1984) The Cimmeride orogenic system and the tectonics of Eurasia. *Journal of Geological Society of America Special Paper* 195:82 pp. https://doi.org/10.1130/SPE195-p1

Sepidbar F., Mirnejad H., Changqian M., Shafaii Moghadam H. (2018) Identification of Eocene-Oligocene magmatic pulses associated with flare-up in east Iran: Timing and sources. *Journal of Gondwana Research* 57:141‑156. https://doi.org/10.1016/j.gr.2018.01.008

Seyyedi M., Lotfi M., Gourabjeripour A., Ashja Ardalan A. (2022) Investigation of alterations and lineaments in Rashid Abad mineral area (N Zanjan, NW Iran), Using integration of Remote Sensing and Aeromagnetic data. *Iranian Journal of Earth Sciences* 14:301-321. https://doi.org/10.30495/ijes. 2022.1942724.1660

Shafaii Moghadam H., Li X.H., Ling X.X., Santos J.F., Stern R.J., Li Q.L., Ghorbani G. (2015b) Eocene Kashmar granitoids

Shafaii Moghadam H., Rossetti F., Lucci F., Chiaradia M., Gerdes A., Martinez M.L., Ghorbani G., Nasrabady M. (2016) The calc-alkaline and adakitic volcanism of the Sabzevar structural zone (NE Iran): Implications for the Eocene magmatic flare-up in Central Iran. *Journal of Lithos* 248-251: 248-535. https://doi.org/10.1016/j.lithos.2016.01.019

Shahbazi S., Ghaderi M., Afzal P. (2019) Prognosis of of gold mineralization phases by multifractal modeling in the Zehabad epithermal deposit, NW Iran. ***I**ranian **J**ournal of **E**arth **S**ciences* 13(1): 31-40. https://doi.org/10.30495/IJES.2021.678957

Shamloo H.I., Grunder A.L. (2023) Magma mingling and ascent in the minutes to hours before an explosive eruption as recorded by banded pumice. *Journal of Geology* 51:957-961. https://doi.org/10.1130/G51318.1

Shokri P., Dehbozorgi M., Hakimi Asiabar S. (2020) Recent tectonic activity in Central Alborz Mountain, Iran: morphometric analysis and knickpoint identification. *Journal of Mountain Science* 17:3137-3161. https://doi.org/10.1007/s11629-019-5945-2

Smith I.E.M., Stewart R.B., Price R.C. (2003) The petrology of a large intra-oceanic silicic eruption: The Sandy Bay Tephra, Kermadec Arc, Southwest Pacific. *Journal of Volcanology and Geothermal Research* 124: 173–194. https://doi.org/10.1016/S0377-0273(03)00040-4

Stöcklin J. (1968) Structural history and tectonics of Iran: a review. *Journal of American Association of Petroleum Geologists (AAPG) bulletin* 52:1229-1258. https://doi.org/10.1306/5D25C4A5-16C1-11D7-8645000102C1865D

Stöcklin J., Eftekhar Nezhad J. (1969) Geological map of Zanjan, scale 1:250 000, 1 sheet, No. D4-61: *Geological Survey of Iran*, Tehran. https://library.iut.ac.ir/dL/search/default.aspx?Term=9891&Field=0&DTC=100

Stöcklin J., Nabavi M.H. (1973) Tectonic map of Iran, scale 1:2 500 000, 1 sheet, *Geological Survey of Iran*, Tehran https://www.davidrumsey.com/luna/servlet/detail/RUMSEY~8~1~354487~90121471

Su H.M., Jiang S.Y., Zhang D.Y., Wu X.K. (2017) Partial melting of subducted sediments produced early Mesozoic calc-alkaline lamprophyres from northern Guangxi Province, South China. *Journal of Scientific Reports* 7:4864. https://doi.org/10.1038/s41598-017-05228-w

Sun S.S., McDonough W.F. (1989) Chemical and isotopic systematics of oceanic basalts: implications for mantle composition and processes, *Journal of the Geological Society (London, Special Publications)* 42:313-345. https://doi.org/10.1144/GSL.SP.1989.042.01.19

Tarabi S., Emami M.H., Modabberi S., Sheikh-Zakariaee S.J. (2019) Eocene-Oligocene volcanic units of momen abad, east of Iran: petrogenesis and magmatic evolution. *Iranian Journal of Earth Sciences* 11:126-140. https://doi.org/10.30495/IJES.2019.665319

Tatsumi Y. (2000) Slab melting: its role in continental crust formation and mantle evolution. *Journal of Geophysical Research Letters* 27:3941-3944. https://doi.org/10.1029/2000GL012061

Tatsumi Y., Takahashi T. (2006) Operation of subduction factory and production of andesite, *Journal of Mineralogical and Petrological Sciences* 101:145-153. https://doi.org/10.2465/jmps.101.145

Taylor S.R. Mclennan S.M. (1985) The continental crust: Its composition and evolution. *The Journal of Geology* 94: 57–72.

Temel A., Gündoğdu M.N., Gourgaud A. (1998) Petrological and geochemical characteristics of Cenozoic high-K calc-alkaline volcanism in Konya, Central Anatolia, Turkey. *Journal of volcanology and geothermal research* 85:327-354. https://doi.org/10.1016/S0377-0273(98)00062-6

Till C. B., Kent A. J. R., Abers G. A., Janiszewski H. A., Gaherty J. B., Pitcher B. W. (2021) The causes of spatiotemporal variations in erupted fluxes and compositions along a volcanic arc. *Journal of Nature Communications* https://doi.org/10.1038/s41467-019-09113-0.

Towsehe Olume Zamin Company (TOZ Co.) (2003) Systematic geochemical explorations in leaf of Hashtjin (1:100,000). *Report of Ardabil province SAMT organization.*

Ulmer P. (2001) Partial melting in the mantle wedge-the role of H_2O in the genesis of mantle-derived 'arc-related'magmas. *Journal of Physics of the Earth and Planetary Interiors* 127:215-232. https://doi.org/10.1016/S0031-9201(01)00229-1

Wang X.C., Li Q., Wilde S.A., Li Z.X., Li C., Lei K., Li S.J., Li L., Pandit M.K. (2021) Decoupling between oxygen and radiogenic isotopes: evidence for generation of juvenile continental crust by partial melting of subducted oceanic crust. *Journal of Earth Science* 32:1212-1225. https://doi.org/10.1007/s12583-020-1095-2

Weaver B.L., Tarney J. (1984) Empirical approach to estimating the composition of the continental crust. *Journal of Nature* 310: 575-577. https://doi.org/10.1038/310575a0

Wilson M. (1989) Igneous petrogenesis A global tectonic approach: *Unwin Hyman*, London, 466 pp. https://doi.org/10.1007/978-1-4020-6788-4

Winter J.D. (2001) An introduction to igneous and metamorphic petrology. United States of America.

Winter J.D. (2010) Principles of igneous and metamorphic petrology, *Second Ed, Prentice Hall,* New York, 720 pp.

Woudloper (2009) Tectonic map of southern Europe, North Africa and the Middle East, *wikimedia,* Own work, 1 sheet. https://en.m.wikipedia.org/wiki/File:Tectonic_map_Mediterranean_EN.svg

Wu J.T-J., Wu J., Alexandrov I., Lapen T., Lee H.Y, Ivin V. (2022) Continental growth during migrating arc magmatism and terrane accretion at Sikhote-Alin (Russian Far East) and adjacent northeast Asia. *Journal of Lithos* 432:106891. https://doi.org/10.1016/j.lithos.2022.106891

Yang W.B, Niu H.C., Shan Q., Chen H.Y., Hollings P., Li N.B., Yan S., Zartman R.E. (2014) Geochemistry of primary-carbonate bearing K-rich igneous rocks in the Awulale Mountains, western Tianshan: Implications for carbon-recycling in subduction zone. *Journal of Geochimica et Cosmochimica Acta* 143:143-164. https://doi.org/https://doi.org/10.1016/j.gca.2014.04.033

Yang W.B., Niu H.C., Cheng L.R., Shan Q., Li N.B. (2015) Geochronology, geochemistry and geodynamic implications of the Late Mesozoic volcanic rocks in the southern Great Xing'an Mountains, NE China. *Journal of Asian Earth Sciences* 113:454-470. https://doi.org/10.1016/j.jseaes.2014.12.002

Yazdani S., Castillo P.R., Hassanzadeh J. (2018) Crust-mantle interaction inferred from the petrology and Sr-Nd-Pb isotope geochemistry of Eocene arc lavas from the Kahrizak Mountains, north-central Iran *Journal of Lithos* 318:299-313. https://doi.org/10.1016/j.lithos.2018.08.018

Yazdi A., Ashja-Ardalan A., Emami M.H., Dabiri R., Foudazi M. (2019) Magmatic interactions as recorded in plagioclase phenocrysts of quaternary volcanics in SE Bam (SE Iran). *Iranian Journal of Earth Sciences* 11(3): 215-224. DOI: https://doi.org/10.30495/ijes.2019.667379

Yazdi A., ShahHoseini E., Razavi R. (2016) AMS, A method for determining magma flow in Dykes (Case study: Andesite Dyke). *Research Journal of Applied Sciences* 11(3): 62-67. DOI: http://doi.org/10.3923/rjasci.2016.62.67

Yazdi A., Shahhosseini E., Moharami F. (2022) Petrology and tectono-magmatic environment of the volcanic rocks of West Torud–Iran, *Iranian Journal of Earth Sciences* 14(1): 40-57. https://dx.doi.org/10.30495/ijes.2022.1929200.1601

Zamanian H., Rahmani S.h., Zareisahamieh R., Pazoki A., Yang X.Y. (2020) Geochemical characteristics of igneous host rocks of Lubin-Zardeh Au-Cu deposit, NW Iran. *Ore Geology Reviews* 122: 103496. https://doi.org/10.1016/j.oregeorev.2020.

Zanchi , Berra , Mattei , Ghassemi M.R., Sabouri J. (2006) Inversion tectonics in central Alborz, Iran. *Journal of Structural Geology* 28:2023-2037. https://doi.org/10.1016/j.jsg.2006.06.020

Zhang , Liang , Wang , Jin Z., Zhu L., Gan W. (2020) Experimental constraints on the partial melting of sediment-metasomatized lithospheric mantle in subduction zones. *Journal of American Mineralogist* 105:1191-1203. https://doi.org/10.2138/am-2020-7403

Zheng W. F. (2019) Subduction zone chemistry. *Journal of Geoscience Frontiers* 10: 1223–1254. https://doi.org/10.1016/j.gsf.2019.02.003

Zheng Y., Chen R., Xu Z., Zhang S. (2016) The transport of water in subduction zones. *Journal of Science China Earth Sciences* 59:651-682. https://doi.org/10.1007/s11430-015-5258-4

Zhong H., Zhu W.G., Hu R.Z., Xie L.W., He D.F., Liu F., Chu Z.Y. (2009) Zircon U–Pb age and Sr–Nd–Hf isotope geochemistry of the Panzhihua A-type syenitic intrusion in the Emeishan large igneous province, southwest China and implications for growth of juvenile crust. *Journal of Lithos* 110:109-128. https://doi.org/10.1016/j.lithos.2008.12.006

zones: Constraints from Kamchatka–Aleutian arc lavas. *Journal of Earth and Planetary Science Letters* 224: 275–293. https://doi.org/10.1016/j.epsl.2004.05.030